University of Alberta

Modeling the mechanics of soft particles using nonlinear membrane theory

by

Touqeer Sohail

A thesis submitted to the Faculty of Graduate Studies and Research in partial fulfillment of the requirements for the degree of

Doctor of Philosophy

Department of Mechanical Engineering

Abstract

Recently research on small soft particles shows impeccable interests because of their significance in both biology and industry. The term 'particle' here is defined as a deformable object with size in the range of nano- to micrometers. Many experimental efforts have been spent on investigating the behavior of these particles and theoretical models have been proposed to describe the mechanics of these particles under different loading conditions. Due to the complex nature of these particles, these mechanics models are all accompanied by various assumptions, one of the common simplifications being the neglect of large deformation. The objective of this study is to explore the application of the nonlinear membrane model in describing the mechanical behaviors of soft particles under several loading conditions relevant to practice. In all cases studied, an originally spherical particle filled with fluid inside was considered. The surface of the particle was considered to be hyperelastic and able to sustain large deformation. The enclosed fluid was modeled to be incompressible. The particle was subjected to four different loading conditions: (i) symmetric poking by two identical conical indenters; (ii) asymmetric poking by a conical indenter and a flat indenter; (iii) micropipette aspiration; and (iv) electrostatic attraction to a charged substrate. The theoretical results were compared with experimental results involving the mechanical response of soft particles such as cells. The model developed in this dissertation is capable of characterizing certain phenomena observed in experiments. The proposed model investigates the large deformation in soft particles from a continuum perspective. The model will be useful in understanding the mechanical properties of particles such as cells, vesicle and microcapsules that have an immense importance in life and industrial applications.

Acknowledgements

Studying at the University of Alberta has been an incredible experience for me. I would like to thank all those who helped me along the way, gave me the strength to complete my PhD degree and made the past four years of my life truly memorable.

I would like to start with Dr. Farbood Fahimi. My academic journey at this university began in 2009 when he invited me to conduct research under his supervision. Although Dr. Fahimi left Canada a few short months later, at which point I had to redirect my research interests, I am grateful to him for having started me on the academic path.

I would like to express my immense gratitude to my wonderful supervisors, Dr. Tian Tang and Dr. Ben Nadler. Without their encouragement and support, this dissertation would not have been possible. Dr. Tang has always challenged me with thought-provoking ideas that helped me better understand the problems I was trying to solve and eventually enabled me to find superior solutions. I truly believe I am a better academic for it and I thank her from the bottom of my heart. As for Dr. Nadler, he has been a great mentor to me: not only did he teach me a lot about Continuum Mechanics and the Finite Element Method, but also about life in general. Although he moved to the University of Victoria two years ago, Dr. Nadler continued to supervise my research progress by sharing his expertise with me when I needed it the most. For that, I am truly grateful and thank him very much.

I would also like to thank Dr. Tian Tang, Dr. Xiaodong Wang, Dr. Jason Olfert, Dr. John Beamish and Dr. Donald Raboud for allowing me the

Contents

List of Figures

List of Abbreviations

Symbol	Description
AFM	Atomic force microscope
SFM	Scanning force microscope
IF	Intermediate filament
DLS	Dynamic light scattering
DWS	Diffusing wave spectroscopy
FCS	Fluorescence correlation spectroscopy
ODEs	Ordinary differential equations
BVP	Boundary value problem
BCs	Boundary conditions
DI	Deionized
PBs	Phosphate-buffered saline solution
ZP	Zona Pellucida
JKR	Johnson-Kendall-Roberts
DMT	Derjaguin-Muller-Toporov
P-B	Poisson-Boltzmann
D-H	Debye-Huckel
FEM	Finite element Method

List of Symbols

All dimensional parameters and symbols used in this work are listed below. When a bar is added to a parameter, it represents the dimensionless value associated with that parameter. Specific normalization of parameters is explained in detail in each chapter.

Chapter 2: List of Symbols

Symbol	Description
P_0, P_1	Material points
IR^3	Euler space
κ	Reference configuration
φ	Deformed configuration
$\{X_1, X_2, X_3\}$	Referential Euler coordinates
$\{x_1, x_2, x_3\}$	Deformed Euler coordinates
$\{E_1, E_2, E_3\}$	Referential Orthonormal basis
$\{e_1, e_2, e_3\}$	Deformed orthonormal basis
χ	Mapping function
$\otimes$	Tensor product operator
$\mathbf{I}$	Identity tensor
∇	Spacial gradient operator
Div	Divergence operator
$\mathbf{P}$	Piola-kirchoff stress tensor
J	Areal dilation
$\mathbf{f}$	Body force/lateral traction
w	Strain energy density function
$\mathbf{C}$	Cauchy-Green deformation tensor
$\boldsymbol{\sigma}_f$	Cauchy stress tensor
$\mathbf{f}_f$	Fluid traction
p_f	Fluid pressure
G	Material constant

V_0	Inflated membrane volume before deformation
V	Membrane volume after deformation
$\mathbf{F}$	Deformation gradient
$\{i, j, k\}$	Cylindrical coordinates
$\{R, \theta, \phi\}$	Spherical coordinates
$\{\mathbf{E}_R, \mathbf{E}_\phi, \mathbf{E}\theta\}$	Spherical orthonormal basis
R	Referential spherical membrane radius
r	Inflated membrane radius
$\{\mathbf{g}_\phi, \mathbf{g}_\theta\}$	Covariant basis
$\{\mathbf{G}^\phi, \mathbf{G}^\theta\}$	Contravariant basis
λ, μ	Prinicipal stretches
$T\kappa$	Tangent plane in κ
$T\varphi$	Tangent plane in φ
$\{\mathbf{L}, \mathbf{M}, \mathbf{N}\}$	Orthonormal basis in κ
$\{\mathbf{l}, \mathbf{m}, \mathbf{n}\}$	Orthonormal basis in φ
ψ	Meridian angle in φ

Chapter 3: List of Symbols

Symbol	Description
κ	Reference configuration
φ	Deformed configuration
$\{i, j, k\}$	Cylindrical coordinates
$\{R, \theta, \phi\}$	Spherical coordinates
R	Referential spherical membrane radius
r	Inflated membrane radius
ψ	Meridian angle in φ
$\mathbf{l}$	Tangent unit vector on the membrane surface
p_c	Contact pressure between the membrane and the indenter
P_i	Initial magnitude of Piola-kirchoff stress in the inflated membrane
p_f	Fluid pressure
F	Vertical Indenter force
α	Conical Indenter sharpness
τ	Tangent angle on the membrane surface

$\phi = 0$	Upper pole of the membrane
$\phi = \pi/2$	Circumference of the membrane
h	Indenter height
d	Indenter displacement
u_c	Contact radius of membrane with indenter
P_0	Piola-kirchoff stress at the pole
w_λ, w_μ	Prinicipal stresses
λ, μ	Prinicipal stretches

Chapter 4: List of Symbols

Symbol	Description
κ	Reference configuration
φ	Deformed configuration
$\{i, j, k\}$	Cylindrical coordinates
$\{R, \theta, \phi\}$	Spherical coordinates
R	Referential spherical membrane radius
r	Inflated membrane radius
ψ	Meridian angle in φ
$\mathbf{l}$	Tangent unit vector on the membrane surface
h	Indenter height
d	Indenter displacement
P_0	Principal stress at the pole
τ	Tangent angle on the membrane surface
$\phi = 0$	Upper pole of the membrane
$\phi = \pi$	Lower pole of the membrane
p_{c_1}	Conical indenter pressure on membrane
f_c	Conical Indenter force
p_{c_2}	Flat support pressure on membrane
f_s	Flat support force
Ω_{c_1}	Membrane contact part with indenter
Ω_{c_2}	Membrane contact part with flat support
u_{c_1}	Contact radius of membrane with conical indenter
u_{c_2}	Contact radius of membrane with flat support
P_0	Principal stress at pole

p_f	Fluid pressure
F	Vertical Indenter force
u_0	maximum horizontal distance from the axisymmetric axis
O'	Indenter tip position
P_i	Initial magnitude of Piola-kirchoff stress in the inflated membrane
w_λ, w_μ	Prinicipal stresses
λ, μ	Prinicipal stretches

Chapter 5: List of Symbols

Symbol	Description
κ	Reference configuration
φ	Deformed configuration
$\{i, j, k\}$	Cylindrical coordinates
$\{R, \theta, \phi\}$	Spherical coordinates
R	Referential spherical membrane radius
r	Inflated membrane radius
ψ	Meridian angle in φ
τ	Tangent angle on the membrane surface
L	Aspiration length
$\psi(\phi c_1)$	Angle from axisymmetric axis to the pipette wall
$\psi(\phi c_2)$	Angle from axisymmetric axis to the pipette edge
P_1	Internal pressure inside the pipette
P_2	External pressure outside the pipette
p_f	Fluid pressure
f_v	Fluid traction on the membrane
f_p	Vertical pipette force on the membrane
f_h	Horizontal pipette force on the membrane
P_i	Initial magnitude of Piola-kirchoff stress in the inflated membrane
w_λ, w_μ	Prinicipal stresses
λ, μ	Prinicipal stretches

Chapter 6: List of Symbols

Symbol	Description
$\{i, j, k\}$	Cylindrical coordinates
$\{R, \theta, \phi\}$	Spherical coordinates
R	Spherical membrane radius
r	Inflated membrane radius
τ	Tangent angle on the membrane surface
$\mathbf{t}$	Tangent direction on the membrane
$\mathbf{n}$	Normal direction on the membrane
σ	Surface charge density on the membrane
$\hat{\sigma}$	Surface charge density of the substrate
Q	Charge
Φ	Electric potential
k	Debye length
∇	Spacial gradient operator
ϵ_0	Free space permittivity
ϵ	Dielectric constant
k_B	Boltzmann constant
T	Absolute temperature
z_i	Valence of the ith type of ions
$n_{i\infty}$	Bulk number concentration of the ith type of ions
$\mathbf{f}_e$	Total electrostatic on an arbitrary element da_1
$\mathbf{f}_{et}$	Electrostatic traction in the tangential direction
$\mathbf{f}_{en}$	Electrostatic traction in the normal direction
$\mathbf{f}_f$	Fluid traction on the membrane
a	Membrane contact radius with substrate
H	Vertical distance between the membrane and the substrate
Z	Membrane height
ψ	Meridian angle in φ
w_λ, w_μ	Prinicipal stresses
λ, μ	Prinicipal stretches

Chapter 1

Introduction

1.1 Motivation

The motivation for this thesis emanated from the significance of mechanics of small soft particles ($\mu m \sim nm$) in both medical and industrial applications. These particles have been widely used in food, pharmaceutical, chromatography, electrophotography, bio-technology, and bio-medical industries [1, 2]. In the food industry, the soft tissues of fruits and vegetables are subjected to external mechanical loading during harvesting, plucking, transport and storage [3]. Such mechanical stresses affect the physiological processes inside the cell [4] and can cause damage to the cell. The quality of these products is determined by the strength of the soft tissues [5]. Therefore, it is very important for the food industry to understand the rheological and micromechanical behavior of these soft tissues [3, 5, 6]. In the pharmaceutical industry, soft particles (e.g., microcapsules which are liquid-filled particles with a thin membrane) are used for drug delivery and construction of synthetic cells for artificial organs and artificial blood [7]. The delivery of these targeted drugs to specific sites in the body at a precisely controlled rate is critically important in the medicine field [8]. Since soft and flexible materials are used to carry

out the drug delivery process, it is important to determine the mechanical properties of the synthetic capsules in order to determine the kinetics of the encapsulated chemicals and to control the durability of these capsules during usage [7]. To control micro-fluidic channels, stimuli-responsive gels are used as actuators that undergo volume change in response to surrounding environment [9]. Such change is not possible with conventional micro-actuators that require external power to operate. In microcirculation, blood cells undergo repeated deformation through small vessels for the transport of blood to different tissues [10]. The deformation of these cells in response to physical forces is important to their in-vivo rheological behavior during circulation in the capillaries [10, 11]. In electrophotography, under external electric field, small charged particles are transferred from one surface to another for photocopying and printing [12–14]. A similar process has been used in electrostatic powder coating [15]. Adhesion of these particles to substrate is of utmost importance to these applications. For example, in electrophotography, the adhesion of the charged particle to the paper is important to the quality of the image. In powder coating, strong adhesion is necessary to make the deposited powders stay on the workpiece before they are completely cured [16]. The study of mechanics of soft particles is also critically important in other applications such as filtration of deformable particles, centrifugal separation of microorganisms, and wet pressing of paper [2]. The deformation of soft particles greatly influences the manufacturing, separation and purification of products containing such material [1].

The remainder of this chapter is organized in three sections. The first section offers a review of the experimental techniques used to determine the mechanical properties of soft particles. The second section presents different theoretical approaches to modeling the mechanical properties of soft particles under various loading conditions. The last section reveals the original

2

contribution that the present thesis makes and provides the thesis outline.

1.2 Experimental techniques to probe mechanical properties of soft particles

In the literature, there are numerous reports of experimental techniques that have been applied to probe the mechanical properties of the flexible particles at different length scales. These particles, which are used in various applications, differ from one another in both structure and internal functional behavior. For example, some plant cells have a hard cell wall, which acts as a shell that dominates their mechanics, while other cells have a soft membrane and their mechanical response is determined by the internal protein network and cytoskeleton [17]. Different cells (e.g., leukocyte, granulocyte, endothelial, Chondrocyte and human neutrophils) respond differently to external loading [10, 11, 18–21]. For instance, Chondrocyte cells obtained from non-osteoarthritic (normal) and osteoarthritic conditions show significant difference in cell volume in response to applied mechanical deformation [18]. To determine the mechanical properties of these particles, an external force is applied to the particle, and the particle's response is monitored. The force typically ranges from pN to nN and can be applied by optical traps, magnetic beads, glass needles, and atomic force microscope cantilevers. The deformation of the particle on a scale of nanometers to microns can be measured by deflection of lasers onto optical detectors or by high resolution microscopy [17]. Experiments generally use compression, indentation, aspiration, shear, magnetic or electrostatic forces to deform the particle.

The compression technique is a method in which a particle is compressed between two flat plates and its physical properties are determined. Usually, in this technique one plate is fixed and other is movable to produce

stress on the particle in order to determine the elasticity, visco-elasticity and stresses/stretches on the particles. The compression technique is used in many applications. For example, in the pharmaceutical industry, the compression technique is used to study the fragmentation of particle (tablet) and to study the effect of additives (e.g. binders) on the particle strength [22]. It was observed that the surface area of the tablet increases with compaction pressure [22]. Lin *et al.* [1] compared the geometrical variation of compressible and incompressible soft particles and determined the difference in the behavior of these particles under uni-axial compression. It was observed that the lateral extension for incompressible particles was greater than that for compressible particles, and rapid reduction in porosity was observed for incompressible soft particles. In biomechanics, the compression technique is used to apply uniaxial force to deform cells and measure their mechanical properties. For example, endothelial cells were subjected to compression between glass microplates and the resulting deformation was obtained [23]. It was observed that the elastic modulus of the nuclei in round and spread cell is $5000N/m^2$ which is 10 times larger than that of the cytoplasm [23].

Poking or indentation is a technique in which a very small force is applied locally to the surface of the particle with the help of a poker or indenter to determine the local mechanical properties of the particle. The force applied is in the nN range and the displacement measured is in the nm range [24]. By varying the rate of the applied force, the force vs. displacement curve gives significant information about the elasticity and visco-elasticity of the particle. The observed response may be linear or nonlinear, depending upon the material properties of the particle and the extent of the deformation. During poking, the stiffness of the particle increases as the magnitude of indentation increases. The poker tip diameter is very small compared to the diameter of the particle, which makes it possible for local viscosity to be measured at

different regions of the particle [17]. With considerable advances in the indentation methods, this technique has been extensively used to investigate the mechanical properties of cells. Glass needles, both uncoated and coated with laminin, were used to deform rat embryo fibroblast [25]. Coated glass needles with laminin were used to induce attachment to the cell surface . For both cases, the experimentally applied force produced local response by the cytoskeleton. When the uncoated glass needle was used to probe the cell, it was observed that the cell's behavior could be predicted by the three layer model proposed by Dong *et al.* [26] in which the nucleus was highly elastic, the cytoplasm was a viscoelastic fluid and the outer cortical layer was an elastic shell with prestressed tension. The stiffness of the cortical layer increased when the adhesive laminin coated needle was used to recruit the actin filaments to the contacted surface region [25]. Visualization of the actin recruitment confirmed a widely postulated model for the mechanical connections between the extracellular matrix proteins and the actin cytosleketon [25]. Similarly, vertical glass stylus with tip of $2\mu m$ in diameter was used to poke osmotically swollen human erythrocytes to determine its elastic area compressibility modulus [27]. The analysis of data gave a range of values (17.9 ± 8.2 to 34.8 ± 12 $mdyn/\mu m$) for the elastic area compressibility modulus at 25^oC depending on the osmotic conditions [27]. The $2\mu m$ small probe was also used to poke the fibroblast and it was observed that both the cytoplasm and nucleus resist the deformation [28]. It was shown that the resistance to deformation has both viscous and elastic components, and an increase in the depth of indentation leads to an increase in stiffness. During indentation, the probe tip causes changes in the microscopic appearance of the cell, which persisted for a long time period (sustained stresses) [28]. Specifically, when a pressure of $0.1atm$ was applied for some time, a circular dark spot was seen on the cell with similar dimensions to that of the probe, but it eventually disappeared [28].

5

The visible time of this spot depended on the magnitude and duration of the applied pressure [28]. This spot might result from the rearrangement of cytoplasmic components in response to a sustained pressure [28]. The hysteresis in the measurements could be due to cytoplasmic viscosity and the sustained stresses. The recovery from the sustained stresses is faster at 37^oC than at 25^oC. Compared to erythrocyte, the fibroblast provided greater resistance to deformation and, due to its network of microfilament, microtubules and intermediate filaments, it was capable of sustaining more force than the cortical matrix of the erythrocyte [28].

Micropipette is a technique in which a control negative pressure is applied to aspirate particles into the pipette to measure their deformation, rheology, viscosity and elastic properties. This technique has been used to measure mechanical properties of cells/vesicles such as bending stiffness, viscosity, relaxation during recovery after being aspirated into a micropipette [10, 11, 18] and adhesion during detachment from a substrate [29, 30]. To understand the flow of cells in vessels, arteries, veins and capillaries, where deformation occurs, the micropipette technique has been applied to different living cells such as granulocyte, leukocyte, erythrocyte, endothelial, red blood cell, chondrocyte, and human neutrophil. Schmid-Schonbein *et al.* [19] observed that, when the human leukocyte was aspirated by the micropipette at different locations using the same pipette and control pressure, similar deformation occurred, suggesting homogenous properties on the scale of the micropipette. Dong *et al.* [31] observed small instantaneous deformation of leukocytes when the cell sealed the micropipette tip, which was modeled as the initial elastic response of the cell. Similarly, this initial elastic response for leukocytes was observed by Sung *et al.* [11] during its recovery from the micropipette. The leukocyte was found to return to a spherical shape during its recovery from the deformation in the micropipette [11, 19] and it was suggested that this behavior

6

was due to the pre-stressed tension in the cortical layer [31]. Micropipette aspiration of endothelial cells has shown greater stiffness and viscosity as compared to erythrocytes [21]. White blood cells were more resistive than red blood cells and therefore larger suction pressure was required to deform white blood cells [11, 32]. Through micropipette experiments for normal chondrocytes and osteoarthritic chondrocytes, Jones *et al.* [18] observed that their Young's moduli were almost identical, but there was significant volumetric difference between normal chondrocytes and osteoarthritic chondrocytes after deformation. Evan *et al.* [33] carried experiments using micropipette to study the entry flow of single blood granulocytes. The results showed that the outer cortex of the cell maintained a persistent tension of 0.035 dyn/cm during aspiration in the micropipette. This tension created a threshold pressure below which the cell could not enter the pipette. Different pipette sizes have been used to determine the apparent viscosity of the cell which strongly depends upon the temperature. The apparent viscosity determined was 2×10^3 poise at 23^oC, smaller than 1×10^3 poise at 37^oC and larger than 10^4 poise below 10^oC [33].

When comparing the micropipette and poking techniques, the micropipette is a preferred technique in which small forces are easily applied to detect changes in deformation during aspiration [27]. Also, the control on the applied force and visualization of the deformed surface are easier with micropipette aspiration than with poking [27]. However, poking is better suited to study the adhesion and spreading of particles [27]. For example, when the aspiration pressure is zero, the leukocyte may not come out of the pipette due to its adhesion to the pipette wall; therefore, positive pressure may be needed to remove the leukocyte from the pipette [19]. The adhesion between the poker tip and the cell is less problematic than adhesion between the cell and the micropipette wall [19, 27]. Cell poking avoids the detachment of plasmalemma

from the underlying cytoskeleton which might result from micropipette aspiration [27, 28]. The contribution of intracellular organelles to the mechanical properties of the whole cell may be more readily detected using poking [27]. Mechanical properties of erythrocytes determined from poking experiments were compared with the ones determined from micropipette aspiration. The results were in reasonable agreement [34] which suggested that the structural elements in erythrocyte that resist area expansion respond similarly to both pulling and pushing forces [27]. The elastic area compressibility modulus of the erythrocyte membrane determined by Daily *et al.* [27] using cell poking was 17.9 ± 8.2 to $34.8 \pm 12.0 \ mdyn/\mu m$. Similarly, the elastic area modulus of the erythrocyte membrane determined by Evans *et al.* [34] using the micropipette technique was $28.8 \pm 5.0 \ mdyn/\mu m$. Both performed the experiment at 25°C and at the same osmotic conditions. Mitchison *et al.* [35] suggested that in the micropipette experiment the hysteresis in the pressure vs. deformation curves during loading and unloading was mainly due to the friction between the cell surface and the pipette edge. However, Petersen *et al.* [28] argued that the hysteresis was due to viscoelastic nature of the cell, since hysteresis was also found in indentation experiments, which could not be attributed to friction alone, due to the lack of extensive contact between the cell and the indenter [35].

AFM and scanning force microscope (SFM) are surface image techniques that work by scanning the sample surface using a sharp tip and continuously recording the images [17, 36–39]. The force between the AFM tip and the particle is obtained by measuring the deflection of the flexible cantilever through laser beam. The images can be created using different modes (e.g., contact mode, tapping mode and jumping mode) to measure the surface topography [17, 36–39], but in the tapping mode, the occurrence of sample damage is minimized [36, 37]. AFM technique is related to the poking technique, but it

has higher force resolution and can be used to apply precisely controlled load at different locations of the sample [17]. The limitation of this technique is that it cannot measure the properties inside the particle, but only of the accessible surface [17]. When the AFM tip is attached to the particle, it can be used for both pulling and pushing [17]. Putman *et al.* [39] used AFM to measure the response of the surface of monkey kidney cells and observed that the cell became stiffened when probed under a tapping motion at high frequency. Recently, advancement in the AFM technique has been made by attaching a polystyrene bead at the AFM tip [40, 41]. Such well-defined probe geometry deforms the sample nondestructively and helps to capture the mechanical response of the object more accurately, because the stress in the sample depends on the shape of the tip [40,41]. The bead diameter can be in the range of $12\mu m$ to less than $1\mu m$, which corresponds to the contact area of $0.5 - 30\mu m^2$ and stress range of $100Pa - 10kPa$ [41]. Such low stress allows for the probing of soft material. For example, AFM with polystyrene bead at the tip has been used to determine the viscoelastic properties of thin fibroblast and polymer gels [40,41].

The fluid flow system is a technique in which a particle is exposed to controlled fluid stresses to determine its response. This technique has practical significance both in biology and industrial applications. Cells can experience shear stresses, as in the case of red blood cells during flow in the circulating system. Red blood cells adhering to a surface in a parallel plate flow channel were found to be stretched when exposed to a fluid shear stress [42]. The elastic modulus of the red blood cell determined this way is $10^4 dyn/cm^2$ with a membrane thickness of $0.01\mu m$ [42]. The distribution of mechanical strain in the intermediate filament (IF) of cytoskeleton of endothelial cells was measured in response to shear flow [43, 44]. It was observed that IF displacement in cells caused by fluid-shear stresses rapidly changed the cytoskeletal mechanics

[43, 44]. The IF displacement was more significant above the nucleus when compared with near the coverslip surface, and the displacement downstream from the nucleus was larger than the upstream areas [43]. It was also found that the shear stress induced an increase in IF strain that was highly localized within the cell [44]. The viscoelastic behavior of endothelial surface layer in response to fluid shear stress was presented in [45]. It was found that the core proteins in the structure acted as transducers, which allowed the fluid shear stress to deform the cortical cytoskeleton [45]. Similar to endothelial and blood cells, bone cells also undergo structural changes when exposed to shear stresses. In a parallel plate flow chamber, a shear stress was applied to a monolayer of cultured bone cells [46]. It was observed that the bone tissue changed its structure due to a local distribution of strains resulting from the fluid shear stresses [46]. The suspension of colloidal particles in the fluid can be found in various applications such as pharmaceuticals, paints, inks, brakes and food [47]. The micro-structural arrangement of these particles is important to the macroscopic properties of the system. For instance, when particles suspended in electrorheological fluids were subjected to both electric field and shear flow, stable lamellar patterns were achieved due to difference in the dipole moment induced in the particles [47]. By controlling the external field and shear flow, the desired macroscopic properties of colloidal system can be achieved [47].

In dynamic light scattering (DLS) and diffusing wave spectroscopy (DWS), a laser beam is sent through a sample of milliliter volume and scattered light is collected with a detector [17,48]. This technique allows for the determination of viscoelastic behavior of complex fluid that carries suspended colloidal particles [49]. This technique is also helpful in understanding polymer solutions, F-actin solution, and cytolasmic solutions [48, 50, 51]. The scattered light is sensitive to very small motions [17] of the particles and therefore can capture

the dynamics of these particles in solution, for example, the motion of particles in the colloidal suspension. Similar to these techniques is the fluorescence correlation spectroscopy (FCS) technique in which a laser beam is focused on a small portion of the particle. In this way, the dynamics of a selected portion of the particle can be studied. The signals from the non-focused region of the particle are avoided [17]. Compared to other light scattering methods, the increased sensitivity of the FCS technique helps to detect the molecular structural changes, conformational changes, chemical reaction kinetics, and photophysical dynamics [52,53]. Another unique and nondestructive approach to determine the elasticity and viscosity of small particles is the ultrasound attenuation [17, 54–56]. In this method, the oscillating glass fiber serves as a sensor to produce small displacements ($1 \sim 100nm$) at its resonance frequency [54,55]. An acoustic microscope analyzes these displacements and provides the image of the particle due to changes in sound attenuation [17,54,55]. Using the sound attenuation method the mechanical properties of F-actin, microtubules and alginate microcapsules were determined [54–56].

Besides the above mentioned methods, there are a few other techniques that can be used to study the behavior of soft particles, including optical traps, optical tweezers and optical stretchers. The optical trap technique is used in different fields including the study of atoms, molecules, dielectric spheres (size $nm \sim \mu m$), cells and other microrganelles in the cells [57]. In the optical trap, a laser beam is used to apply a controlled force to a trapped particle, which is usually a silica or latex bead [17,57]. The force on the trapped particle depends upon the particle size and the relative index of refraction $n = n_p/n_m$, where n_p and n_m are the indices of the particle and the medium [17]. The stability of the trapped particle depends upon the applied field, the properties of the particle and the surrounding medium [17]. Such trappable particle or bead can be used to deform the cell membrane locally [17] to determine it mechanical

properties. Optical tweezers also use focused laser beam to trap particles or beads to deform cells and vesicles [58–60]. Lenormand *et al.* [58] used three silica beads to trap a red blood cell membrane. Using optical tweezers, the skeleton extracted from the red cell membrane was deformed by applying calibrated forces to the beads and the area expansion and shear modulus of the skeleton were measured [58]. Optical tweezers were also used to determine the deformed shape of trapped red blood cells [59] and vesicles [60]. The advantage of this technique is that these micron sized beads can be used to probe another (typically larger) particle locally with high resolution [17]. The disadvantage is that the force exerted on the particle is difficult to increase beyond $100pN$, and local heating of the trapped bead at high laser power is often not negligible [61]. The optical stretcher technique is similar to optical traps and uses two opposing non-focused laser beams to stretch a dielectric object along the axis of the beam [62]. The forces exerted by light due to momentum transfer are sufficient to hold, move and deform the object [62]. This technique has been used to measure the viscoelastic properties of dielectric materials and biological cells [62]. For example, Guck *et al.* [62] used the optical stretcher to deform human erythrocyte and mouse fibroblasts. The advantage of this method is that it is nondestructive and the force applied ranges from that applied with optical tweezers to that applied with AFM [62].

The magnetic trap method is generally used to quantify the response of particles under very small forces in the pico-newton range [63–66]. This method helps to study the deformation, rheology, and local viscoelasticity of particles. Bausch *et al.* [63] used the magnetic trap with one pole which could generate forces up to $10^4 pN$ on paramagnetic beads. These beads were then used to measure the local viscoelastic properties of the surface of adhering fibroblasts. The shear modulus found was in the range of 2×10^{-3} Pa to 4×10^{-3} Pa [63]. The bulk shear modulus estimated was 0.5×10^{-4} Pa, which was in agreement

with data obtained by AFM [63]. Amblard *et al.* [66] designed a magnetic manipulator that generated two dimensional translational and rotational motions, and they used it to study the local rheology and micromechanical properties of biological systems. The limitation of this technique is that the magnetic beads can only exert forces in the piconewton range [63–66] and torques on the order of $10^{-14}Nm$ [66]. However, the advantage is that the precisely controlled force can be used to study the local response of $\mu m-$ to $nm-$ sized particles.

The different experimental methods discussed above have been employed to understand the mechanical, chemical and biological responses of soft flexible particles. However, there is not a single method that can capture all the responses individually and the coupling between these responses. Each method has a unique approach to interpret the behavior of a particular element of the particle or the overall property of the particle. Sometimes, different methods predict different results. For example, some methods may explain the particle behavior as solid-like, while others may claim it to be liquid-like. Some may suggest that the particle's behavior is linear upon external force, while others may propose a nonlinear behavior. Some may find the particle's response elastic, while others may point out that it is viscoelastic. These differences can be due to the differences in the time scale of the measurement and in the strains at which the measurements are taken [17]. In particular, it has been observed quite often that a particle responds very differently at small and large deformation. For biological particles, current experimental techniques predict their response under controlled conditions but to capture their real response in living conditions is still a challenge. In particular, a biological particle responds both passively and actively. Sometimes, the passive response is hidden in the active response that cannot be measured through experiments. Further development in the technology is necessary to understand the complex response of soft particles both in their passive and active states.

13

1.3 Mathematical models for the mechanics of soft particles

Different experimental approaches provide insight into both internal and external properties of flexible particles. To interpret the experimental results and relate them to the properties of the particles, different theoretical models have been proposed in the literature. The ability of a model to predict the experimental observations depends upon the type of the particle under study, the size of the particle, the conditions under which measurements are taken and the suitability of the assumptions in the model. Common models describing the mechanics of soft particles and their responses in experiments are reviewed below.

A particle can be modeled as a continuum, if the operative length scale of interest is much larger than the distance over which structural or material properties change [67]. The continuum approach uses constitutive laws to describe the local stress-strain relationship. Prediction of the particle's response depends upon these constitutive laws [67]. Material properties such as isotropy or anisotropy and homogeneity or heterogeneity of the particle are incorporated in the continuum models. It has been shown that the experimentally observed response of the particle using techniques such as poking, micropipette, optical traps and magnetic manipulation can, to some extent, be captured using continuum based models. For example, the mechanical behavior of erythrocytes or neutrophils in micropipette aspiration has been captured by viscoelastic continuum models [67]. Similarly, the deformation of cells due to the controlled force from magnetic microbeads can be captured by viscoelastic continuum models, when the bead size is much larger than the mesh size of cytoskeletal network [67]. Comparison between experiments and theoretical models can help to determine the mechanical properties of particles. Schmid-Schonbein *et al.* [19] used the continuum approach and modeled

the human leukocyte as a homogenous viscoelastic body. They compared the theoretical results with the micropipette experimental results to determine the rheological properties of the leukocyte [19]. Studies on 75 neutrophils at 22°C determined the elastic coefficients $k_1 = 275 \pm 119\ dyn/cm^2$, $k_2 = 737 \pm 346$ dyn/cm^2 and viscosity coefficient $\mu = 130 + 54\ dyn \cdot s/cm^2$. Similarly, Drury *et al.* [68] used the continuum description to study the aspiration of human neutrophils into the pipette and observed that the continuum models needed to incorporate both shear thinning and surface viscosity.

Generally, the continuum models are based on one of the two theories (1) the shell theory and (2) the membrane theory. Hard-core particles that provide resistance to bending are treated as shells. Some biological structures, for example, arteries, embryos, heart, head, and eyeball can be treated as fluid-filled shells [69,73]. These particles can buckle and dimples of reversed curvature can form during buckling [69–72]. Cagan *et al.* [71] studied the large deflection of spherical shells with ring loads. The computed load-deflection curve for both thick and thin shell was compared with experimental data which showed good agreement. The results suggested that, for a spherical shell with radius R and ring load radius r_0, there existed characteristic ring load radii r_1 and r_2 with $r_1 < r_2 < R$. For $r_0 < r_1$, no buckling occurred and the load-deflection curve resembled a point-load deflection curve. For $r_1 < r_0 < r_2$ transition buckling did occur, with the load rising to the peak and then dropping towards the point-load curve. Last, for $r_2 < r_0 < R$, the shell buckled locally with abrupt change in the shape at a critical deflection. [71]. Updike *et al.* [72] studied the finite deflection and rotation of an elastic spherical shell by a rigid flat indenter. They explored two bifurcation points. The first point marked the buckling from a flat contact region to an axisymmetric dimple and the second point marked the transition from the axisymmetric dimple to an asymmetric one [72]. Taber [69, 70] studied the large deflection and rotation of fluid-filled

spherical shells and compared the computed results with experimental data on rubber shells filled with water. He observed that the deflection of the shell less than 20 percent of its radius was dominated by bending, while larger deformation was mainly due to membrane stretching because of the fluid inside the shell [69, 70]. Membrane stress becomes significant for thin shell structures that exist in many real particles, for example, gel microcapsules and plasma membranes. These particles have jelly-like structure which is very thin and can sustain significant stretches on their surface, but provide little resistance to bending. Such soft particles can be modeled as two dimensional fluid-filled membrane. Taber observed that when the thickness of a fluid-filled shell decreased to a certain extent bending became negligible and membrane stress was significant even for small deformation [70]. Some cells have a cortical layer that is very thin compared to the radius and can also be modeled using membrane theory [73].

The main limitation of the continuum based models is that they do not provide any information about the microstructure of the particle. For example, in cells, it is hard to determine the intracellular stress and strain response, unless a constitutive model is developed that can capture this behavior [67]. Using the continuum approach, it is difficult to capture the heterogeneity of the interior of the particles. Continuum models usually employ a limited number of time constants to characterize the particle's response. However, recent studies showed that there can be a continuous distribution of relaxation time constants [74]. Continuum models also cannot capture the small Brownian motion in the particle [75]. To compensate for the limitations of the continuum models, discrete models were proposed. While continuum models assume that the stress-bearing elements in the soft particle continuously fill the space, discrete models consider discrete elements and the space is not filled [76]. Among such discrete models, there is a special group which in-

volve structural members that are pre-stressed with tension to maintain their structural integrity. External forces are resisted by geometrical arrangement of these members [76]. This special class is named tensegrity by Fuller [77]. In this class of models, the particle is composed of a large number of structural members and the behavior of each member depends on the mechanical equilibrium and geometrical compatibility at every node [76]. The particle stiffness depends on the pre-stress induced in the structural members. The greater the pre-tension is, the less deformable the particle structure will be upon external loading. Any local disturbance in the tensegrity structure results in the global rearrangement of the structural members [76], which typically leads to non-linear relationship between stress and strain. The effect of local disturbance on global rearrangement of the members in the tensegrity models is quite different from the continuum models, where local disturbance produce only local response [76]. The tensegrity models have been used extensively to determine the mechanical behavior of soft particles. Three tensegrity models commonly used in cell mechanics are: (1) cortical membrane model, (2) tensed cable net model and (3) cable and strut model [76]. In the cortical membrane model, the pretension is carried by the cortical layer and balanced by cytoplasm pressure and extracellular traction. In the tensed cable net model, there is a network of cables that carries pretension to avoid buckling and structural collapse in the presence of external force [76]. This initial pretension defines prestress which is balanced by cytoplasmic swelling [76]. In the cable and strut model, the prestress is carried by cables and balanced by compression of struts. Which of these models is suitable to describe the deformability and mechanical behavior of the cell depends on the cell type and the extent of cell deformation [76, 78]. Many experimental results are consistent with the aforementioned tensegrity models. For example, microscopic analysis of cells containing microtubules and mitochondrial revealed that it behaved like a discrete structure when me-

chanical stress was applied to the cell surface [79]. Stamenovic *et al.* [78] concluded that tensegrity structural based models were more appropriate to describe the role of cytoskeleton in determining the mechanical behavior of adherent cells. Using the tensegrity structure, Volokh *et al.* [80] explained the experimentally observed linear stiffening of living cells and also predicted the transient softening behavior of cells. Like continuum models, the discrete models also have limitations. The tensegrity models may not be well suited to describe the dynamic behavior of cells and they can only explain some aspects of cell's viscoelastic behavior [78]. At large deformation, some particles behave like liquid and the tensegrity models cannot explain the liquid-like behavior of soft particles. Tensegrity models are also not applicable to the study of thermal effect in the particles.

Through studies it has been found that the mechanics of some soft particles is affected by the interaction among their molecular components (e.g., polymers, proteins, water, ions and other macromolecules). To model these particles, multiphase constitutive laws were used to represent the interaction among solids, fluids and ions [81]. For instance, biphasic (fluid-solid) or triphsaic (fluid-solid-ion) models were developed to determine the mechanical behavior of these complex particles. Micropipette aspiration and indentation experimental results were explained using biphasic theory for cells in the articular cartilage and osteo-blast-like cells [82, 83]. With the addition of ionic concentration in the model, the triphasic theory was used to describe the osmotic swelling and deformation of cells in the articular cartilage under both mechanical and chemical loads [84]. These multiphasic models are based on continuum theories and the constitutive model for each phase is selected independently to determine the particle's response [81]. Such models combined with other structural models, e.g. tensegrity models, may provide a better opportunity to understand the interplay between molecular components and

the overall response of the particle [81].

Despite the vast theoretical efforts, the models that describe the mechanics of small soft particles, especially biological particles, are still far from being mature. For some particles, due to their complex microstructures and sometimes complex loading conditions, it is difficult to find a single mechanics model that can capture all of their mechanical properties observed in experiments. There is an ongoing need for the development of models that can properly characterize the behavior of these particles without involving all the molecular details.

1.4   Thesis Contributions

As described above, understanding the behavior of soft particles in response to external mechanical stresses is critically important in many applications. It is of great interest to develop suitable models that can describe the mechanics of these particles under loading conditions relevant to practical applications. The main objective of the present thesis is to study a series of problems related to the deformation of small flexible particles under different loading conditions. The following four problems were studied in detail in this dissertation:

1. Poking of a fluid-filled particle using two conical indenters;

2. Poking of a fluid-filled particle with a conical indenter against a flat indenter;

3. Micropipette aspiration of a fluid-filled particle;

4. Adhesive contact of a fluid-filled particle driven by electrostatic forces.

The motivation behind the research presented in this thesis consists of real-life challenging situations (e.g., bruising of fruits during plucking and transportation), which we addressed by proposing a theoretical continuum model.

This model was used to solve four problems. In the first problem, we considered a simplified symmetric indentation using two sharp identical conical indenters to deform a fluid-filled spherical particle. The goal was to determine the instantaneous response of the particle during sharp symmetric indentation and lay a solid foundation for more complex, asymmetric indentation. The second problem investigates asymmetric indentation in a typical poking/indentation experiment, where the particle is either attached to a flat surface or to other particles. In the third problem, we studied the response of the particle while being aspirated by a micropipette. In the last problem, we studied the deformation of the particle due to electrostatic forces between the particle and a flat surface. Many of the soft particles used in practice carry charges on their surface. The electrostatic interaction between the particle and another charged surface can contribute significantly to the adhesion between the two surfaces. For example, the adhesion of blood cells to the capillary walls during circulation of the blood, the adhesion of charged toner particles on paper during photocopying and printing, and the adhesion of paint chemical droplets to the wall.

To study the above four problems, we adopted a nonlinear continuum approach and modeled the particle as an entity consisting of two separate continuum domains. The surface of the particle is modeled as a nonlinear membrane that cannot sustain bending, but can undergo large stretching. The membrane model is appropriate for thin shell structures whose thickness is much smaller than their radius. The interior of the particle is modeled as an incompressible fluid, which is suitable for liquids such as water. As the loading conditions in the four problems are different, the forces acting on the particle and the associated boundary conditions will be formulated separately for each problem. The major original contributions of this dissertation are:

1. Modeled the interior (i.e., incompressible fluid) and the surface of the

particle (i.e., hyper elastic membrane) separately, instead of considering the particle to be homogenous. This is a more appropriate approach to model fluid-filled particles such as cells, vesicles and microcapsules.

2. Avoided various assumptions in the literature on the deformed geometry of the particle (e.g., part of the deformed particle being spherical). This allows us to obtain the exact (not approximate) deformation of the particle from well-defined boundary value problems (BVPs). We also removed the typical assumption of small deformation, which allows us to study the response of the particle under large deformation.

3. Introduced coupling between the electrostatic interactions and deformation of the particle, which has not been studied before in the literature, but which is important for charged particles, especially biological particles.

4. Explored the ability of the membrane theory to capture experimental observations of soft particles. In fact, some of the results predicted from our model agree quantitatively with experimental results.

1.5   Thesis outline

The dissertation is organized as follows.

The general preliminaries are presented in Chapter 2. This chapter focuses on explaining the membrane theory and the formulation on the geometry, deformation, equilibrium and the constitutive relation to be used in this dissertation.

The attempt to understand the mechanical response of a fluid-filled particle in contact with rigid conical indenters is presented in Chapter 3.

The deformation of the particle during indentation using a rigid conical indenter against a flat indenter is investigated in Chapter 4.

The characterization of the particle during micropipette aspiration is provided in Chapter 5.

The adhesion of a charged flexible particle located in an electrolytic environment to an oppositely charged rigid substrate is investigated in Chapter 6.

Chapter 7 summarizes the findings of this study and recommends directions for future research.

Bibliography

[1] Y. L. Lin, D.-M. Wang, W.-M. Lu, Y.-S. Lin, and K.-L. Tung, "Compression and deformation of soft spherical particles," *Chem. Eng. Sci*, vol. 63, pp. 195–203, 2008.

[2] W.-M. Lu, K.-L. Tung, S.-M. Hung, J.-S. Shiau, and K.-J. Hwang, "Compression of deformable gel particles," *Powder. Tech.*, vol. 116, pp. 1–12, 2001.

[3] R. E. Pitt and D. C. Davis, "Finite element analysis of fluid-filled cell response to external loading," *Trans. Am. Soc. Agr. Eng.*, vol. 27, pp. 1976–1983, 1984.

[4] P. V. Liedekerke, P. Ghysels, E. Tijskens, G. Samaey, B. Smeedts, D. Roose, and H. Ramon, "A particle-based model to simulate the micromechanics of single-plant parenchyma cells and aggregates," *Phys. Biol.*, vol. 7, pp. 026006(1–13), 2010.

[5] H. X. Zhu and J. R. Melorose, "A mechanics model for the compression of plant and vegetative tissues," *J. Theor. Biol.*, vol. 221, pp. 89–101, 2003.

[6] R. E. Pitt, "Models for the rheology and statistical strength of uniformly stressed vegetative tissue," *Trans. Am. Soc. Eng.*, vol. 25, pp. 1776–1784, 1982.

[7] K. K. Liu, D. R. Williams, and B. J. Briscoe, "Compressive deformation of a single microcapsule," *Phys. Rev. E.*, vol. 54, pp. 6673–6680, 1996.

[8] R. Langer, "Drug delivery and targetting," *Nature*, vol. 392, pp. 5–10, 1998.

[9] D. J. Beebe, J. S. Moore, J. M. Bauer, Q. Yu, R. H. Liu, C. Devadoss, and B. Jo, "Functional hydrogel structures for autonomous flow control inside microfluidic channels," *Nature*, vol. 404, pp. 588–590, 2000.

[10] E. Evans and B. Kukan, "Passive material behavior of granulocyte based on large deformation and recovery after deformation tests," *Blood*, vol. 64, pp. 1028–1035, 1984.

[11] K. P. Sung, C. Dong, G. W. Schmid-Schonbein, S. Chien, and R. Skalak, "Leukocyte relaxation properties," *Biophys. J.*, vol. 54, pp. 331–336, 1988.

[12] J. Q. Feng and D. A. Hays, "A finite-element analysis of the electrostatic force on a uniformly charged dielectric sphere resting on a dielectric-coated electrode in a detaching electric field," *IEEE Trans. Ind. Appl.*, vol. 34, pp. 84–91, 1988.

[13] H. Mizes, M. Ott, E. Eklund, and D. Hays, "Small particle adhesion: measurement and control," *Coll. and Surf.*, vol. 165, pp. 11–23, 2000.

[14] H. Zhou, M. Gotzinger, and W. Peukert, "The influence of particle charge and roughness on particle-substrate adhesion," *Powd. Tech.*, vol. 135-136, pp. 82–91, 2003.

[15] P. Barmuta and K. Cywinski, "Electroseparation and efficiency of deposition during electrostatic powder coating," *J. Electro.*, vol. 51-52, pp. 239–244, 2001.

[16] M. Takeuchi, "Adhesion forces of charged particles," *Chem. Eng. Sci.*, vol. 61, pp. 2279–2289, 2006.

[17] P. Janmey and C. Schmidt, "Experimetal measurements of intracellular mechanics," in *Cytoskeletal mechanics models and measurements* (M. R. K. Mofrad and R. D. Kamm, eds.), pp. 18–49, NY, USA: Cambridge Uni. Press, 2006.

[18] W. Jones, H. Ting-Beall, G. Lee, S. Kelley, R. Hochmuth, and F. Guilak, "Alterations in the young's modulus and volumetric properties of chondrocytes isolated from normal and osteoarthritic human cartilage," *J. of Biomech.*, vol. 32, pp. 119–127, 1999.

[19] G. W. Schmid-Schonbein, K. L. Sung, H. Tozeren, R. Skalak, and S. Chien, "Passive mechanical properties of human leukocytes," *Biophys. J.*, vol. 36, pp. 243–256, 1981.

[20] K. Sung, G. Schmid-Schonbein, R. Skalak, G. Schuessler, S. Usami, and S. Chien, "Influence of physiochemical factors on rheology of human neutrophils," *Biophys. J.*, vol. 39, pp. 101–106, 1982.

[21] M. Sato, D. Theret, L. Wheeler, N. Ohshima, and R. Nerem, "Application of the micropipette technique to the measurement of cultured porcine aortic endothelial cell viscoelastic properties," *ASME J. Biomech. Eng.*, vol. 112, pp. 263–268, 1990.

[22] G. Alderborn, K. Pasanen, and C. Nystrom, "Studies on direct compression of tablets. xi. chacaracterization of particle fragmentation during compaction by permeametry measurements of tablets," *Int. J. Pharm.*, vol. 26, pp. 79–86, 1985.

[23] N. Caille, O. Thoumine, Y. Tardy, and J. Meister, "Contribution of the nucleus to the mechanical properties of endothelial cells," *J. Biomech.*, vol. 35, pp. 177–187, 2002.

[24] M. Radmacher, M. Fritz, C. M. Kacher, J. P. Cleveland, and P. K. Hansma, "Measuring the viscoelastic properties of Human Platelets with the Atomic Force Microscope," *Biophys. J.*, vol. 70, pp. 556–567, 1996.

[25] S. R. Heidemann, S. Kaech, R. E. Buxbaum, and A. Matus, "Direct obesrvations of the mechanical behaviors of the cytoskeleton in living fibroblasts," *J. Cell. Biol.*, vol. 145, pp. 109–122, 1999.

[26] C. Dong, R. Skalak, and K. L. P. Sung, "Cytoplasmic rheology of passive neutrophils," *Biorheology*, vol. 28, pp. 557–567, 1991.

[27] B. Daily, E. L. Elson, and G. I. Zahalak, "Cell poking. determination of the elastic area compressibility modulus of the erythrocyte membrane," *Biophys. J.*, vol. 45, pp. 671–682, 1984.

[28] N. O. Petersen, W. B. Mcconnaughey, and E. L. Elson, "Dependence of locally measured cellular deformability on position on the cell, temperature, and cytochalasin b," *Proc. Natl. Acad. Sci..*, vol. 79, pp. 5327–5331, 1982.

[29] Y. Lin and L. Freund, "Forced detachment of a vesicle in adhesive contact with a substrate," *Int. J. Sol. Struct.*, vol. 44, pp. 1927–1938, 2007.

[30] Q. H. Cheng, P. Liu, H. J. Gao, and Y. Zhang, "A computational modeling for micropipette-manipulated cell detachment from a substrate mediated by receptor-ligand binding," *J. Mech. Physi. Sol*, vol. 57, pp. 205–220, 2009.

[31] C. Dong, R. Skalak, K. Sung, G. Scmid-Schonbein, and S. Chien, "Passive deformation analysis of human leukocytes," *ASME J. of Biomech. Eng*, vol. 110, pp. 27–36, 1988.

[32] D. Needham and R. Hochmuth, "Rapid flow of passive neutrophils into a 4 μm pipet and measurement of cytoplasmic viscosity," *ASME J. of Biomech. Eng.*, vol. 112, pp. 269–276, 1990.

[33] E. Evan and A.Yeung, "Apparent viscosity and cortical tension of blood granulocytes determined by micropipet aspiration," *Biophys. J.*, vol. 56, pp. 151–160, 1989.

[34] E. A. Evans, R. Waugh, and L. Melnik, "Elastic area compressibility modulus of red cell membrane," *Biophys. J.*, vol. 16, pp. 585–595, 1976.

[35] J. M. Mitchison and M. M. Swann, "The mechanical properties of the cell surface i. the cell elastimeter," *J. Exp. Biol.*, vol. 31, pp. 443–460, 1954.

[36] Y. F. Dufrene, "Recent progress in the application of atomic force microscopy imaging and force spectroscopy to microbiology," *Curr. Op. Microbiol.*, vol. 6, pp. 317–323, 2003.

[37] C. A. J. Putman, K. O. V. Werf, B. G. D. Grooth, N. F. V. Hulst, and J. Greve, "Tapping model atomic force microscopy in liquid," *Appl. Phys. Lett.*, vol. 64, pp. 2454–2456, 1994.

[38] P. J. de Pablo, J. Colchero, J. Gomez-Herrero, and A. M. Baro, "Jumping mode scanning force microscopy," *Appl. Phys. Lett.*, vol. 73, pp. 3300–3302, 1998.

[39] C. A. J. Putman, K. O. van der Werf, B. G. de Grooth, N. F. V. Hulst, and J. Greve, "Viscoelasticity of living cells allows high resolution imaging by

tapping mode atomic force microscopy," *Biophys. J.*, vol. 67, pp. 1749–1753, 1994.

[40] R. E. Mahaffy, S. Pak, E. Gerde, J. Kas, and C. K. Shih, "Quantitative analysis of the viscoelastic properties of thin regions of fibroblasts using atomic force microscopy," *Biophys. J.*, vol. 86, pp. 1777–1793, 2004.

[41] R. E. Mahaffy, C. K. Shih, F. C. Mackintosh, and J. Kas, "Scanning probe-based frequencey-dependent microrheology of polymer gels and biological cells," *Phys. Rev. Lett.*, vol. 85, pp. 880–883, 2000.

[42] R. M. Hochmuth, N. Mohandas, and J. P. L. Blackshear, "Measurement of the elastic modulus for red cell membrane using a fluid mechanical technique," *Biophys. J.*, vol. 13, pp. 747–762, 1973.

[43] B. P. Helmke, D. B. Thakker, R. D. Goldman and P. F. Davies, "Spatiotemporal analysis of flow-induced intermediate filament displacement in living endothelial cells," *Biophys. J.*, vol. 80, pp. 184–194, 2001.

[44] B. P. Helmke, A. B. Rosen, and P. F. Davies, "Mapping mechanical strain of an endogenous cytoskeletal network in living endothelial cells," *Biophys. J.*, vol. 84, pp. 2691–2699, 2003.

[45] S. Weinbaum, X. Zhang, Y. Han, H. Vink, and S. C. Cowin, "Mechanotransduction and flow across the endothelial glycocalyx," *Proc. Natl. Acad. Sci.*, vol. 100, pp. 7988–7995, 2003.

[46] J. Klein-Nulend, R. G. Bacabac, J. P. Veldhuijzen, and J. J. W. V. Loon, "Microgravity and bone cell mechanosensitivity," *Adva. Space Res.*, vol. 32, pp. 1551–1559, 2003.

[47] J. G. Cao, J. P. Huang, and L. W. Zhou, "Structure of electrorhelogical fluids under an electric field and a shear flow: experiment and computer simulation," *J. Phys. Chem.*, vol. 110, pp. 11635–11639, 2006.

[48] I. Nisho, J. Peetermans, and T. Tanaka, "Microscope laser light scattering spectroscopy of single biological cells," *Cell Biophys.*, vol. 7, pp. 91–105, 1985.

[49] T. G. Mason, H. Gang, and D. A. Weitz, "Diffusing-wave-spectroscopy measurements of viscoelasticity of complex fluids," *J. Opt. Soc. Am.*, vol. 14, pp. 139–149, 1997.

[50] T. G. Mason, K. K. T. Gisler, E. Frey, and D. A. Weitz, "Rheology of f-actin solutions determined from thermally driven tracer motion," *J. Rheol.*, vol. 44, pp. 917–928, 2000.

[51] T. B. Liverpool and A. C. Maggs, "Dynamic scattering from semiflexible polymers," *Macromolecules*, vol. 34, pp. 6064–6073, 2001.

[52] W. W. Webb, "Fluorescence correlation spectroscopy: inception, biophysical experimentations, and prospectus," *Appl. Opt.*, vol. 40, pp. 3969–3983, 2001.

[53] S. T. Hess, S. Huang, A. A. Heikal, and W. W. Webb, "Biological and chemical applications of fluorescence correlation spectroscopy: A review," *Biochem.*, vol. 41, pp. 697–705, 2002.

[54] O. Wagner, J. Zinke, P. Dancker, W. Grill, and J. Bereiter-Hahn, "Viscoelasticity properties of f-actin, microtubules, f-actin/α-actinin, and f-actin/hexokinase determined in microliter volumes with a novel nondestructive method," *Biophy. J.*, vol. 76, pp. 2784–2796, 1999.

[55] O. Wagner, H. Schuler, P. Hofmann, D. Langer, P. Dancker, and J. Bereiter-Hahn, "Sound attenuation of polymerizing actin reflects supramolecular structures: viscoelastic properties of actin gels modified by cytochalasin d, profilin and α-actinin," *Biochem. J.*, vol. 355, pp. 771–778, 2001.

[56] A. Klemenz, C. Schwinger, J. Brandt, and J. Kressler, "Investigation of elasto-mechanical properties of alginate microcapsules by scanning acoustic microscopy," *J. Biomed. Mater. Res.*, vol. 65A, pp. 237–243, 2003.

[57] A. Ashkin, "Optical trapping and manipulation of neutral particles using lasers," *Proc. Natl. Acad. Sci.*, vol. 94, pp. 4853–4860, 1997.

[58] G. Lenormand, S. Henon, A. Richert, J. Simeon, and F. Gallet, "Direct measurement of the area expansion and shear moduli of the human red blood cell membrane skeleton," *Biophys. J.*, vol. 81, pp. 43–56, 2001.

[59] S. Rancourt-Grenier, M. Wei, J. Bai, A. Chiou, P. Bareil, P. Duval, and Y. Sheng, "Dynamic deformation of red blood cell in dual-trap optical tweezers," *Opt. Expr.*, vol. 18, pp. 10462–10472, 2010.

[60] J. J. Foo, K. K. Liu, and V. CHan, "Viscous drag of deformed vesicles in optical trap: Experiments and simulations," *Amer. Inst. Chem. Eng.*, vol. 50, pp. 249–254, 2004.

[61] E. J. G. Peterman, F. Gittes, and C. F. Schmidt, "Laser-induced heating in optical traps," *Biophys. J.*, vol. 84, pp. 1308–1316, 2003.

[62] J. Guck, R. Ananthakrishnan, H. Mahmood, T. J. Moon, C. C. Cunningham, and J. Kas, "The optical stretcher: A novel laser tool to micromanipulate cells," *Biophys. J.*, vol. 81, pp. 767–784, 2001.

[63] A. R. Bausch, F. Ziemann, A. A. Boulbitch, K. Jacobson, and E. Sackmann, "Local measurement of viscoelastic parameters of adherent cell surfaces by magnetic bead microrheometry," *Biophys. J.*, vol. 75, pp. 2038–2049, 1998.

[64] A. R. Bausch, W. Moller, and E. Sackmann, "Measurement of local viscoelasticity and forces in living cells by magnetic tweezers," *Biophys. J.*, vol. 76, pp. 57–579, 1999.

[65] H. Huang, C. Y. Dong, H. Kwon, J. D. Sutin, R. D. Kamm, and P. T. C. So, "Three-dimensional cellular deformation analysis with a two-photon magnetic manipulator workstation," *Biophys. J.*, vol. 82, pp. 2211–2223, 2002.

[66] F. Amblard, B. Yurke, and A. Pargellis, "A magnetic manipulator for studying local rheology and micromechanical properties of biological systems," *Rev. Sci. Instrum.*, vol. 67, pp. 818–827, 1996.

[67] M. R. K. Mofrad, H. Karcher, and R. D. Kamm, "Continuum elastic or vicoelastic models for the cell," in *Cytoskeletal mechanics models and measurements* (M. R. K. Mofrad and R. D. Kamm, eds.), pp. 71–83, NY, USA: Cambridge Uni. Press, 2006.

[68] J. L. Drury and M. Dembo, "Aspiration of human neutrophils: effects of shear thinning and cortical dissipation," *Biophys. J.*, vol. 81, pp. 3166–3177, 2001.

[69] L. A. Taber, "Large deflection of a fluid-filled spherical shell under a point load," *J. Appl. Mech.*, vol. 49, pp. 121–128, 1982.

[70] L. A. Taber, "Compression of fluid-filled spherical shells by rigid indenters," *J. Appl. Mech.*, vol. 50, pp. 717–722, 1983.

[71] J. Cagan and L. A. Taber, "Large deflection of spherical shells with ring loads," *J. Appl. Mech.*, vol. 53, pp. 897–901, 1986.

[72] D. P. Updike and A. Kalnins, "Axisymmetric behavior of an elastic spherical shell compressed between rigid plates," *J. Appl. Mech.*, vol. 37, pp. 635–640, 1970.

[73] L. Y. Cheng, "Deformation analyses in cell and development biology. part i- formal methodology," *J. Biomech. Eng.*, vol. 109, pp. 18–24, 1987.

[74] N. Desprat, A. Richert, J. Simeon, and A. Asnacios, "Creep function of a single living cell," *Biophys. J.*, vol. 88, pp. 2224–2233, 2005.

[75] A. Mogilner and G. Oster, "Cell motility driven by actin polymerization," *Biophys. J.*, vol. 71, pp. 3030–3045, 1996.

[76] D. Stamenovic, "Models of cytoskeletal mechanics based on tensegrity," in *Cytoskeletal mechanics models and measurements* (M. R. K. Mofrad and R. D. Kamm, eds.), pp. 103–128, NY, USA: Cambridge Uni. Press, 2006.

[77] R. B. Fuller, "Tensegrity," *Portfolio. Artnews annual*, vol. 4, pp. 112–127, 1961.

[78] D. Stamenovic and D. E. Ingber, "Models of cytoskeletal mechanics of adherent cells," *Biomech. Model Mechanobiol.*, vol. 1, pp. 95–108, 2002.

[79] N. Wang, K. Naruse, D. Stamenovic, J. J. Fredberg, S. M. Mijailovich, I. M. Tolic-Norrelykke, T. Polte, R. Mannix, and D. E. Ingber, "Mechanical behavior in living cells consistent with the tensegrity model," *Proc. Natl. Acad. Sci. USA*, vol. 98, pp. 7765–7770, 2001.

[80] K. Y. Volokh, O. Vilnay, and M. Belsky, "Tensegrity architecture explains linear stiffening and predicts softening of living cells," *J. Biomech.*, vol. 33, pp. 1543–1549, 2000.

[81] F. Guilak, M. A. Haider, L. A. Setton, T. A. Laursen, and F. P. T. Baaijens, "Multiphasic models of cell mechanics," in *Cytoskeletal mechanics models and measurements* (M. R. K. Mofrad and R. D. Kamm, eds.), pp. 84–102, NY, USA: Cambridge Uni. Press, 2006.

[82] F. P. T. Baaijens, W. R. Trickey, T. A. Laursen, and F. Guilak, "Large deformation finite element analysis of micropipette aspiration to determine the mechanical properties of the chondrocyte," *An. Biomed. Eng.*, vol. 33, pp. 494–501, 2005.

[83] D. Shin and K. Athanasiou, "Cytoindentation for obtaining cell biomechanical properties," *J. Orthop. Res.*, vol. 17, pp. 880–890, 1999.

[84] W. M. Lai, J. S. Hou, and V. C. Mow, "A triphasic theory for the swelling and deformation behaviors of articular cartilage," *J. Biomech. Eng.*, vol. 113, pp. 245–258, 1999.

[85] J. D. Humphrey, "Review paper: Continuum biomechanics of soft biological tissues," *Proc. R. Soc. Lond.A*, vol. 459, pp. 3–46, 2003.

Chapter 2

Mathematical formulation for the axisymmetric deformation of a fluid-filled spherical membrane

2.1 Introduction

The membrane is a structure that is commonly seen in soft particles (e.g., cells, vesicles and polymer microcapsules) [1–5]. Generally, a membrane is a continuous two dimensional manifold that encloses a space which can be empty or filled with liquid. The enclosing surface of the membrane can be a single layer or a combination of different layers. Some membranes are permeable, so liquid can be diffused inside or outside depending upon the osmotic pressure (e.g., cells and vesicles). However, some membranes are impermeable and can be used to make different microcapsules. The enclosed liquid can be single phase or multiphase. Some other microstructures can also be embedded in the liquid (e.g., polymers that can be proteins or fibers).

The material properties of the membrane structure greatly depend upon the micro-components on the surface, as well as on the enclosed fluid. For thin membranes, bending is usually negligible and stretching plays an important role in their deformation. However, for thick membranes, bending

and curvature significantly affect the deformation. For instance, Dueling *et al.* [6] explained the shape of red blood cell membrane on the basis of curvature elasticity. Bending moments can also be induced chemically in the membrane by altering the interfacial free energy densities, which changes the curvature of the membrane [7]. Some membranes may exhibit anisotropic, time-dependent and/or dissipative properties such as viscoelasticity and viscoplasticity [8]. Other membranes may also demonstrate rheological behavior and flow under shear force. Possible diffusion of materials through the membrane, molecular interactions and chemical interactions on the outside and inside the membrane all contribute to its apparent mechanical properties. The mechanics of the membrane is also affected by the extent of the deformation and by temperature. For example, different molecular components inside the membrane may have thermal coefficients that respond differently to temperature changes. Thermal fluctuations may play a role when the deformation is small. Finally, biological membranes may be in an active state and undergo continuous changes with time. Due to the complexity of features that a real membrane structure exhibits, it is not possible to consider all the mechanical and thermodynamic aspects of the membrane in a single mechanics model. To mitigate this limitation, various assumptions are set in place. In the literature, one of two assumptions is often made for the membrane. One assumes that the surface area of the membrane does not change with deformation while the volume occupied by the membrane structure varies. The other assumes that the volume stays constant allowing the surface area to change.

In this dissertation, the membrane model adopted is a continuum mechanics model subjected to the following assumptions. First, the membrane is separated into two domains, the membrane surface and the interior, each of which is occupied by a single-phased homogeneous and isotropic material. We focus on addressing equilibrium deformation of the membrane structure and

35

do not consider any time-dependent properties. Second, the surface of the membrane is assumed to be sufficiently thin so that bending can be neglected and the surface is allowed to undergo large nonlinear deformation. Third, the membrane is assumed to be impermeable and its interior is assumed to be occupied by liquid that is incompressible. When external load is applied on the membrane, deformation occurs in order to reach a new configuration in equilibrium. Under the continuum mechanics framework, the deformation can be described by the deformation gradient tensor.

Consider a body B whose material points occupy a region $R_0 \subset \mathrm{IR}^3$ in a reference configuration κ as shown in Figure 2.1(a). We label the two different yet infinitely close points P_0 and $P_1 \in R_0$ by their position vectors $\mathbf{Z}(P_0)$ and $\mathbf{Y}(P_1)$, defined by their components $\{X_1, X_2, X_3\}$ with orthonormal basis $\{E_1, E_2, E_3\}$ relative to a coordinate system. This system is referred to as Lagrangian coordinate system and the components in this system are called Lagrangian coordinates. The deformation of the body is defined by an injective mapping function χ, which maps every point in the reference configuration to a point in the deformed configuration (φ). Such a mapping function does
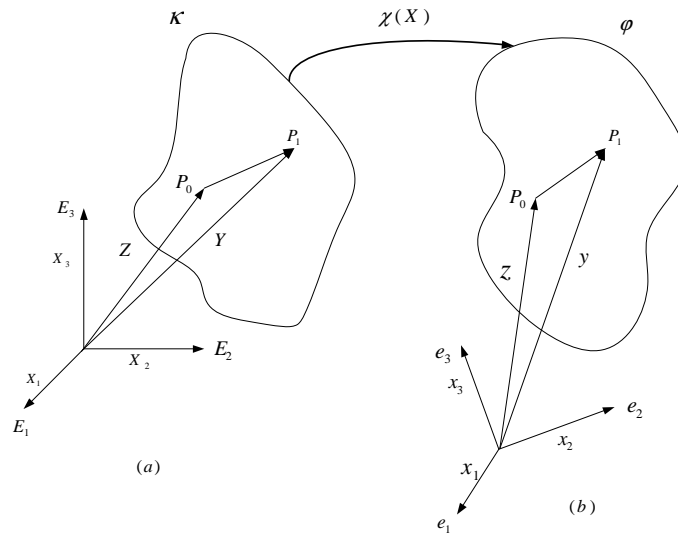
Figure 2.1: Displacement of a continuum body

36

not include the effect of tearing of material, where one-to-one mapping does not exist. $\chi(B)$ is the deformed configuration φ of the body. The material points P_0 and P_1 in the deformed configuration are represented by their position vectors $\mathbf{z}(P_0)$ and $\mathbf{y}(P_1)$, defined by their components $\{x_1, x_2, x_3\}$ with respect to orthonormal basis $\{e_1, e_2, e_3\}$. This coordinate system is referred to as Eulerian coordinate system and the components in this system are called Eulerian coordinates. In the formulation, we will use upper case letters to represent quantities in the reference configuration and lower case letters to represent quantities in the deformed configuration. The position vectors $\mathbf{z}(P_0)$ and $\mathbf{y}(P_1)$ can be written in terms of the mapping function χ as

$$\mathbf{z} = \chi(\mathbf{Z}, t), \mathbf{y} = \chi(\mathbf{Y}, t) \tag{2.1}$$

Let χ be differentiable, the relative displacement between the two vectors $\mathbf{y}$ and $\mathbf{z}$ is written as

$$\mathbf{y} - \mathbf{z} = \left.\frac{\partial \chi(\mathbf{X}, t)}{\partial \mathbf{X}}\right|_{\mathbf{Y}} (\mathbf{Y} - \mathbf{Z}) + O(|\mathbf{Y} - \mathbf{Z}|), \tag{2.2}$$

where the deformation gradient is conveniently expressed as

$$\mathbf{F} = \frac{\partial \chi(\mathbf{X}, t)}{\partial \mathbf{X}}. \tag{2.3}$$

Ignoring the high order terms in (2.2) it can be written simply as

$$\mathbf{dx} = \frac{\partial \chi(\mathbf{X}, t)}{\partial \mathbf{X}} \mathbf{dX}, \tag{2.4}$$

where $\mathbf{dX}$ and $\mathbf{dx}$ are the infinitesimal distances between two same material points in the reference and deformed configurations, respectively. $\mathbf{F}$ is the material deformation gradient tensor that describes the relationship between

elemental vectors defining neighbouring particles in the reference and deformed configuration of the body. By employing the deformation gradient tensor to all material points, the membrane can be transformed from the referential to the deformed configuration. In the following, we consider the special situation where the deformation gradient is applied to the spherical membrane as a two dimensional surface and we will consider the formulation for deformation that possesses axisymmetry, which is the focus of this dissertation.

2.2   Formulation

2.2.1   Geometry

Consider a membrane which is a sphere of radius R in the reference configuration κ (taken to be the stress-free state) as shown in Figure 2.2(a). The convected spherical coordinates $\{\phi, \theta\}$ are used to define the position of a material point $\mathbf{X}$ on the membrane surface

$$\mathbf{X} = R\mathbf{E}_R(\phi, \theta), \tag{2.5}$$

where $\{\mathbf{E}_\phi(\phi, \theta), \mathbf{E}_\theta(\theta), \mathbf{E}_R(\phi, \theta)\}$ are the standard orthonormal basis for the
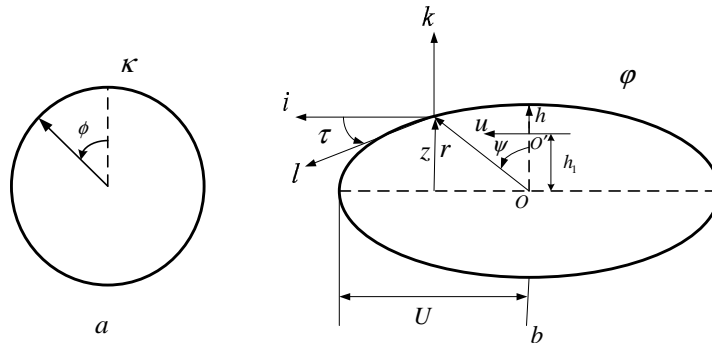
Figure 2.2: a) Reference and b) Deformed configurations

spherical coordinates in κ. The membrane is inflated to radius r_0 and then

deformed axisymmetrically by applying some external force. The position $\mathbf{x}$ of a material point X in the deformed configuration φ is located at

$$\mathbf{x}(\phi, \theta) = r(\phi)\mathbf{e}_r(\psi(\phi), \theta), \tag{2.6}$$

where the meridian angle $\psi(\phi)$ is shown in Figure 2.2(b) and $\{\mathbf{e}_\psi(\psi, \theta), \mathbf{e}_\theta(\theta), \mathbf{e}_r(\psi, \theta)\}$ are the orthonormal basis for the spherical coordinates in φ. The deformation gradient is

$$\mathbf{F} = \nabla \mathbf{x} = \mathbf{g}_\phi \otimes \mathbf{G}^\phi + \mathbf{g}_\theta \otimes \mathbf{G}^\theta, \tag{2.7}$$

where $\{\mathbf{g}_\phi, \mathbf{g}_\theta\}$ are the covariant basis in the deformed configuration φ, and $\{\mathbf{G}^\phi, \mathbf{G}^\theta\}$ are the contravariant basis in the reference configuration κ. The covariant basis on φ are defined by

$$\mathbf{g}_\phi = \frac{\partial \mathbf{x}}{\partial \phi}, \quad \mathbf{g}_\theta = \frac{\partial \mathbf{x}}{\partial \theta}, \tag{2.8}$$

and the covariant basis on κ are

$$\mathbf{G}_\phi = \frac{\partial \mathbf{X}}{\partial \phi}, \quad \mathbf{G}_\theta = \frac{\partial \mathbf{X}}{\partial \theta}. \tag{2.9}$$

The contravariant basis on κ satisfy the Kronecker Delta property

$$\mathbf{G}_i \cdot \mathbf{G}^j = \delta_i^j, \tag{2.10}$$

which means

$$\mathbf{G}^\phi \cdot \mathbf{G}_\phi = 1, \quad \mathbf{G}^\phi \cdot \mathbf{G}_\theta = 0, \quad \mathbf{G}^\theta \cdot \mathbf{G}_\phi = 0, \quad \mathbf{G}^\theta \cdot \mathbf{G}_\theta = 1. \tag{2.11}$$

Now, using (2.6) and (2.8), the calculation yields

$$\mathbf{g}_\phi = r'\mathbf{e}_r + r\psi'\mathbf{e}_\psi, \quad \mathbf{g}_\theta = r\sin\psi\mathbf{e}_\theta, \tag{2.12}$$

and using (2.5) and (2.9)

$$\mathbf{G}_\phi = R\mathbf{E}_\phi, \quad \mathbf{G}_\theta = R\sin\phi\mathbf{E}_\theta, \tag{2.13}$$

where $()' = d()/d\phi$. By (2.10), the contravariant basis on κ are

$$\mathbf{G}^\phi = \frac{\mathbf{E}_\phi}{R}, \quad \mathbf{G}^\theta = \frac{\mathbf{E}_\theta}{R\sin\phi}. \tag{2.14}$$

Now, using (2.12) and (2.14), it can be shown that, for the membrane in Figure 2.2, the deformation gradient (2.7) takes the form

$$\mathbf{F} = \frac{r'\mathbf{e}_r + r\psi'\mathbf{e}_\psi}{R} \otimes \mathbf{E}_\phi + \frac{r\sin\psi}{R\sin\phi}\mathbf{e}_\theta \otimes \mathbf{E}_\theta, \tag{2.15}$$

which can be conveniently expressed as

$$\mathbf{F} = \lambda\mathbf{l} \otimes \mathbf{L} + \mu\mathbf{m} \otimes \mathbf{M}, \tag{2.16}$$

where λ and μ are the principal stretches, $\mathbf{l}$ and $\mathbf{m}$ are orthonormal vectors in the tangent plane $T\varphi$ of the deformed configuration φ, while $\mathbf{L}$ and $\mathbf{M}$ are orthonormal vectors in the tangent plane $T\kappa$ of the reference configuration κ. Comparison of (2.15) and (2.16) yields

$$\lambda = \frac{\sqrt{(r')^2 + (r\psi')^2}}{R}, \quad \mu = \frac{r\sin\psi}{R\sin\phi},$$
$$\mathbf{l} = \frac{r'\mathbf{e}_r + r\psi'\mathbf{e}_\psi}{\lambda R}, \quad \mathbf{m} = \mathbf{e}_\theta, \quad \mathbf{L} = \mathbf{E}_\phi, \quad \mathbf{M} = \mathbf{E}_\theta, \tag{2.17}$$

and the areal dilation is given by

$$J = \sqrt{\det \mathbf{F}^T \mathbf{F}} = \lambda \mu. \tag{2.18}$$

The outward normals to $T\kappa$ and $T\varphi$ are, respectively,

$$\mathbf{N} = \mathbf{L} \times \mathbf{M}, \quad \mathbf{n} = \mathbf{l} \times \mathbf{m}. \tag{2.19}$$

As shown in Figure 2.2(b), the unit tangent vector $\mathbf{l}$ can be expressed using the standard cylindrical basis $\{\mathbf{i}(\theta), \mathbf{j}(\theta), \mathbf{k}\}$ as

$$\mathbf{l} = \cos \tau \mathbf{i} - \sin \tau \mathbf{k}, \tag{2.20}$$

where the angle τ and the basis $\{\mathbf{i}(\theta), \mathbf{j}(\theta), \mathbf{k}\}$ are shown in Figure 2.2(b). The transformation between the spherical and the cylindrical basis is

$$\mathbf{i} = \cos \psi \mathbf{e}_\psi + \sin \psi \mathbf{e}_r, \quad \mathbf{j} = \mathbf{e}_\theta, \quad \mathbf{k} = -\sin \psi \mathbf{e}_\psi + \cos \psi \mathbf{e}_r. \tag{2.21}$$

Substituting (2.21) into (2.20) and, subsequently, into (2.17)$_3$ (the third equation of (2.17)), the first order ordinary differential equations (ODEs) for $r'(\phi)$ and $\psi'(\phi)$ are, respectively,

$$r' = \lambda R \sin(\psi - \tau), \quad \psi' = \frac{\lambda R}{r} \cos(\psi - \tau). \tag{2.22}$$

2.2.2 Equilibrium

The equilibrium equation of the membrane is given by

$$\text{Div } \mathbf{P} + J\mathbf{f} = \mathbf{0}, \tag{2.23}$$

41

where Div is the two dimensional divergence operator on the reference configuration κ, $\mathbf{P}$ is the first Piola-Kirchhoff stress tensor, J is the areal dilation and $\mathbf{f}$ is the body force and lateral traction per deformed area. For simple hyperelastic material, $\mathbf{P}$ is equal to the gradient w.r.t $\mathbf{F}$ of the strain energy density function $W(\mathbf{F})$ on κ

$$\mathbf{P} = W_{\mathbf{F}}. \tag{2.24}$$

The strain energy density is a scalar function that relates the strain energy density of the material to the deformation gradient. The strain energy density function depends on the deformation gradient through the symmetric right Cauchy-Green deformation tensor, which is expressed in its spectral form by [9]

$$\mathbf{C} = \mathbf{F}^T\mathbf{F} = \lambda^2 \mathbf{L} \otimes \mathbf{L} + \mu^2 \mathbf{M} \otimes \mathbf{M}. \tag{2.25}$$

For an isotropic membrane, the strain energy density function simplifies to a symmetric function of the principal stretches λ and μ as

$$W(\mathbf{F}) = \overline{W}(\mathbf{C}) = w(\lambda, \mu) = w(\mu, \lambda). \tag{2.26}$$

Considering (2.16), (2.24) and (2.26), the first Piola-kirchhoff stress tensor can be written as

$$\mathbf{P} = w_\lambda \mathbf{l} \otimes \mathbf{L} + w_\mu \mathbf{m} \otimes \mathbf{M}, \tag{2.27}$$

where $w_\lambda = \frac{\partial w}{\partial \lambda}$ and $w_\mu = \frac{\partial w}{\partial \mu}$. By (2.27), the divergence of $\mathbf{P}$ is

$$\text{Div}\,\mathbf{P} = \frac{(w_\lambda)'\mathbf{l} + w_\lambda \mathbf{l}'}{R} + \frac{w_\lambda \cos\phi\,\mathbf{l} - w_\mu \mathbf{i}}{R\sin\phi}. \tag{2.28}$$

If the membrane is filled with fluid and the particle is small enough so that the effect of gravity can be neglected, the equilibrium of the fluid inside the membrane requires that div $\boldsymbol{\sigma}_f = \mathbf{0}$, which means that the pressure in the fluid

is constant. That is, the fluid Cauchy stress tensor takes the spherical form $\boldsymbol{\sigma}_f = -p_f \mathbf{I}$, where p_f is the fluid pressure and $\mathbf{I}$ is the identity tensor. This means that the traction exerted on the membrane by the fluid is

$$\mathbf{f}_f = p_f \mathbf{n}. \tag{2.29}$$

Depending on the loading conditions, there can be other traction acting on the membrane, which will be discussed in each individual chapter.

2.2.3 Constitutive relationship

While the above formulation applies to any hyperelastic material, in this work we adopt the strain energy function for the neo-Hookean material as [9]

$$w(\lambda, \mu) = \frac{G}{2} \left(\lambda^2 + \mu^2 + (\lambda\mu)^{-2} - 3 \right), \tag{2.30}$$

where G is a material constant with a dimension of energy per unit area. The relevant derivatives of $w(\lambda, \mu)$ are

$$w_\lambda = G \left(\lambda - \frac{1}{\lambda^3 \mu^2} \right), w_\mu = G \left(\mu - \frac{1}{\lambda^2 \mu^3} \right), w_{\lambda\lambda} = G \left(1 + \frac{3}{\lambda^4 \mu^2} \right), w_{\lambda\mu} = \frac{2G}{(\lambda\mu)^3}. \tag{2.31}$$

Since the membrane cannot sustain any negative stress, the conditions $w_\lambda \geqslant 0$ and $w_\mu \geqslant 0$ need to hold everywhere in the membrane [9]. If w_λ or w_μ are found to be negative, then, physically, this corresponds to wrinkling of the membrane and the equilibrium solution is not physically admissible. The spherical membrane with initial radius R is first inflated by the enclosed fluid to radius r_0. For such homogeneous deformations $\psi = \tau = \phi$, since the sphere is mapped into another sphere, and the principle stretches are $\lambda = \mu = \lambda_i = \frac{r_0}{R}$. Using (2.23), (2.28), (2.29) and (2.31), the initial pressure in the fluid can be

found to be

$$p_f^0 = \frac{2G}{r_0} \left(1 - \left(\frac{R}{r_0} \right)^6 \right).$$

(2.32)

The deformation of the fluid-filled membrane is also governed by the constitutive law for the fluid which determines the pressure in the fluid. In this work, the fluid is taken to be incompressible, which is an assumption commonly used when the bulk stiffness of the fluid is much larger than the stiffness of the membrane. The fluid pressure p_f in the deformed membrane is determined by the incompressibility condition

$$J_f = \frac{V}{V_0} = 1,$$

(2.33)

where $V_0 = \frac{4}{3}\pi r_0^3$ is the volume of the inflated spherical membrane before any further deformation. V is the volume of the fluid enclosed in the membrane after it has been deformed and can be calculated in several ways, for example

$$V = \pi \int_{Z_{min}}^{Z_{max}} u^2 dz,$$

(2.34)

where $u = r\sin(\psi)$ and $z = r\cos(\psi)$ as indicated in Figure 2.2(b).

The above formulation applies to any axisymmetric loading on the fluid-filled membrane. In each of the following chapters, where a particular loading is given, corresponding ODEs and boundary conditions governing the deformation of the membrane will be derived, and the numerical procedure to solve the BVP will be described.

Bibliography

[1] J. D. Humphrey, "Review paper: Continuum biomechanics of soft biological tissues," *Proc. R. Soc. Lond.A*, vol. 459, pp. 3–46, 2003.

[2] C. Dong and R. Skalak, "Leukocyte deformability: finite element modeling of large viscoelastic deformation ," *J. Theor. Biol.*, vol. 158, pp. 173–193, 1992.

[3] Y. Lin and L. B. Freund, "Forced detachment of a vesicle in adhesive contact with a substrate," *Int. J. Sol. Struct.*, vol. 44, pp. 1927–1938, 2007.

[4] K. K. Liu, D. R. Williams and B. J. Briscoe, "Compressive deformation of a single microcapsule," *Phys. Rev. E.*, vol. 54, pp. 6673–6680, 1996.

[5] M. Rachik, D. Barthes-Biesel, M. Carin and F. Edwards-Levy, "Identification of the elastic properties of an artifical capsule membrane with the compression test: effect of thickness," *J. Colloid Interface Sci.*, vol. 301, pp. 217–226, 2006.

[6] H. J. Dueling and W. Helfrich, "Red blood cell shapes as explained on the basis of curvature elasticity," *Biophy. J.*, vol. 16, pp. 861–868, 1976.

[7] E. A. Evans, "Bending resistance and chemically induced moments in membrane bilayers," *Biophy. J.*, vol. 14, pp. 923–931, 1974.

[8] E. Evans and R. Skalak, "Mechanics and thermodynamics of biomembranes," CRC Press Florida, 1980.

[9] B. Nadler, "On the contact of a spherical membrane enclosing a fluid with rigid parallel planes," *Int. J. Non-Linear Mech.*, vol. 45, pp. 294–300, 2010.

Chapter 3

Contact of a fluid-filled spherical membrane with rigid conical indenters[1]

3.1 Introduction

Membrane-fluid structures have much resemblance to biological cells. Modern advanced techniques have been used to poke and microinject foreign material into biological cells. The determination of the mechanical properties of plant cells was obtained in [1] by studying cell poking. Also, the turgor pressure inside the cells can be measured using cell poking based on experimental data. Microinjection model based on membrane model was proposed in [2] to predict the mechanical response of cell when foreign material is injected. This chapter focuses on the mechanical response of a spherical fluid-filled membrane when it is brought into contact with two rigid conical indenters in a symmetric manner. For simplicity, it is assumed that the membrane is homogenous, elastic and isotropic, and the fluid is incompressible.

Large elastic deformation of inflated circular plate was studied in [3] by assuming uniform pressure on one side. In [4], the deformation of a spherical shell compressed between rigid plates was analyzed and conditions for

---

[1] A version of this chapter was published. Touqeer Sohail and Ben Nadler, Acta Mech, 218 , 225-235, 2011.

47

buckling were determined. The contact of an initially flat circular membrane with a smooth and rigid spherical indenter were discussed in [5], where the axisymmetric deformations were analyzed. The general formulation of a flat neo-Hookean membrane was presented in [6]. Mooney-Rivlin material model was used in [7] to analyze the deformed configurations of an inflated nonlinear membrane from an initially flat configuration. When Mooney-Rivlin material model [7] was reduced to neo-Hookean material, the results in [7] agreed with [6]. The contact problem of an inflated spherical membrane with flat rigid plates was discussed in [8] using Mooney-Rivlin material and instability of the membrane under large deformations was studied. The shape of the contact region and the deformed configuration of the initially flat membrane was also studied in [9] by employing the energy method. In [10], the large deflection of fluid filled spherical shells were studied and compared with two analytical models (based on the shell theory and the membrane model). Recently, in [11], a general formulation for the axisymmetric deformation of spherical membrane-fluid structure in contact with two parallel planes was derived. It was also observed in [12] that, under proper conditions, the membrane stress can be reduced and loss of stability can occur in the form of wrinkling. Three different theories not restricted to small strains were considered in [13] to determine the equilibrium configuration and a comparison between the theories was provided.

In this thesis, the mechanical response of a spherical membrane-fluid structure subjected to poking by conical indenters is presented. Generalization to the formulation in [12] is introduced to include a non-flat indenter. The current study provides more realistic data regarding the forces, stress distribution and fluid pressure in biological cells subjected to poking.

The present chapter is organized as follows: Section 3.2 presents the model description of a fluid-filled spherical membrane, the equilibrium equation, the

constitutive relation and the contact conditions during indentation with rigid conical indenters. The numerical procedure is discussed in Section 3.3. The results and discussion are presented in Section 3.4 and conclusions are given in Section 3.5.

3.2 Formulation

3.2.1 Governing ODEs

The membrane is a sphere of radius R in the reference configuration κ. In the deformed configuration φ, the membrane is inflated to a radius r_0 $(r_0 > R)$ and then indented using two rigid conical indenters in a symmetric manner. Both the referential and deformed configuration of the membrane are shown in Figure 3.1. The kinematics and equilibrium equations for a fluid-filled spherical membrane are explained in detail in section 2.2. Therefore, in this section we will present briefly the governing equations required to formulate this problem.
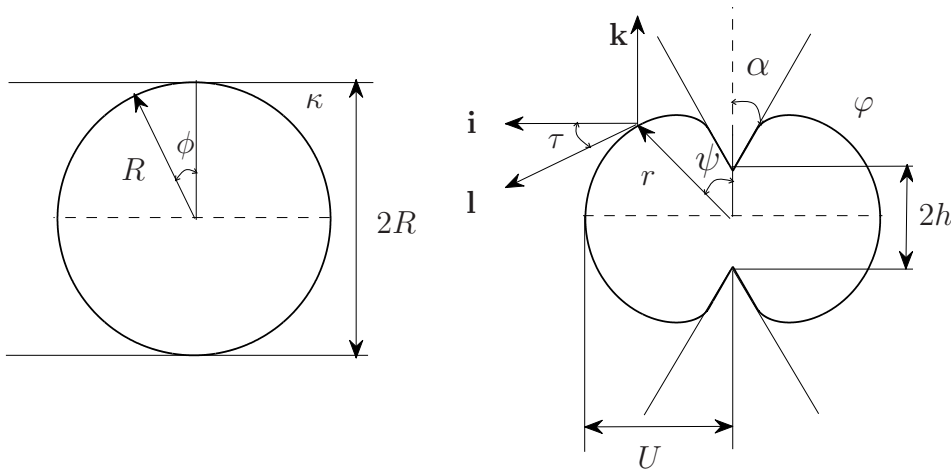
Figure 3.1: a) Reference and b) Deformed configurations

The geometry of the deformed membrane is represented by two first-order

ODEs for $r'(\phi)$ and $\psi'(\phi)$

$$r' = \lambda R \sin(\psi - \tau), \tag{3.1a}$$

$$\psi' = \frac{\lambda R}{r} \cos(\psi - \tau), \tag{3.1b}$$

which are explained in Chapter 2.

Assuming that the rigid indenters that exert force on the membrane are frictionless, the traction exerted on the membrane by the rigid indenter is normal to the membrane

$$\mathbf{f}_c = -p_c \mathbf{n}, \tag{3.2}$$

where p_c is the contact pressure between the membrane and indenters, and its direction is opposite to the outward normal $\mathbf{n}$. p_c vanishes on the part of the membrane not in contact with the indenters. Substituting Equations (2.28), (2.29) and (3.2) into the equilibrium equation (2.23) yields

$$\frac{(w_\lambda)'\mathbf{l} + w_\lambda \mathbf{l}'}{R} + \frac{w_\lambda \cos\phi\,\mathbf{l} - w_\mu \mathbf{i}}{R \sin\phi} + \lambda\mu(p_f - p_c)\mathbf{n} = \mathbf{0}. \tag{3.3}$$

Employing the properties

$$\mathbf{l}\cdot\mathbf{l} = \mathbf{n}\cdot\mathbf{n} = 1, \quad \mathbf{l}\cdot\mathbf{n} = 0, \quad \mathbf{l}\cdot\mathbf{i} = \cos\tau, \quad \mathbf{n}\cdot\mathbf{i} = \sin\tau, \quad \mathbf{l}'\cdot\mathbf{l} = 0, \quad \mathbf{l}'\cdot\mathbf{n} = -\tau',$$
$$\tag{3.4}$$

the projection of (3.3) onto the $\mathbf{l}$ and $\mathbf{n}$ directions decomposes (3.3) into two first order ODEs

$$(w_\lambda)' + \frac{w_\lambda \cos\phi - w_\mu \cos\tau}{\sin\phi} = 0, \quad \lambda\mu R(p_f - p_c) - w_\lambda\tau' - \frac{w_\mu \sin\tau}{\sin\phi} = 0. \tag{3.5}$$

By virtue of (2.26),

$$(w_\lambda)' = w_{\lambda\lambda}\lambda' + w_{\lambda\mu}\mu' \tag{3.6}$$

50

and by using $(2.17)_2$ and (2.22), it can be shown that

$$\mu' = \frac{\lambda \cos \tau - \mu \cos \phi}{\sin \phi}. \tag{3.7}$$

Substituting (3.7) into (3.6), and subsequently, into (3.5), the equilibrium equations can be conveniently expressed as two first order ODEs for λ and τ

$$\lambda' = \frac{(w_\mu - \lambda w_{\lambda\mu}) \cos \tau - (w_\lambda - \mu w_{\lambda\mu}) \cos \phi}{w_{\lambda\lambda} \sin \phi}, \tag{3.8}$$

$$\tau' = \frac{\lambda \mu R(p_f - p_c)}{w_\lambda} - \frac{w_\mu \sin \tau}{w_\lambda \sin \phi}. \tag{3.9}$$

Now, we have the four ODEs that govern the deformed geometry and equilibrium of the membrane which are (3.1a), (3.1b), (3.8) and (3.9).

3.2.2 Boundary and contact conditions

Due to the symmetry of the problem with respect to the plane defined by $\phi = \frac{\pi}{2}$, it is sufficient to consider only the domain $0 \leq \phi \leq \frac{\pi}{2}$. The boundary conditions at $\phi = 0$ are

$$\psi(0) = 0, \quad \tau(0) = \alpha - \frac{\pi}{2}, \tag{3.10}$$

where α is the angle of the conical indenter depicted in Figure 3.1. At the boundary $\phi = \frac{\pi}{2}$, the conditions are

$$\psi(\frac{\pi}{2}) = \frac{\pi}{2}, \quad \tau(\frac{\pi}{2}) = \frac{\pi}{2}, \tag{3.11}$$

which are associated with the symmetry about the horizontal plane defined by $\phi = \frac{\pi}{2}$.

The membrane domain is decomposed into two parts, one in contact with the indenter and the other not in contact. The interface between the two

domains is defined by the value of the convected coordinate ϕ and is labeled by $\phi_c \in (0, \frac{\pi}{2})$. On the part of the membrane in contact with the indenter, $0 \leqslant \phi < \phi_c$, $\tau = \alpha - \frac{\pi}{2}$ and $\tau' = 0$. Hence, using (3.9), the contact pressure p_c between the membrane and indenter can be evaluated by

$$p_c = p_f - \frac{w_\mu \sin(\alpha - \frac{\pi}{2})}{\lambda \mu R \sin \phi}. \tag{3.12}$$

Moreover, the presence of concentrated force at the pole is indicated by the discontinuity of the normal to the tangent plane of the membrane at this point. The height of the indenter h, as depicted in Figure 3.1(b), provides the initial value of the radius, r, at $\phi = 0$, such that

$$r(0) = h. \tag{3.13}$$

A simple geometrical relationship (Law of Sines) furnishes an algebraic expression for the radius, r, in the part of the membrane in contact as

$$r = h \frac{\sin(\pi - \alpha)}{\sin(\alpha - \psi)}, \tag{3.14}$$

and (3.1b) is expressed as

$$\psi' = \frac{\lambda R \sin^2(\alpha - \psi)}{h \sin(\pi - \alpha)}. \tag{3.15}$$

On the part of the membrane not in contact, $\phi_c < \phi \leqslant \frac{\pi}{2}$, the contact pressure between the indenter and the membrane, p_c, in (3.9) vanishes, which furnish the governing equation for τ

$$\tau' = \frac{\lambda \mu R p_f}{w_\lambda} - \frac{w_\mu \sin \tau}{w_\lambda \sin \phi}. \tag{3.16}$$

The resultant vertical force between the conical indenter and the membrane

due to the contact pressure and the concentrated force can be evaluated by global equilibrium of the membrane domain $0 \leqslant \phi \leqslant \frac{\pi}{2}$ as

$$F = \pi U^2 p_f - 2\pi RT, \tag{3.17}$$

where $U = u(\frac{\pi}{2})$ as shown in Figure 3.1 and $T = w_\lambda(\frac{\pi}{2})$ is the meridian traction per referential length at $\phi = \frac{\pi}{2}$.

Two different sets of equations govern the equilibrium in the parts of the membrane in contact and not in contact with the indenter. On the part of the membrane in contact, $0 \leqslant \phi < \phi_c$, $\tau = \alpha - \frac{\pi}{2}$ and the governing equations to determine $\{\lambda, \psi, r\}$ are

$$\lambda' = \frac{(\lambda w_{\lambda\mu} - w_\mu) \sin \alpha + (\mu w_{\lambda\mu} - w_\lambda) \cos \phi}{w_{\lambda\lambda} \sin \phi}, \tag{3.18}$$

(3.15), and the algebraic equation (3.14). On the part of the membrane not in contact with the indenter, $\phi_c < \phi \leqslant \frac{\pi}{2}$, the governing equations to determine $\{\lambda, \tau, \psi, r\}$ are the four first order ODEs (3.1a), (3.1b), (3.8) and (3.16). These first order ODEs are accompanied by boundary conditions $(3.10)_1$ and (3.11). In additions, on the interface, ϕ_c, between the two parts of the membrane, $\{\lambda, \tau, \psi, r\}$ are continuous [12]. It should be noted that the value of ϕ_c is not known a priori and is part of the solution to the BVP.

3.2.3 Constitutive relationship

To finalized the mathematical model of the membrane-fluid structure, the strain energy function of the membrane needs to be specified. Here, we adopt the well-known neo-Hookean model

$$w(\lambda, \mu) = \frac{G}{2} \left(\lambda^2 + \mu^2 + (\lambda\mu)^{-2} - 3 \right), \tag{3.19}$$

where w is the strain energy function and G is the ground-state shear modulus of the membrane. For the equilibrium configuration to be physically admissible [12], the requirements $w_\lambda \geqslant 0$, $w_\mu \geqslant 0$ need to hold everywhere in the membrane. In the deformed configuration, the fluid pressure is computed by satisfying the incompressibility condition

$$J_f = \frac{V}{V_0} = 1, \qquad (3.20)$$

where V is the volume of the enclosed fluid and $V_0 = \frac{4}{3}\pi r_0^3$ is the volume of the fluid in the inflated spherical membrane. The volume of the enclosed fluid in the deformed membrane is evaluated by

$$V = 4\pi \int_0^U zu\,du, \qquad (3.21)$$

where $z = r\cos\psi$ as shown in Figure 3.1.

3.3 Numerical Algorithm

The shooting method based on standard Euler forward differencing with a suitable mesh spacing $\Delta\phi$ is used to solve numerically the governing equations in the contact and non-contact domains of the membrane. Due to the discretization of the membrane (required by the numerical solution) it is preferred numerically to control the parameter ϕ_c such that it coincides with the membrane discretization. A sequence of equilibrium configurations is obtained for various prescribed values of ϕ_c, and the corresponding indenter height h is computed. In this method, the boundary conditions $\psi(\frac{\pi}{2}) = \frac{\pi}{2}, \tau(\frac{\pi}{2}) = \frac{\pi}{2}$ are satisfied by determining the associated initial conditions

$$r(0) = h, \quad \lambda(0) = \lambda_0, \qquad (3.22)$$

where h and λ_0 are unknowns. After $\{\lambda, \tau, \psi, r\}$ are obtained, the other principal stretch μ can be determined from equation $(2.17)_2$ and the principal stresses can be calculated from equation (2.27).

3.4 Results and Discussion

The equilibrium configurations of the membrane-fluid structure at various conical indenter angles are depicted in Figure 3.2 for the same indenter height, where the following normalize parameters are used

$$\bar{r}_0 = \frac{r_0}{R}, \quad \bar{h} = \frac{h}{r_0}, \quad \bar{u} = \frac{u}{r_0}, \tag{3.23}$$

and the normalized indenter displacement is defined as

$$\bar{d} = 1 - \bar{h}. \tag{3.24}$$

In the considered deformations, the membrane is compressed by identical in-
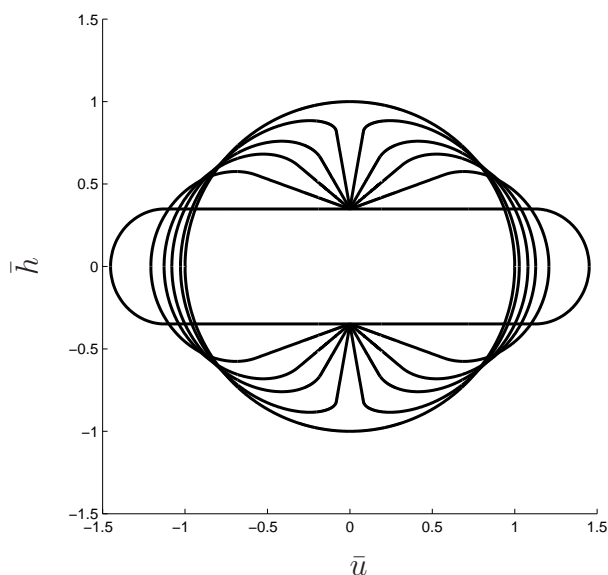
Figure 3.2: Equilibrium configurations of the membrane-fluid structure at various indenter angles for $\bar{r}_0 = 2$ and $\bar{h} = 0.35$.
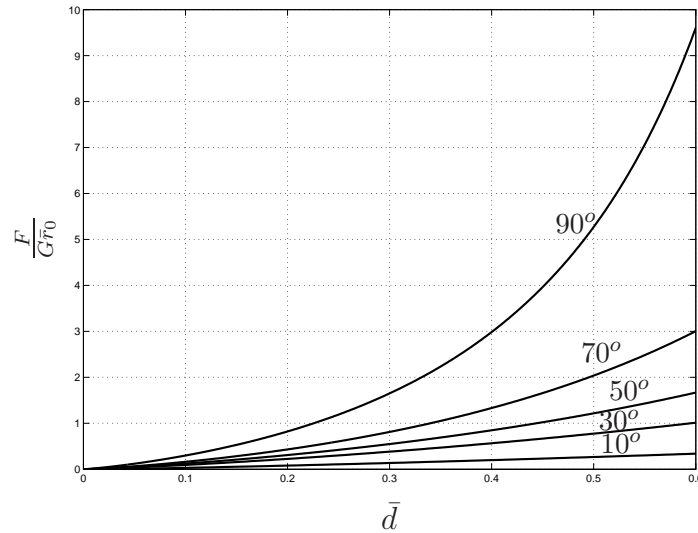
Figure 3.3: The force applied by the indenter on the membrane-fluid structure vs. indenter displacement for various indenters $\alpha = \{90^o, 70^o, 50^o, 30^o, 10^o\}$ and $\bar{r}_0 = 2$.

denters from both sides in the vertical direction, and as a result, it moves outward circumferentially. The dependency of the vertical contact force applied on the membrane-fluid structure by the indenter on the indenter displacement and angle is depicted in Figure 3.3. The indenter force increases nonlinearly with the indentation. As the sharpness of the indenter increases (indenter angle decreases), the force required to indent the membrane decreases. In Figure 3.4, the fluid pressure as a function of the indenter displacement is shown. It can be observed that the fluid pressure increases as the indenting process advances. Also, the fluid pressure decreases as the indenter sharpness increases. Figure 3.5 depicts the dependence of the contact radius on the vertical displacement of the indenter. The contact radius increases with indenter displacement until the two indenters meet each other at the geometrical center. Decrease in indenter sharpness results in an increase in the contact radius.

In Figure 3.6, the principal first Piola-Kirchhoff stresses are plotted as a function of position at a given indentation of $\bar{d} = 0.65$ for various indenters, where P_i is the magnitude of the first Piola-Kirchhoff stress in the inflated spherical membrane. It should be noted that for a flat indenter, the principal

56
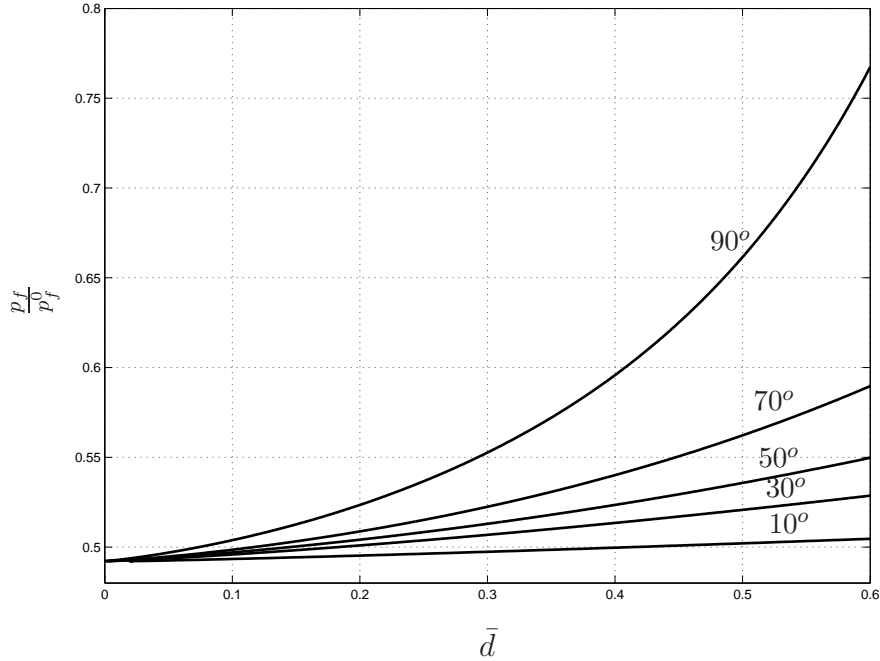
Figure 3.4: Fluid pressure vs. indenter displacement for various indenters $\alpha = \{90^o, 70^o, 50^o, 30^o, 10^o\}$ and $\bar{r}_0 = 2$.
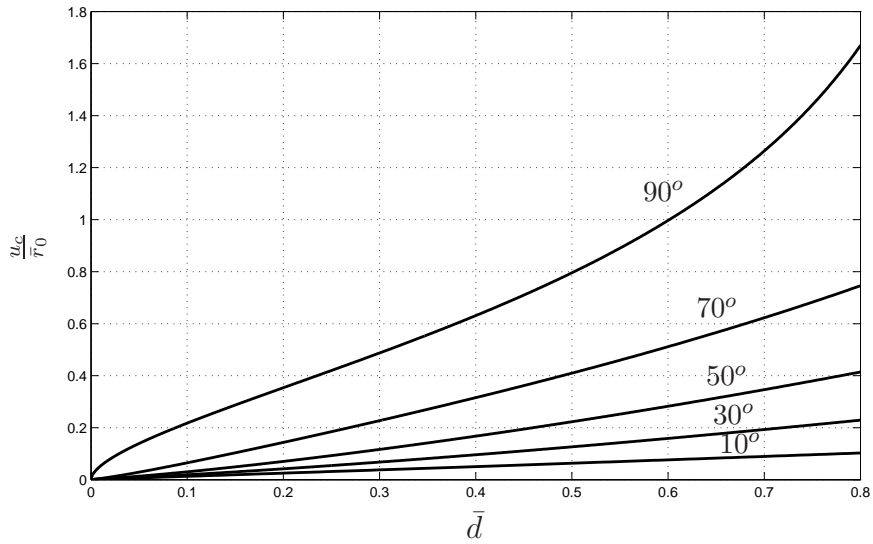
Figure 3.5: Contact radius vs. indenter displacement for various indenters $\alpha = \{90^o, 70^o, 50^o, 30^o, 10^o\}$ and $\bar{r}_0 = 2$.

stresses increase from poles to the equator, such that, the lowest stresses are located at the pole while the largest stresses are at the equator. As the sharpness of the indenter increases (α decreases), the first Piola-Kirchhoff principal
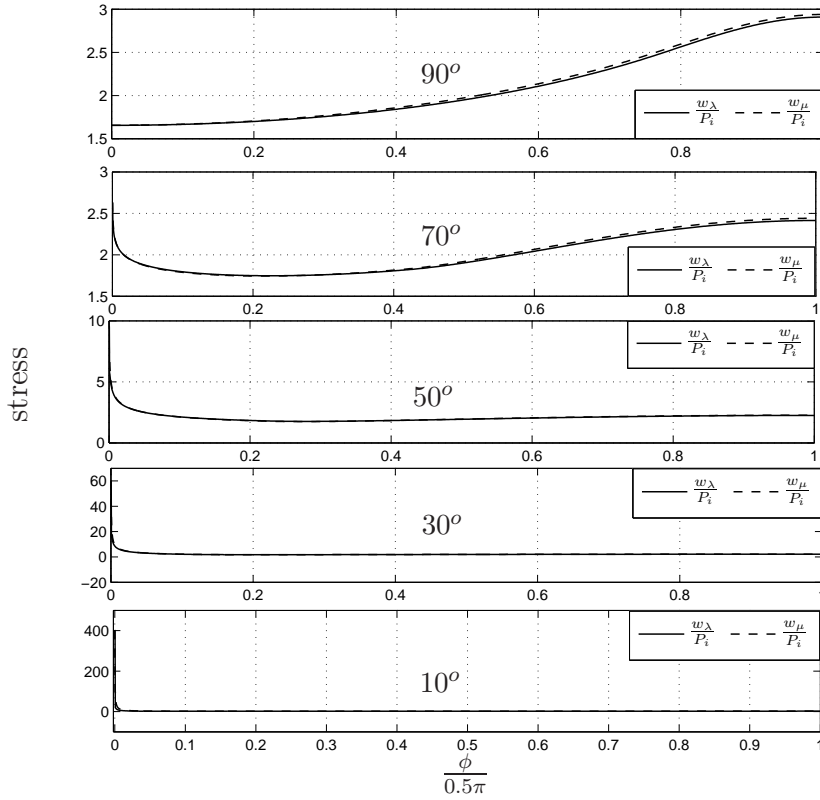
Figure 3.6: Distribution of principal first Piola-Kirchhoff stresses in the membrane at $\bar{d} = 0.65$ for various indenters $\alpha = \{90^o, 70^o, 50^o, 30^o, 10^o\}$ and $\bar{r}_0 = 2$.

stresses about the pole increase significantly and the stresses are much smaller and approximately constants away from the pole. Thus, the maximum first Piola-Kirchhoff principal stresses are located at the poles, if conical indenter is used, and located at the equator, if flat indenter is used.

Figure 3.7 and Figure 3.8 depict the first Piola-Kirchhoff principal stresses and stretches for different initial inflations $\bar{r}_0 = \{1.03, 1.5, 2.0\}$ and flat indenter at a given indentation of $\bar{d} = 0.65$, where λ_i is the principal stretch in the inflated spherical membrane. For large initial inflation, the stress distribution in the compressed membrane is close to equibiaxial stretch, but for small initial inflation, the two principal stresses and stretches differ.

In Figure 3.9, the first Piola-Kirchhoff stress at the pole, P_0, is plotted as a function of the indenter displacement for various indenters. It is observed that the stress distribution in the membrane has strong dependency on the sharpness of the indenter. For flat indenter, the pole stress remains approxi-

58
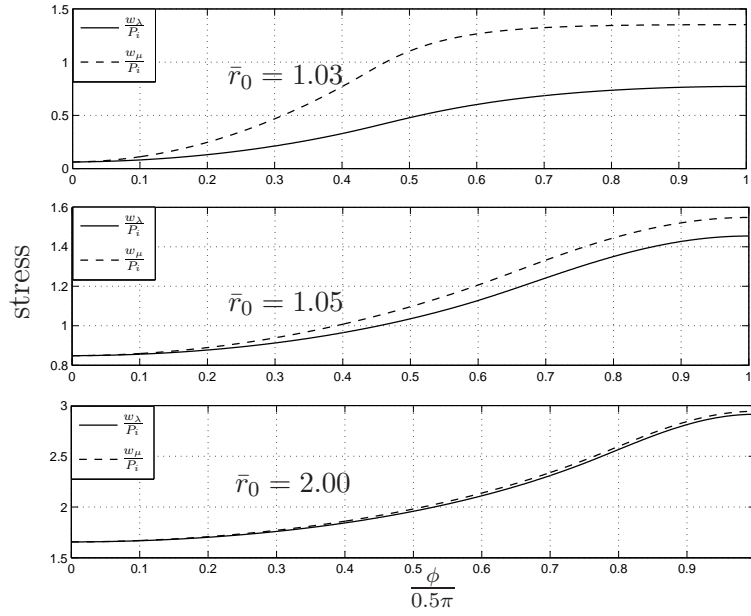
Figure 3.7: Distribution of principal first Piola-Kirchhoff stresses in the membrane at $\bar{d} = 0.65$ for different initial inflations and flat indenter ($\alpha = 90^o$).
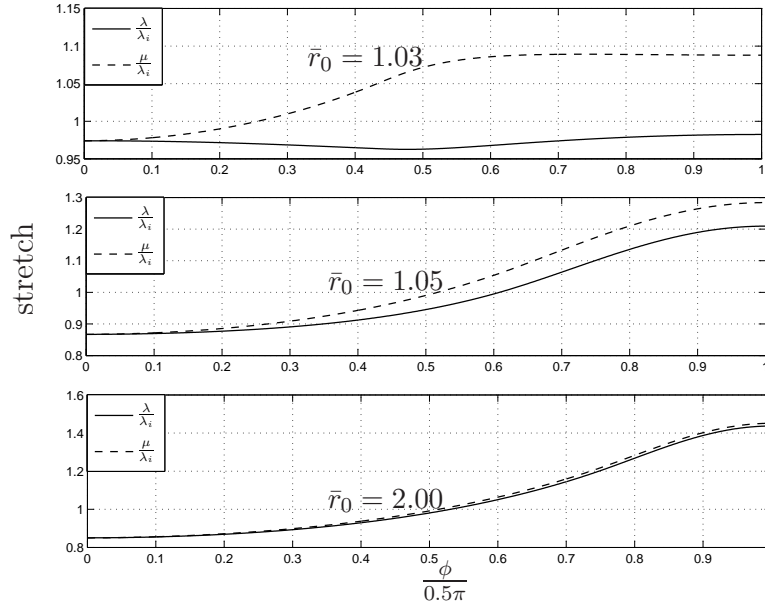
Figure 3.8: Principal stretches in the membrane at $\bar{d} = 0.65$ for different initial inflations and flat indenter ($\alpha = 90^o$).

mately constant through the indentation process and increases only at the last stage of indentation. However, for conical indenter, the pole stress increases initially and then remains approximately constant and even decreases at the end of the indentation process.
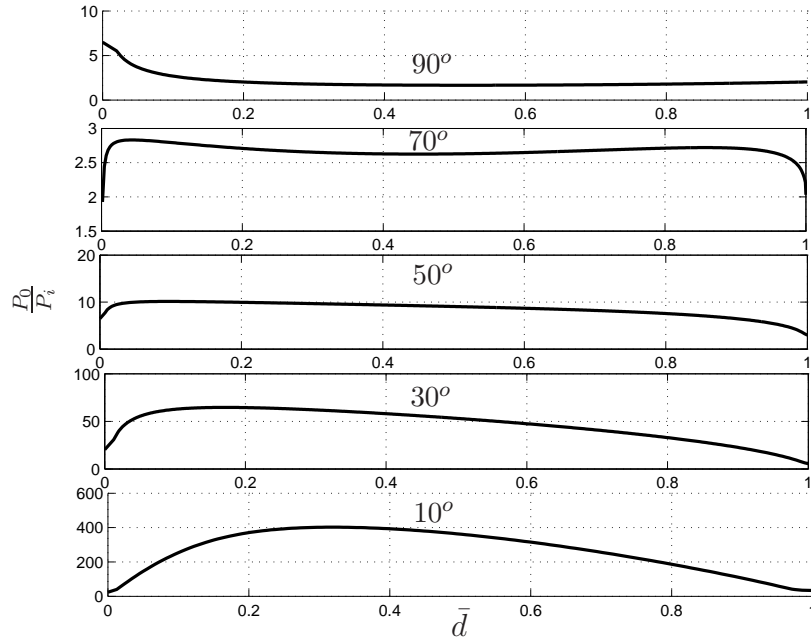
Figure 3.9: First Piola-Kirchhoff stress at the pole vs. indenter dissplacement for various indenters $\alpha = \{90^o, 70^o, 50^o, 30^o, 10^o\}$ and $\bar{r}_0 = 2$.

3.5   Conclusions

The contact problem of two rigid conical indenters with a spherical membrane-fluid structure undergoing large deformation was analyzed. The results obtained in this study can be used to determine the turgor pressure in a cell during indentation and can be used to detect the mechanical properties of the membrane in biological cells using a simple poking experiment. This can be done by matching the constitutive law of the membrane with experimental data on the structural stiffness of the cell under poking. It was shown that the stress distribution in the membrane has strong dependency on the sharpness of the indenter, which can be used for microinjection of foreign material into cells where knowledge of the stress distribution and the location of the minimum stress are important.

Bibliography

[1] R. Wang, Q.-Y. Jiao, and D.-Q. Wei, "Mechanical response of single plant cells to cell poking: A numerical simulation model," *J. Integrative Plant Biology*, vol. 48, pp. 700–705, 2006.

[2] Y. Tan, D. Sun, W. Huang, and S. H. Cheng, "Mechanical modeling of biological cells in microinjection," *IEEE Transactions on NanoBioscience*, vol. 7, pp. 257–266, 2008.

[3] J. Adkins and R. Rivlin, "Large elastic deformations of isotropic materials ix: The deformation of thin shells," *Philosophical Transactions of the Royal Society, London Series A*, vol. 244, pp. 505–531, 1952.

[4] D. Updike and A. Kalnins, "Axisymmetric behavior of an elastic spherical shell compressed between rigid plates," *ASME J. Appl. Mech*, vol. 37, pp. 635–640, 1970.

[5] W. H. Yang and K. Hsu, "Indentation of a circular membrane," *ASME J. Appl. Mech*, vol. 38, pp. 227–230, 1971.

[6] W. H. Yang and C. Lu, "General deformations of neo-hookean membranes," *ASME J. Appl. Mech*, vol. 40, pp. 9–12, 1973.

[7] W. W. Feng and P. Huang, "On the inflation of a plane nonlinear membrane," *ASME J. Appl. Mech*, vol. 41, pp. 767–771, 1974.

[8] W. Feng and W.-H. Yang, "On the contact problem of an inflated spherical nonlinear membrane," *J. Appl. Mech*, vol. 41, pp. 209–214, 1973.

[9] W. W. Feng and P. Huang, "On the general contact problem of an inflated nonlinear plane membrane," *Int. J. Solids Structures*, vol. 11, pp. 437–448, 1975.

[10] T. LA, "Compression of fluid-filled spherical shells by rigid indenters," *J. Appl. Mech*, vol. 50, pp. 717–722, 1983.

[11] Y. Lefebvre, E. Leclerc, D. Barthes-Biesel, J. Walter, and F. Edwards-Levy, "Flow of artificial microcapsules in microfluidic channels: A method for determining the elastic properties of the membrane," *Physics of Fluids*, vol. 20, pp. 123102–1–123102–9, 2008.

[12] B. Nadler, "On the contact of spherical membrane enclosing a fluid with rigid parallel planes," *Int. J. Non-linear Mech*, vol. 45, pp. 294–300, 2010.

[13] R.H.Plaut, "Linearly elastic annular and circular membranes under radial, transverse, and torsional loading. part i: large unwrinkled axisymmetric deformations," *Acta Mech*, vol. 202, pp. 79–99, 2009.

[14] V. A. Lubarda and A. Marzani, "Viscoelastic response of thin membranes with application to red blood cells," *Acta Mech*, vol. 202, pp. 1–16, 2009.

Chapter 4

Asymmetric indentation of a fluid-filled spherical membrane[1]

4.1 Introduction

Soft particles such as cells, vesicles, granules, emulsion bubbles, microcapsules and hydrogels have been widely used in the food, pharmaceutical, chromatography, electrophotography, biotechnology, biomedical and chemical industries [1–9]. Because of their broad applications, it is important to understand their mechanical properties. The deformation of these particles has paramount importance in biomedical applications, for example, the microinjection of DNA material into an embryo [3], drug delivery capsules [1,7,9] and non-toxic hydrogels for drug delivery [4]. The strength of these capsules is important for holding and releasing the encapsulated content in response to mechanical perturbations or osmotic pressure [1, 7]. Also, the blood flow in blood vessels and capillaries [10, 11] and its rheological behavior are directly related to the mechanical properties of blood cells.

Various techniques have been developed to probe the mechanical properties of soft particles. The most common techniques are: compression [5–7, 12–17], indentation [1–3, 7, 9, 18–30] and micropipette aspiration [10, 11, 31, 32]. In the

---

[1]A version of this chapter has been submitted to an international journal and is under review. Touqeer Sohail, and Ben Nadler., 2012.

compression technique, the particle is compressed between two flat parallel plates, while the deformation of the particle and the corresponding compression force are measured. Similarly, the indentation technique uses indenters of various shapes (spherical, conical and cylindrical) to indent the particle while measuring the deformation and indentation force. The compression technique gives the bulk response of the particle, while the indentation technique is used to probe the local response of the particle at different locations. In both techniques, the force versus displacement curve is obtained which gives useful information regarding the elasticity, visco-elasticty and time dependent response of the particle. Since indentation technique is non-destructive [9], it can be used to determine the response during loading and unloading cycles. In the past, this technique was used to study the indentation of axisymmetric geometries. Only recently it has been used to probe the mechanical properties of complicated geometries [19–21,33]. In the micropipette technique, a controlled suction pressure is applied to aspirate the particle into the micropipette. The measured suction pressure versus the aspiration length curve is used to obtain information about the global mechanical properties of the particle. The micropipette technique has been the preferred technique since small forces can be easily applied to detect changes in the geometry of the deformed surface of the particle during aspiration [18]. Also, micropipette aspiration is an easier experiment to perform. However, indentation is better suited to study the adhesion and spreading of particles [18].

Other experimental techniques are also mentioned in literature, including: micromanipulation, microcantilevers, Atomic Force Microscope (AFM), optical tweezers, optical trap and optical stretcher [3,7,10,11,19,20,23,31,34,35]. These methods measure the mechanical properties by deforming the particles either mechanically (contact) [3, 7, 19, 20, 23], electrically (electric field) [36, 37], chemically (by changing the external medium, ion concentrations or

pH valve) [4] or by light (laser beam) [34, 38]. AFM has been used to study the deformation of soft particles by recording the force versus indentation curves [2, 19, 20, 24, 25, 28, 39, 40]. This is a surface image technique in which a sharp tip mounted on a flexible cantilever beam is used to scan the particle surface. The deflection of the cantilever beam is measured to create the images of the surface topography of the particle. Smith *et al.* [5] used the micromanipulation technique that allows the force required to compress a single yeast cell between two parallel flat surfaces to be measured as a function of cell deformation [5]. It was found in [5] that the Young's modulus of a single yeast cell was about 100 MPa. To determine the Young's modulus of yeast cells in different surrounding environment, Bui *et al.* [20] used AFM to measure the Young's modulus of yeast cell in both Deionized (DI) water and Phosphate-buffered saline solution (PBS). The deformation of yeast in DI water was greater than in PBS solution, which indicated that yeast cell in DI water was softer than in PBS [20]. The Young's modulus observed for yeast cell was 0.15 ± 0.02 MPa in DI water and 0.24 ± 0.03 MPa in PBS. Using AFM, Arfsten *et al.* [19] found that the local deformation of single yeast cell was purely elastic and completely reversible. The influence of extracellular osmotic pressure on mechanical properties of the yeast cell was also investigated. It was observed that the stiffness increased as the turgor pressure increased [19]. Sun *et al.* [23] used force sensor to apply a uniaxial load on mouse oocyte and embryo Zona Pellucida (ZP). The experimental results demonstrated that the force required for puncturing embryo ZP (13 μN) was almost twice as much as for oocyte (7.5 μN) and the measured elastic moduli were 42.2 kPa for embryo ZP and 17.9 kPa for oocyte ZP [23]. The indentation was performed on the zebrafish embryo to generate empirical data for determining the maximum sustainable stress and strain [3]. During indentation, nine images were obtained corresponding to different force and indentation depth values [3]. These data points were used to evaluate the

maximum sustainable stress and strain starting from initial contact to the point just before penetration [3]. At an indentation depth of 440 μm, the maximum stress calculated through membrane model using the experimental data was 6.2 MPa [3]. The adhesion and viscoelastic properties of lysozyme adsorbed on Mica substrate was investigated using AFM. The Young's modulus of lysozyme was estimated to be 0.5 ± 0.2 GPa and the viscosity to be 800 ± 400 Pa-s [24]. Radmacher *et al.* [25] measured the viscoelastic properties of human platelets with AFM. The force curves taken on different spots on a platelet measured an elastic modulus in the range of $1 - 50$ kPa [25]. To characterize the properties of elastic capsules, Gordon *et al.* [7] indented an inflated polymer capsules using microcantilevers. It was observed that the indentation depth depended linearly on the force for all capsules examined. The elastic modulus of these capsules was calculated, from the linear response, to be 100 Pa. In recent years, significant improvements in the nanoindentation technique have been employed to study the mechanical properties of materials. For example, the addition of continuous stiffness measurement technique allows one to measure the dynamical contact stiffness and to probe the changes in the mechanical properties during indentation [26].

Several mathematical models have been developed to study the mechanical response of soft particles and to analyze the experimental observations. Such particles are modeled either as shells or as membranes (neglecting bending stiffness) with elastic or viscoelastic properties. The deformation and contact of a solid elastic spherical particle subjected to a point load was first studied by Hertz [41] and Boussinesq [42]. Sneddon solved the axisymmetric Boussinesq problem and developed simple formulas to express the relation between load and penetration for infinitely thick sample using different axisymmetric indenter geometries [27]. Later, the Hertz theory was extended by Johnson-Kendall-Roberts (JKR) [43] and Derjaguin-Muller-Toporov (DMT) [44] to account for

66

the adhesive contact during deformation. The Hertz theory was also modified to account for the thickness of the particles when deformed using different indenter shapes [21, 28]. More recently, numerous new models were proposed to characterize the mechanical properties of the soft particles. Wan *et al.* [1] presented an elastic model for the indentation of a spherical pressurized micro-capsule and observed that the response of the capsule is linear initially, when the bending is dominant. However, the response is cubic at large deformation, when large in-plane stretching is observed [1]. Sun *et al.* [23] used the same model for thin film encapsulated with liquid to determine the biomembrane mechanical properties of mouse oocyte and embryo ZP. Lu *et al.* [3] extended the biomembrane model [23] to determine the maximum stress and strain of zebrafish embryos. In this model, an indenter was used to exert a force on zebrafish embryo and, as a result, a conical dimple was created, where the cell contacted the indenter tip [3]. The deformed shape of the membrane was approximated by polynomial function [3]. Bui *et al.* [20] fitted the experimental force versus indentation curves of yeast cells with the Hertz-Sneddon model with a power equation of the form $F = a\,\Delta z^b$, where a represented the Young's modulus and b depended on the indenter tip shape [39]. They suggested that $b \approx 2$ for conical indenter, $b \approx 1.5$ for parabolic indenter and $b \approx 1$ for cylindrical indenter. Arfsten *et al.* [19] observed that the local deformation of a yeast cell was purely elastic and, therefore, modeled the cell as a linear spring with spring constant (k_c), and found a proportional relation between k_c and the turgor pressure. Radmacher *et al.* [25] described the elastic response of human platelets using the Hertz model, where the contact area is a function of the loading force. The measured indentation versus loading force of Filopodium shows good agreement with the Hertz model only for small indentation. However, for Pseudonucleus, which is the thicker part of the cell, it shows good agreement for large indentation [25]. Gordon *et al.* [7] used a Finite Element

Method (FEM) model to describe the indentation of a self-assembled polymer membrane capsule inflated by osmotic pressure from internal polyelectrolyte. It was shown that a membrane model (negligible bending stiffness) provided more accurate predications than a shell model (with bending stiffness). The FEM model was fitted with the indentation experiments to determine the system parameters. It was found that $Et = 0.73$ N/m and $pR/2Et = 0.023$, where E is the Young's modulus, t is the thickness, p is the internal pressure, and R is the radius of the capsule. Vella et $al.$ [9] investigated the response of uniformly pressurized spherical capsule by modeling it as a shell under a point load. It was observed that the response has two linear regimes, at small and large indentations.

Various assumptions have been considered to minimize the difficulty in modeling the mechanical response of such particles. The most common of these assumptions include homogeneity, constant surface area, constant volume, constant pressure, constant thickness, axisymmetric deformation, small deformation and negligible bending stiffness [1, 2, 7, 9, 10, 12–17, 21, 23, 25, 28–32, 36]. These assumptions greatly simplified the analysis of soft particles, but are associated with limitations. For example, Leukocyte showed similar behavior when aspirated at different locations by rotating the cell [10], which suggested that Leukocyte cells had homogenous properties. The axisymmetric recovery of Leukocyte cells provided further evidence of homogeneity [11]. However, it was also observed that the cell was morphologically heterogeneous [10, 31]. It has been observed by many researchers that bending stiffness dominated the small deformation response but could be neglected for large deformation [1]. Similarly, for thin-fluid shells and small indenter size, the bending stiffness becomes negligible [12–14]. However, it is necessary to consider the bending, if the thickness to radius ratio is significant ($R/t \leq 10$). Taber [12, 29] compared the experimental measures of water-filled rubber shells of various thicknesses

68

with the model thin shell and showed that bending dominated for deflection less than 20 percent of the radius. At large deflection, the membrane in-plane stress became more significant since the fluid pressure increased. Joshi *et al.* [36] used a thin elastic shell model to determine the deformation of a spherical cell structure in response to an external force field. He observed that the bending moment was small and could be neglected. Liu *et al.* [13] suggested that the bending moment could be neglected for a spherical micro-capsule that has a radius 16 times more than its thickness. However, Rachik *et al.* [14] indicated that the thin shell approximation for capsules was valid only for thickness to radius ratio of up to 5% and the bending effect could not be ignored for thick shells. Considering small strain, the linear theory was often assumed [10, 31], but it has been found that the response was nonlinear for large deformation [1, 9, 20, 21, 23, 39, 45].

The Hertz-Sneddon contact model has also been used to study the response of soft particles [2, 21, 23, 28, 46]. This model treats the particle as as solid body. However, it is experimentally observed that many of these soft particles do not behave as a solid body upon indentation. This model only shows good agreement with experimental data for indentation smaller than the particle thickness [21]. This model also assumes that there is only local deformation in the neighbourhood of the contact with the indenter, while the global shape remains unchanged, which is not always observed in experiments [2, 7, 20, 23]. Due to these assumptions, this model lacks the ability to accurately describe the large deformation of soft particles.

In this chapter, we develop a continuum model to characterize the behavior of a spherical particle during indentation by a rigid conical indenter. Unlike previous studies [1, 10, 31], we do not assume small deformations. Hence the model has the ability to capture the nonlinear response observed experimentally. We only study axisymmetric deformations, but do not impose any addi-

tional geometrical assumption on the deformation to obtained the equilibrium configurations of the particle as a function of the indenter force. The particle is modeled as a spherical membrane enclosing incompressible fluid. The membrane is considered to be hyperelastic, homogenous and isotropic, while the viscosity of the membrane and the enclosed fluid, the frictional contact and adhesion were neglected. Consistent with the membrane assumption, bending stiffness is neglected, but the membrane can undergo large deformations. The current study determines the indenter force, indenter displacement, fluid pressure, contact radii and principal stress distributions in the membrane. As part of the formulation, it is necessary to specify the constitutive relation. In the literature, constitutive relations based on the theory of elasticity or viscoelasticty are generally used [47]. However, due to the complex microstructure of these particles, the exact constitutive relations are difficult to determine. Therefore, we formulate the problem for general nonlinear isotropic hyperelastic material by using a neo-Hookean material type as an example.

The remainder of the chapter is organized as follows. The governing equations of the deformations, equilibrium equations, the constitutive relation and the contact conditions during indentation are presented in Section 4.2. The numerical procedure is explained in Section 4.3. The results and discussion are presented in Section 4.4, and conclusions are given in Section 4.5.

4.2 Formulation

Consider a nonlinear membrane Ω, which is spherical and stress-free in its reference configuration κ as depicted in Figure 4.1(a). In the reference configuration, the membrane occupies a sphere surface of radius R. The membrane is inflated from its stress-free radius, R, to radius $r_0 > R$ and then quasistatically indented by a rigid conical indenter, while supported by a rigid plane.
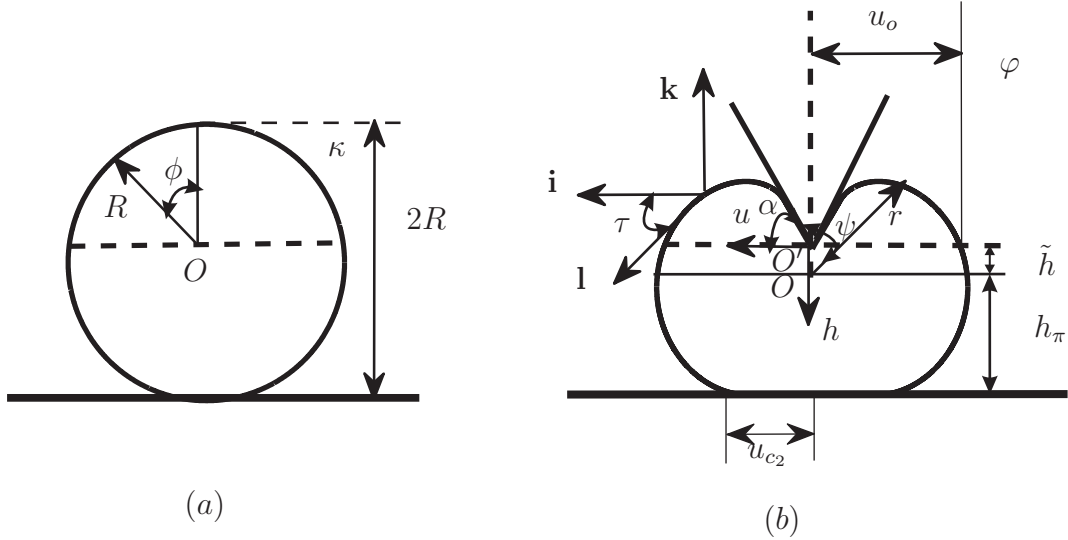
Figure 4.1: (a) Referential configuration, (b) Deformed equilibrium configurations of the membrane-fluid structure in contact with rigid conical indenter and flat support.

This indentation yields an axisymmetric deformation in the deformed configuration φ as shown in Figure 4.1(b). To study the mechanical response of this membrane-fluid structure, the equilibrium configurations is obtained. The formulation of the governing equation is presented below.

4.2.1 Governing ODEs and boundary conditions

The basic idea for formulating the deformation of the membrane has been illustrated in Chapter 2, using the radial position $r(\phi)$ and meridian angle $\psi(\phi)$ (see Figure 4.1). The choice of origin, O, is natural in the reference configuration, but this is not the case for the deformed configuration (see Figure 4.1), where the origin can be located anywhere on the axisymmetry axis. Since the deformed configuration is axisymmetric, it is more natural to use cylindrical coordinates rather than spherical coordinates. We now reformulate the deformation using the more convenient cylindrical coordinates $\{u, h, \theta\}$ with respect to the origin located at the conical indenter tip, O', as shown in Figure 4.1(b). The coordinates $u(\phi)$ and $h(\phi)$ are the horizontal and vertical

distances from the origin O', such that

$$\mathbf{x}(\phi, \theta) = u(\phi)\mathbf{i}(\theta) + h(\phi)\mathbf{k}. \tag{4.1}$$

The following relationships can be easily established

$$u = r \sin \psi, \quad h = \tilde{h} - r \cos \psi, \tag{4.2}$$

where $\tilde{h}$ is the distance between the origin O' and the horizontal line passing through O at $\tau = \pi/2$. Differentiating (4.2) and using equation (2.22), the first order ODE for $u'(\phi)$ and $h'(\phi)$ are

$$u' = \lambda R \cos \tau, \quad h' = \lambda R \sin \tau. \tag{4.3}$$

The principal hoop stretch $\mu(\phi)$ in $(2.17)_2$ can be expressed in terms of $u(\phi)$ as

$$\mu = \frac{u}{R \sin \phi}. \tag{4.4}$$

Assuming that the rigid conical indenter and the flat support are frictionless, the equilibrium equations for the membrane can be derived following the same procedure as demonstrated in Chapter 3, which results in the following two ODEs for principal stretch $\lambda(\phi)$

$$\lambda' = \frac{(w_\mu - \lambda w_{\lambda\mu}) \cos \tau - (w_\lambda - \mu w_{\lambda\mu}) \cos \phi}{w_{\lambda\lambda} \sin \phi}, \tag{4.5}$$

and for angle $\tau(\phi)$ (see Figure 4.1(b))

$$\tau' = \frac{\lambda \mu R(p_f - p_c)}{w_\lambda} - \frac{w_\mu \sin \tau}{w_\lambda \sin \phi}. \tag{4.6}$$

where p_f and p_c are the pressure due to the fluid and due to the indenter,

72

respectively. The resultant external force applied on the membrane by the conical indenter is

$$f_c = \int_{\Omega_{c_1}} p_{c_1} \cos \tau dA, \tag{4.7}$$

where Ω_{c_1} is the part of the membrane in contact with rigid conical indenter and p_{c_1} is the indenter pressure on the membrane. At the contact part of the membrane with flat support Ω_{c_2}, where $\tau = \pi$, the contact pressure between the membrane and the flat support is equal to the fluid pressure inside the membrane, which is confirmed by (4.6). So, the resultant external force applied on the membrane by the flat support is

$$f_s = \pi u_{c_2}^2 p_{c_2}, \tag{4.8}$$

where $u_{c_2} = u(\phi_{c_2})$ (see Figure 4.1(b)) is the radius of the contact area with flat indenter and p_{c_2} is the pressure exerted on the membrane by the flat support. The global equilibrium of the membrane requires that the sum of the external forces vanishes, that is

$$f_c = f_s. \tag{4.9}$$

Define ϕ_{c_1} to be the convected coordinate of the interface between the part of the membrane in contact with the indenter and the part not in contact, and ϕ_{c_2} to be the convected coordinate of the interface between the part of the membrane not in contact and the part in contact with the flat support. Then, the part Ω_{c_1} is parametrized by $0 \leqslant \phi \leqslant \phi_{c_1}$ and $\phi_{c_2} \leqslant \phi \leqslant \pi$ corresponds to the part Ω_{c_2} in contact with the flat indenter. Ω_{n_c} will be used to denote the domain not in contact, corresponding to $\phi_{c_1} \leqslant \phi \leqslant \phi_{c_2}$ The equilibrium of each domain is governed by a different set of equations.

73

4.2.1.1 Equilibrium of Ω_{c_1}

The membrane is in contact with the rigid conical indenter on the domain $0 \leqslant \phi \leqslant \phi_{c_1}$. The indenter makes a constant angle α with the horizontal axis as shown in Figure 4.1(b). Since the membrane is in contact with the indenter on Ω_{c_1}, $\tau = -\alpha$ and

$$\tau' = 0. \tag{4.10}$$

Employing (4.6), the contact pressure between the membrane and the conical indenter, p_{c_1} is evaluated by

$$p_{c_1} = p_f - \frac{w_\mu \sin \tau}{\lambda \mu R \sin \phi}. \tag{4.11}$$

The three first order ODEs $(4.3)_1$, $(4.3)_2$ and (4.5) are to be integrated on this domain with the initial conditions

$$u = 0, \quad h = 0 \quad \text{at} \quad \phi = 0. \tag{4.12}$$

4.2.1.2 Equilibrium of $\Omega_{c_{nc}}$

The domain of the membrane which is neither in contact with the conical indenter nor with the flat support is parametrized by $\phi_{c_1} < \phi < \phi_{c_2}$. Since the contact pressure vanishes, $p_c = 0$, in this part equation (4.6) reduces to

$$\tau' = \frac{\lambda \mu R p_f}{w_\lambda} - \frac{w_\mu \sin \tau}{w_\lambda \sin \phi}. \tag{4.13}$$

Moreover, the angle τ monotonically increases from $-\alpha$ to π as depcited in Figure 4.1(b). The four first order ODEs $(4.3)_1$, $(4.3)_2$, (4.5) and (4.13) are integrated to solve for the deformation of the membrane in the non-contact domain. The four boundary conditions at the interface ϕ_{c_1} are the continuity of λ (i.e., $\lim_{\phi \to \phi_{c_1}^+} \lambda = \lim_{\phi \to \phi_{c_1}^-} \lambda$), τ (i.e., $\lim_{\phi \to \phi_{c_1}^+} \tau = \lim_{\phi \to \phi_{c_1}^-} \tau$), u

74

(i.e., $\lim_{\phi \to \phi_{c_1}^+} u = \lim_{\phi \to \phi_{c_1}^-} u$) and h (i.e., $\lim_{\phi \to \phi_{c_1}^+} h = \lim_{\phi \to \phi_{c_1}^-} h$) across the interface. The fifth boundary condition is at the interface ϕ_{c_2}, given by

$$\tau = \pi \quad \text{at} \quad \phi = \phi_{c_2}. \tag{4.14}$$

4.2.1.3 Equilibrium of Ω_{c_2}

In this part, $\phi_{c_2} \leqslant \phi \leqslant \pi$, the membrane is in contact with the flat support and $\tau = \pi$. Therefore $h' = 0$ and $\tau' = 0$. Equation (4.6) reduces to

$$\frac{\lambda \mu R (p_f - p_{c_2})}{w_\lambda} = 0. \tag{4.15}$$

Hence, the contact pressure between the membrane and the flat support is

$$p_{c_2} = p_f, \tag{4.16}$$

as suggested by (4.15). The two governing equations of this domain are $(4.3)_1$ and (4.5) with the continuity conditions of λ (i.e., $\lim_{\phi \to \phi_{c_2}^+} \lambda = \lim_{\phi \to \phi_{c_2}^-} \lambda$) and u (i.e., $\lim_{\phi \to \phi_{c_1}^+} u = \lim_{\phi \to \phi_{c_1}^-} u$) across the interface at ϕ_{c_2}, and the boundary condition

$$u = 0 \quad \text{at} \quad \phi = \pi. \tag{4.17}$$

4.2.2 Constitutive relationships

The neo-Hookean strain energy function is adopted to describe the membrane

$$w(\lambda, \mu) = \frac{G}{2} \left(\lambda^2 + \mu^2 + (\lambda \mu)^{-2} - 3 \right), \tag{4.18}$$

where G is the ground state shear modulus constant. For the homogeneous deformation of a spherical membrane of radius R to spherical membrane of radius r_0 (mapping of a sphere into a sphere), the initial principle stretches

75

are $\lambda_i = \mu_i = \frac{r_0}{R}$, the enclosed fluid volume is $V_0 = \frac{4}{3}\pi r_0^3$, and the enclosed fluid pressure is

$$p_f^0 = \frac{2G}{r_0}\left(1 - \left(\frac{R}{r_0}\right)^6\right). \tag{4.19}$$

Since the fluid is assumed to be incompressible, the fluid pressure, p_f, is a Lagrange multiplier determined by the incompressibility condition

$$J_f = \frac{V}{V_0} = 1, \tag{4.20}$$

where the deformed volume V is evaluated by

$$V = 2\pi \int_0^{u_0} hudu + \pi \int_0^{h_\pi} u^2 dh, \tag{4.21}$$

where u_0 and h_π are shown in Figure 4.1(b). The first term in (4.21) accounts for the enclosed volume above the plane defined by $h = 0$, while the second term accounts for the enclosed volume below this plane.

4.3   Numerical Algorithm

The shooting method with standard Euler explicit integration are employed to integrate the governing ODEs in the three parts. The membrane domain, $0 \leqslant \phi \leqslant \pi$, is discretized into n elements of equal length $\Delta\phi$. Due to the discretization of the membrane (required by the numerical solution), it is numerically preferred to control the parameter ϕ_{c_1} such that it coincides with the membrane discretization. A series of equilibrium configurations is computed for increasing values of ϕ_{c_1} which is associated with an increase in the indenter displacement. The parameter ϕ_{c_1} is increased by adding elements to the domain of the membrane in contact with the conical indenter, Ω_{c_1}. As ϕ_{c_1} is monotonically increased, the part of the membrane in contact with the flat support, represented by ϕ_{c_2}, also increases. For each additional element that

76

comes into contact with the conical indenter, the deformed equilibrium config-uration is solved. It should be noted that, while the interface ϕ_{c_1} is prescribed, the interface ϕ_{c_2} is unknown.

Here, the shooting method is used to convert the BVP into two initial value problems: one involving integration from $\phi = 0$ to $\phi = \phi_{c_2}$ and the other involving backward integration from $\phi = \pi$ to $\phi = \phi_{c_2}$. The decomposition into two initial value problems is done to reduce the cumulative error associated with the integration. For the deformed membrane, the guessed values $\lambda_1 = \lambda(\phi = 0)$, $\lambda_2 = \lambda(\phi = \pi)$, p_f and ϕ_{c_2} are used to satisfy the boundary condition $\tau(\phi = \phi_{c_2}) = \pi$, continuity of u and λ at ϕ_{c2}, and one additional condition (4.20). The Newton-Raphson method is used to solve the resulting system of nonlinear algebraic equations. After $\{\lambda, \tau, u, h\}$ are obtained, the other principal stretch μ can be determined from (4.4) and the principal stresses can be calculated from (2.27).

4.4   Results and Discussion

The numerical results are presented in this section to study the response of the fluid-filled membrane when indented by rigid conical and flat indenters. At each equilibrium configuration, the conical indenter force, the enclosed fluid pressure, the contact areas, the principal stresses and stretches in the mem-brane are studied in detail and discussed. The following normalized parameters are used

$$\bar{r}_0 = \frac{r_0}{R}, \quad \bar{h} = \frac{h}{2r_0}, \quad \bar{u} = \frac{u}{r_0}. \tag{4.22}$$

The conical indenter force f_c, the indenter height d, the enclosed fluid pressure p_f, and the contact radii are normalized as

$$\bar{f}_c = \frac{f_c R}{G r_0}, \quad \bar{d} = \bar{h}(\phi = 0), \quad \bar{p}_f = \frac{p_f R}{G}, \quad \bar{u}_{c_1} = \frac{u_{c_1}}{r_0}, \quad \bar{u}_{c_2} = \frac{u_{c_2}}{r_0}, \tag{4.23}$$

where u_{c_1} is the contact radius with the conical indenter and u_{c_2} is the contact radius with the flat support.

In many experiments, spherical beads are used at the AFM tip [21, 28] to probe the elastic properties of the particle. This provides the average elastic response of the particle associated with the diameter of the spherical bead, but local properties cannot be obtained [21]. Therefore, sharp AFM tips are used to provide measurements of local elastic properties with nanometer resolution [21]. Experiments using spherical AFM tip to determine the mechanical response of thin Gelatin film [46] showed that the Hertz model failed to correctly predict the elastic property when the indentation is larger than the radius of curvature of the tip. However, the Hertz cone model predicted correctly the elastic response for large indentation [46]. For small indentations, the response is better approximated by spherical indenter tip [46], but for large indentation, the tip geometry should be assumed either conical or pyramidal [2, 21, 46].

The inflated spherical configuration and the deformed equilibrium configurations by various conical indenters ($\alpha = 0^o, 20^o, 40^o, 60^o$ and 80°) at indenter height of $\bar{d} = 0.50$ are depicted in Figure 4.2. It should be noted that the positive direction of h is pointing downward in Figure 4.1(b). In Figure 4.2, we have converted the positive direction of h upward by using negative of the h values obtained from solving the BVP. In addition, a rigid body translation in the vertical direction is introduced so that, in the contact zone with the flat support, h is zero. It can be observed that, as the indentation advances, the membrane is pushed outward circumferentially to preserve the fluid volume. Since the membrane structure has vanishing bending stiffness, the membrane takes a conical shape at the part in contact with the conical indenter and a flat shape at the part in contact with the flat support. This was also seen experimentally when mouse embryo, mouse oocyte, and zebrafish embryo are

deformed by rigid indenters [3, 23]. Since the membrane is hyperelastic, it can undergo large deformation and can recover fully [7]. It has also been observed that, as the sharpness of the conical indenter increases (i.e., α increases), the part of the membrane in contact with the conical indenter, Ω_{c_1}, and in contact with the flat support, Ω_{c_2}, decreases. By decreasing the conical indenter sharpness (i.e., decreasing α), the membrane circumferential advancement increases as shown in Figure 4.2.
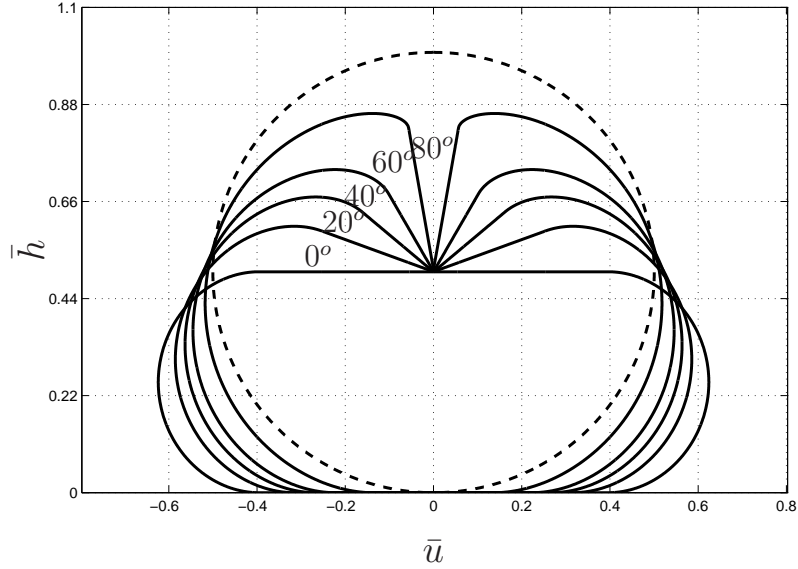
Figure 4.2: Equilibrium configurations of the membrane-fluid structure at various indenter angles $\alpha = \{0^o, 20^o, 40^o, 60^o, 80^o\}$ for $\bar{r}_0 = 2$ and $\bar{d} = 0.50$.

The resultant contact force of the conical indenter, which is equal to the resultant contact force with the flat support, is plotted in Figure 4.3. It has been observed that the response depends on the indenter shape and also exhibits different behaviors for small and large deformation [9]. The response is linear for small deformation [1, 9, 14, 15] and nonlinear for large deformation [1, 5, 9, 13–15, 20, 21, 23, 39, 45]. Starting from the initial point of contact with $\bar{d} = 1.0$ (no deformation), the membrane shows linear response until the indenter height reaches $\bar{d} = 0.98$ for flat indenter and $\bar{d} = \{0.96, 0.93, 0.78, 0.65\}$ for conical indenters with sharpness $\alpha = \{20^o, 40^o, 60^o, 80^o\}$. It becomes clear that the linear regime increases as the indenter sharpness increases. The reason

is that, by increasing the indenter sharpness, the deformation is localized as shown in Figure 4.2. When the indenter sharpness decreases, the deformation is non-localized, which increases the geometrical nonlinearity. In Figure 4.3, the different curves of the indenter force represent the stiffness of the structure corresponding to different indenters. It can be seen that the contact force in-
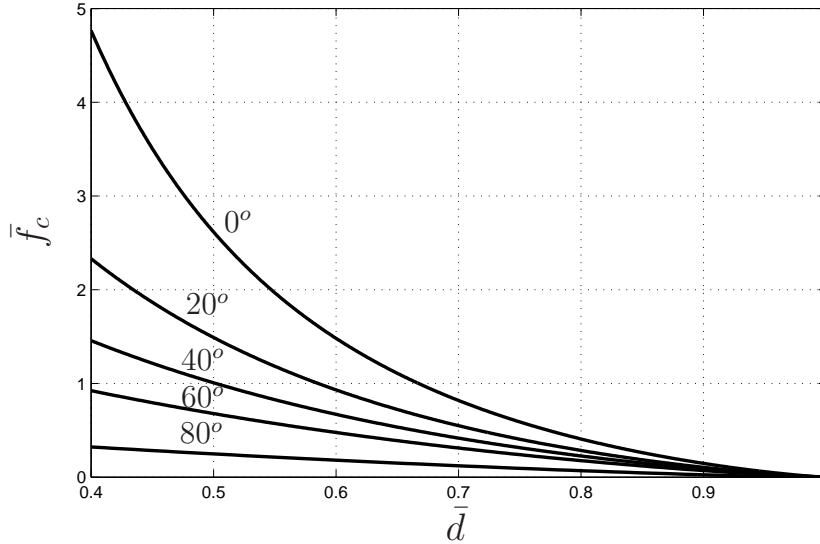
Figure 4.3: Normalized conical indenter force vs. normalized conical indenter height for various conical indenters $\alpha = \{0^o, 20^o, 40^o, 60^o, 80^o\}$ and $\bar{r}_0 = 2$.

creases nonlinearly with indentation displacement, which is in agreement with experimental results [13–15, 20, 21, 23, 45]. In particular, at indenter height of $\bar{d} = 0.4$ and $\bar{r}_0 = 2.0$, the force applied by the flat indenter is $\bar{f}_c = 4.74$. At the same indenter height, the indentation force for conical indenters with sharpness $\alpha = \{20^o, 40^o, 60^o, 80^o\}$ are $\{48.94\%, 30.71\%, 19.36\%, 6.77\%\}$ of the flat indenter. As expected, this shows that, by increasing the sharpness of the conical indenter, the force required to deform the membrane decreases to a great extent. Santos *et al.* [21] observed that the applied force for a conical indenter is smaller compared to a spherical indenter. Similarly, when the capsules are deformed with point and flat indenters, it is observed that, at the same indentation depth, smaller force is required by the point indenter than by the flat indenter. In our model, if we increase the sharpness from 0^0 to 90^0,

the indenter geometry changes from flat to conical and, ultimately, to point load; the force required to deform the membrane decreases with increasing sharpness, which is consistent with [7, 21].
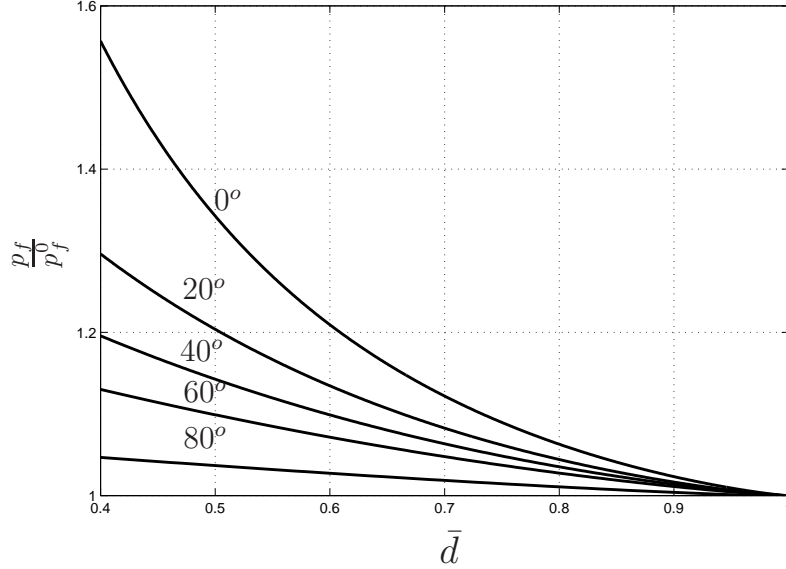
Figure 4.4: Normalized fluid pressure vs. normalized conical indenter height for various conical indenters $\alpha = \{0^o, 20^o, 40^o, 60^o, 80^o\}$ and $\bar{r}_0 = 2$.

The indentation experiments are also used to determine the enclosed fluid pressure [9, 40]. A major resistance to indentation is provided by the enclosed fluid [9], while the role of the peripheral membrane is to confine the fluid. Gordon *et al.* [7] modeled the polymer capsules inflated by osmotic pressure from internal polyelectrolyte as a pressurized membrane and used the finite element modeling approach to study the deformation upon indentation. Because these capsules are inflated to a great extent as shown in Figure 6 of [7], the inflation can be used as a possible non-mechanical trigger for the release of the encapsulated contents. Similarly, due to the osmotic gradient, the water flows into the cell under physiological condition, causing an overpressure inside the cell, which is called turgor pressure and is defined as the difference between intracellular and extracellular osmotic pressure [19]. Since these examples are associated with large inflations, in particular for capsules [7], we take the initial inflation to be $\bar{r}_0 = 2.0$. The fluid pressure as a function of indenter height

81

is depicted in Figure 4.4. The fluid pressure increases monotonically with the decrease in indenter height. Moreover, in [7] it was shown that at the same indentation depth, less force is required for point indenter than for flat indenter. A similar relationship is observed in our model since compared with conical indenter, the fluid pressure increases at higher rate when using flat indenter as depicted in Figure 4.4. For comparison, for flat indenter ($\alpha = 0^o$), the fluid pressure at the indenter height of $\bar{d} = 0.4$ and $\bar{r}_0 = 2.0$ is $\bar{p}_f = 1.56$. For conical indenters with sharpness $\alpha = \{20^o, 40^o, 60^o, 80^o\}$, at the same indenter height, the fluid pressure is $\{83.27\%, 76.91\%, 72.60\%, 67.33\%\}$ of the flat indenter. The fluid pressure decreases as the conical indenter sharpness increases, because the deformation is more localized for sharper indenters.
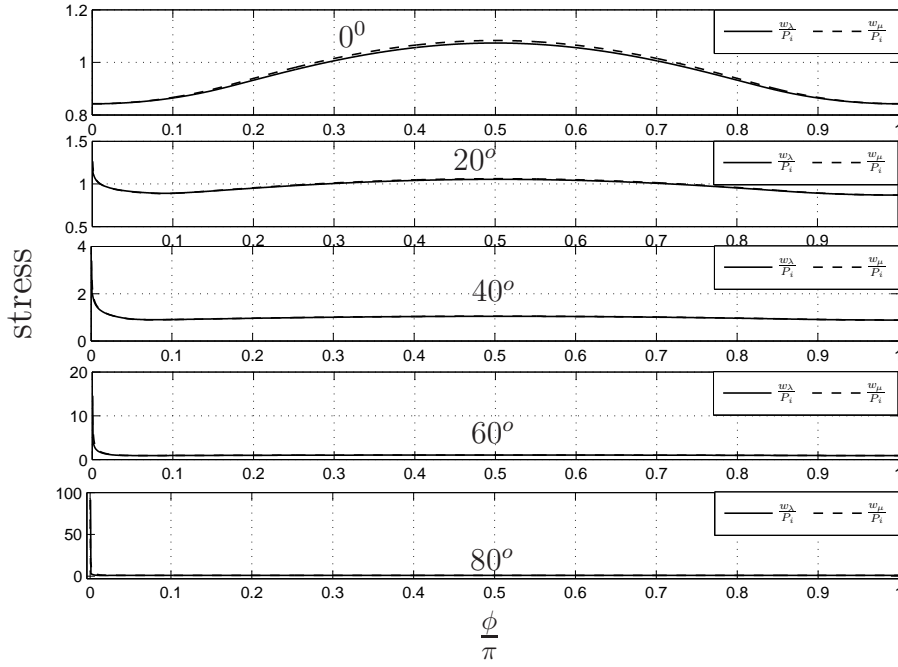
Figure 4.5: Distribution of normalized principal stresses in the membrane at $\bar{d} = 0.50$ for various conical indenters $\alpha = \{0^o, 20^o, 40^o, 60^o, 80^o\}$ and $\bar{r}_0 = 2$.

The principal stress distribution in the membrane, normalized by the initial membrane stress P_i, at the indenter height of $\bar{d} = 0.50$, is depicted in Figure 4.5. With initial inflation of $\bar{r}_0 = 2.0$, it is observed that both principal Piola-Kirchhoff stresses w_λ and w_μ are approximately equal everywhere in the
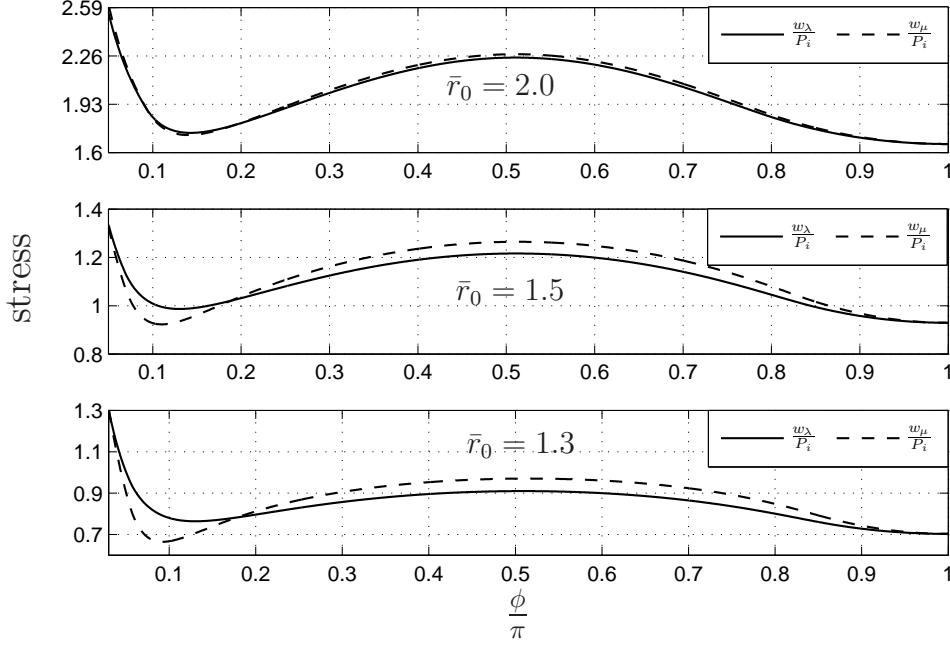
Figure 4.6: Distribution of normalized principal stresses in the membrane at $\bar{d} = 0.50$ for different initial inflations $\bar{r}_0 = \{2.0, 1.5, 1.3\}$ and conical indenter $\alpha = 60^0$.

membrane. When flat indenter ($\alpha = 0^o$) is used, the maximum principal stress occurs at the equator ($\phi = \psi = \pi/2$) [13, 17, 45, 48, 49], since this part is not externally supported. However, for conical indenters, the maximum stress is located at the point in contact with the indenter tip [3, 21]. For comparison, at $\bar{d} = 0.50$ the normalized maximum stress is 1.083 at $\phi/\pi = 0.5$ for flat indenter and the normalized maximum stresses are $\{1.263, 3.385, 14.48, 91.14\}$ at $\phi/\pi = 0$ for different sharp conical indenters $\alpha = \{20^o, 40^o, 60^o, 80^o\}$. It is obvious that the maximum stress value for conical sharp indenters is much larger than for the flat indenter which is also reported in [21], where the stress for conical indenter is almost ten times larger than that for spherical indenter. As sharpness increases, the maximum stress significantly increases and becomes more localized about the indenter tip, while the stress away from the indenter tip is almost uniform, which is in agreement with [3]. In Figure 4.5, for indenters $\alpha = \{0^o, 20^o\}$, the principal stresses show non-monotonic

83

change away from the indenter tip. To better observe this non-monotonic change for $\alpha = 60^o$, which is difficult to observe in Figure 4.5, the principal stresses are also depicted in Figure 4.6 for different initial inflations $\bar{r}_0 = \{2.0, 1.5, 1.3\}$. The non-monotonic change is significant for both principal stresses w_λ and w_μ. For large initial inflation $\bar{r}_0 = 2.0$, the principal stresses are equal but as the initial inflation decreases, the principal stresses start to vary as shown in Figure 4.6. At an initial inflation of $\bar{r}_0 = 1.5$, the Piola-Kirchhoff stress w_μ is smaller than w_λ at the part in contact with the conical indenter, $0.0 \leqslant \phi \leqslant 0.17$. However, w_μ is larger than w_λ at the part which is not in contact, $0.17 < \phi \leqslant 0.9$. For the part of the membrane in contact with the flat support, $0.9 < \phi \leqslant 1.0$, the principal stresses are almost equal. Similar behavior is observed for an initial inflation of $\bar{r}_0 = 1.3$. The variation in the principal stresses is dependent on the initial inflation, which is an important factor to study in inflated particles such as cells, vesicles, and polymer capsules [1, 7, 9, 19, 40].

Figure 4.7 shows the principal stretches distributions in the membrane for various initial inflations $\bar{r}_0 = \{2.0, 1.5, 1.3\}$ using flat indenter. Similarly, Figure 4.8 shows the principal stretches distributions in the membrane for different initial inflations using conical indenter with $\alpha = 60^o$. In Figure 4.7 and Figure 4.8, the principal stretches are normalized by the initial stretches. The principal stretches show similar behavior to the principal stresses in Figure 4.5 and Figure 4.6. For large initial inflation, the membrane is close to an equibiaxial stretch state, but, for smaller initial inflations, the principal stretches deviate. In case of flat indenters (Figure 4.7), the hoop stretch, μ, is always greater than the meridian stretch, λ. However, when conical indenters are used, the hoop stretch μ is smaller than the meridian stretch λ at the part of membrane in contact with the conical indenter, while being larger than the meridian stretch on the part of the membrane not in contact.
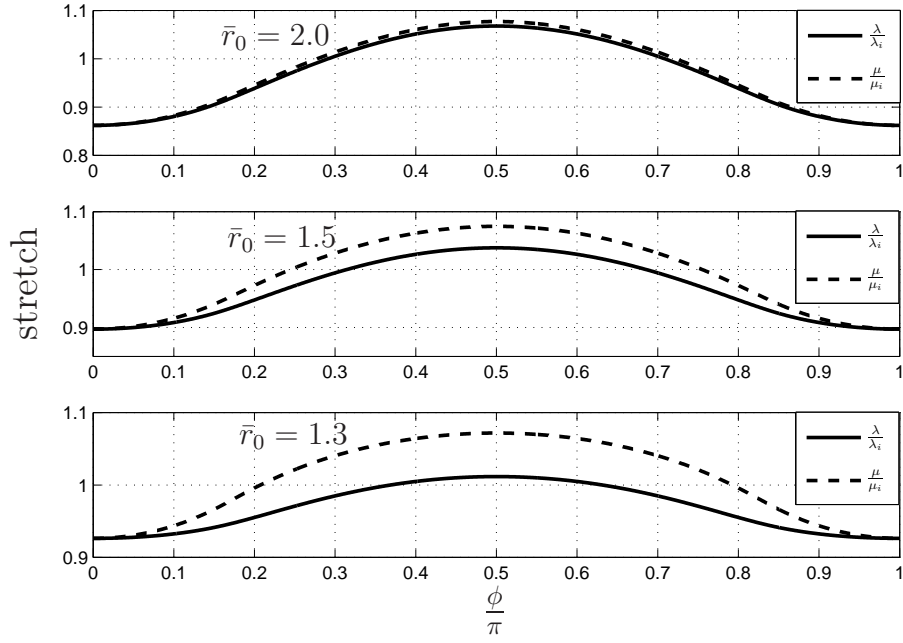
Figure 4.7: Normalized principal stretches in the membrane at $\bar{d} = 0.50$ for different initial inflations $\bar{r}_0 = \{2.0, 1.5, 1.3\}$ and flat indenter $\alpha = 0^0$.
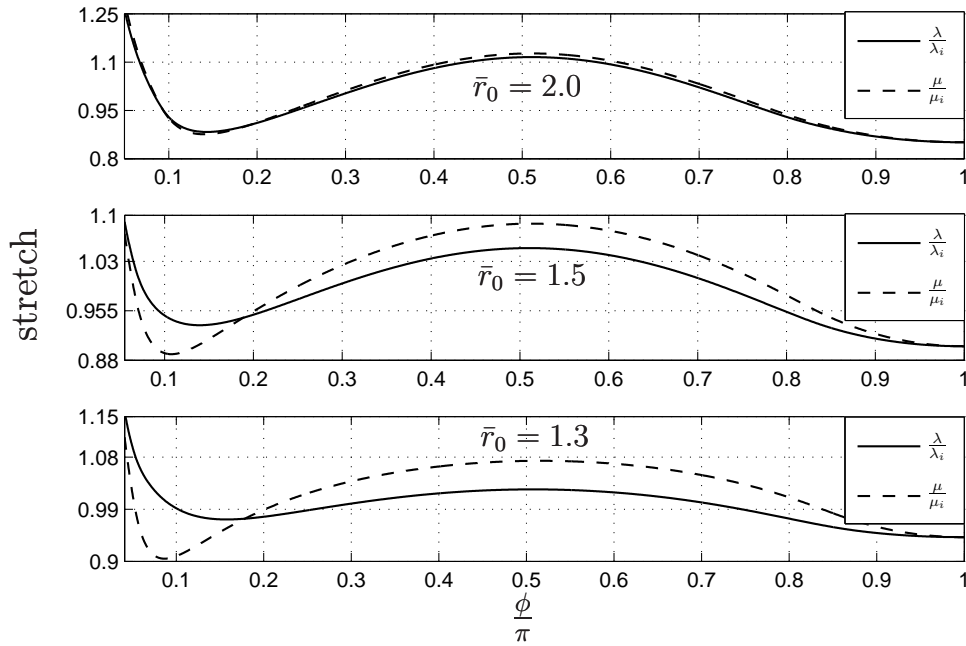
Figure 4.8: Normalized principal stretches in the membrane at $\bar{d} = 0.50$ for different initial inflations $\bar{r}_0 = \{2.0, 1.5, 1.3\}$ and conical indenter $\alpha = 60^o$.

The pole stress, which is the maximum stress for conical indenters, can be used as an indication of the penetration conditions [3]. The principal stress at the pole normalized by the initial homogeneous stress P_i as a function of indenter height for various indenters is shown in Figure 4.9. It is observed, as expected, that the pole stress in the membrane has strong dependency on the indenter sharpness. Moreover, while for sharp indenters, $\alpha > 20^o$, the pole stress increases monotonically with indenter displacement (i.e., decrease in indenter height), for blunt indenters, $\alpha < 20^o$, the pole stress decreases initially followed by an increase. This behavior is governed by the coupling between the pole strain and the fluid pressure (see [17]). It was also observed in [30] that when the structure is poked by two conical indenters, the pole stress during the indentation process increases initially, then remains approximately constant and, in the final stage of indentation decreases. However, if the membrane is poked by a conical indenter on a flat support, the response is completely different (see Figure 4.9).

The final equilibrium configurations of the fluid-membrane structure as the conical indenter comes into contact with the flat support, $\bar{h} = 0$, are depicted in Figure 4.10. For flat indenter, $\alpha = 0^o$, the indenter height can approach zero, but cannot take the value zero, since the inclosed fluid volume cannot vanish. Such large deformed equilibrium configuration of the membrane is possible for polymer capsules that recover elastically even when indented by a depth of nearly the capsule's diameter [7]. The contact radius increases with indenter displacement until the indenter tip comes into contact with the flat support. The dependency of the contact radii, u_{c_1} and u_{c_2} on the indenter height are shown in Figure 4.11. An increase in the sharpness of the conical indenter (i.e., increasing α) yields a decrease in the contact radii. It is observed that the contact radius of the structure with the flat support is larger than the contact radius with the conical indenter, and converges to the same value
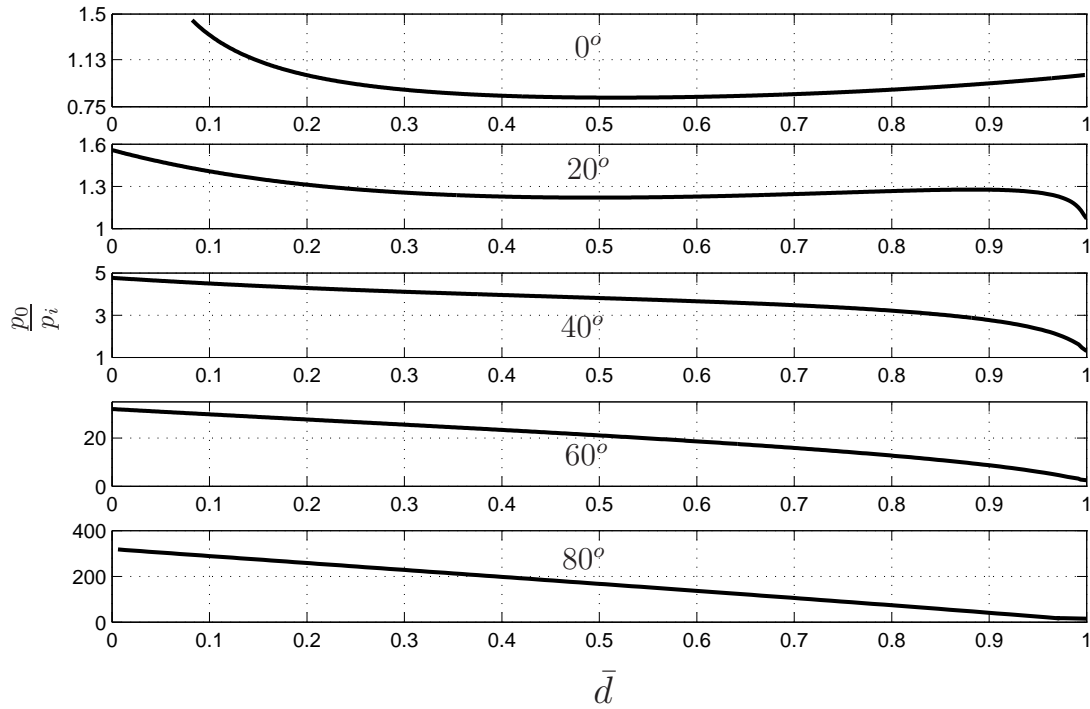
Figure 4.9: Normalized principal stress at the pole vs. normalized indenter height for various indenters $\alpha = \{0^o, 20^o, 40^o, 60^o, 80^o\}$ and $\bar{r}_0 = 2$.
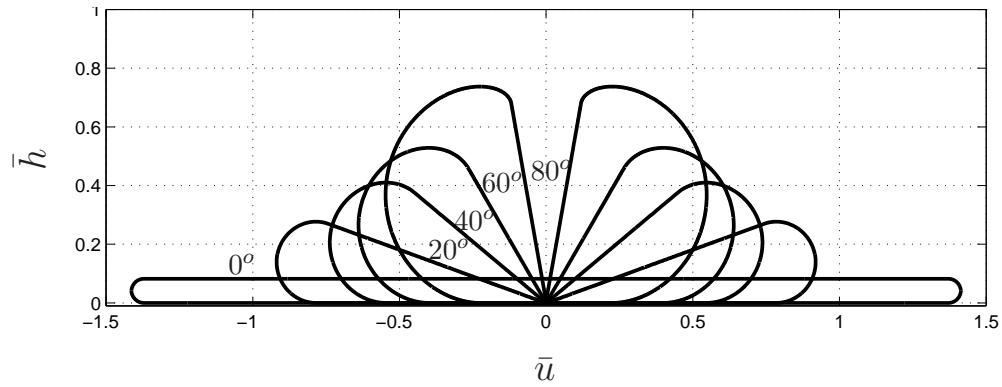
Figure 4.10: Equilibrium configurations at indenter height approaching zero for various conical indenters $\alpha = \{0^o, 20^o, 40^o, 60^o, 80^o\}$ and $\bar{r}_0 = 2$ and $\bar{d} = 0$.

with a decrease of indenter sharpness. The same was observed experimentally in [12].
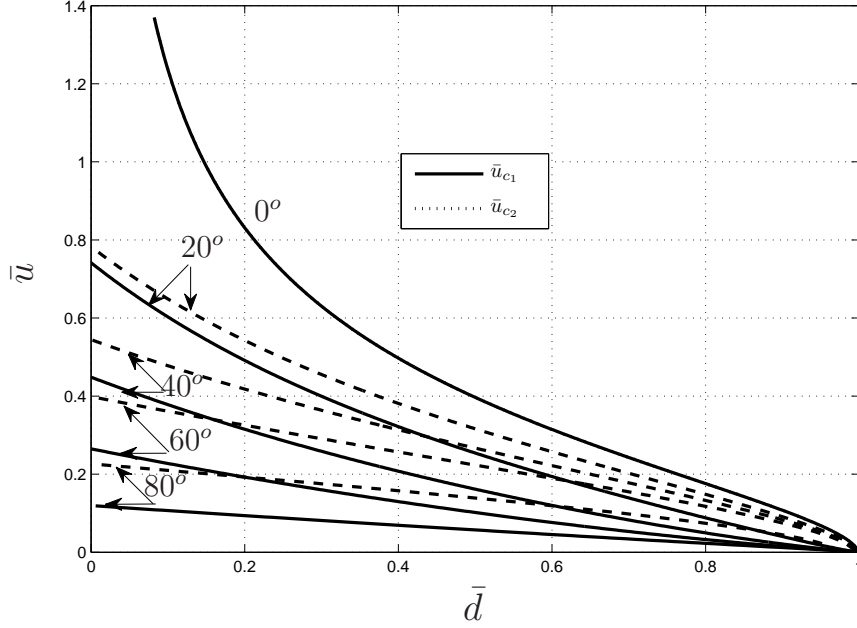
Figure 4.11: Normalized contact radii vs. normalized conical indenter height for various conical indenters $\alpha = \{0^o, 20^o, 40^o, 60^o, 80^o\}$ and $\bar{r}_0 = 2$.

4.5   Conclusions

In this chapter, we developed a nonlinear spherical membrane-fluid model. The membrane is assumed to be homogenous, isotropic and of hyperelastic type filled with incompressible fluid. The governing equations are formulated to investigate the mechanical response of the structure in contact with a rigid conical indenters and a flat support. Our formulation can be used to determine the mechanical properties of soft particles by comparison with experimental measurement of indentation. Although such particles, which can undergo large deformation, have no bending stiffness, the enclosed fluid provides sufficient resistance to the deformation and contributes to the structural stiffness. The resistance to deformation also depends on the sharpness of the indenter. This study provides valuable information on the indentation force, fluid pressure, contact areas and principal stress/stretch distributions in the membrane. It was observed that the indenter force, fluid pressure and contact area depend

inversely on the sharpness of the indenter. While, for large inflations $\bar{r}_0 > 2.0$, the two principal stresses/stretches are almost equal everywhere, for small inflations, $\bar{r}_0 < 2.0$, the two principal stresses/stretches differ. The location and value of the maximum principal stresses/stretches show strong dependency on the indenter sharpness. For flat indenter the maximum stresses/stretches are at the equator, while for conical sharp indenters, they are located at the tip of the indenter. Our model predicts accurately the nonlinear response of certain particle types for large deformation and shows excellent agreement with experiments.

Our model can also accommodate different hyperelastic constitutive membrane laws and compressible fluid. This model provides insights into the complex response of elastic spherical particles and can be used to determine the mechanical properties of soft particles from indentation experiments. In addition, the model can determine the distribution of stresses in the peripheral membrane which can be used to predict the penetration condition associated with capsules holding and releasing their content and the microinjection techniques. The model presented here is very simple and therefore, it has certain limitations. In the current model, the friction and adhesion of the membrane with the indenters and the flat support are not considered. Moreover, the viscous properties of the membrane and the enclosed fluid are ignored.

Bibliography

[1] K. Wan, V. Chan, and D. A. Dillard, "Constitutive equation for elastic indentation of a thin-walled bio-mimetic microcapsule by an atomic force microscope tip," *Colloid Surf.*, vol. 27, pp. 241–248, 2002.

[2] F. Rico, P. Roca-Cusachs, N. Gavara, R. Farre, M. Rotger, and D. Navajas, "Probing mechanical properties of living cells by atomic force microscopy with blunted pyramidal cantilever tips," *Phys. Rev. E*, vol. 72, pp. 021914(1–10), 2005.

[3] Z. Lu, P. C. Y. Chen, H. Luo, J. Nam, R. Ge, and W. Lin, "Models of maximum stress and strain of zebrafish embryos under indentation," *J. Biomech.*, vol. 42, pp. 620–625, 2009.

[4] K. Soppimath, T. Aminabhavi, A. Dave, S. Kumbar, and W. Rudzinski, "Stimulus-responsive smart hydrogels as novel drug delivery systems," *Drug Del. Ind. Pharm.*, vol. 28, pp. 957–974, 2002.

[5] A. E. Smith, Z. Zhang, C. R. Thomas, K. E. Moxham, and A. P. J. Middelberg, "The mechanical properties of saccharomyces cerevisiae," *Proc. Natl. Acad. Sci.*, vol. 97, pp. 9871–9874, 2000.

[6] K. Liu, "Deformation behavior of soft particles: a review," *J. Phys. D: Appl. Phys.*, vol. 39, pp. 189–199, 2006.

[7] V. D. Gordon, X. Chen, J. W. Hutchinson, A. R. Bausch, M. Marquez, and D. A. Weitz, "Self-assembled polymer membrane capsules inflated by osmotic pressure," *J. Am. Chem. Soc.*, vol. 126, pp. 141177–14122, 2004.

[8] J. Q. Feng, "Relative importance of elctrostatic forces on powder particles," *Powder Tech.*, vol. 135-136, pp. 65–75, 2003.

[9] D. Vella, A. Ajdari, A. Vaziri, and A. Boudaoud, "The indentation of pressurized elastic shells: from polymeric capsules to yeast cells," *J. R. Soc. Interf.*, vol. 9, pp. 448–455, 2012.

[10] G. Schmid-Schonbein, K-L.P.Sung, H. Tozeren, R. Skalak, and S. Chien, "Passive mechanical properties of human leukocytes," *Biophys. J.*, vol. 36, pp. 243–256, 1981.

[11] K. P. Sung, C. Dong, G. W. Schmid-Schonbein, S. Chien, and R. Skalak, "Leukocyte relaxation properties," *Biophys. J.*, vol. 54, pp. 331–336, 1988.

[12] L. A. Taber, "Compression of fluid-filled spherical shells by rigid indenters," *J. Appl. Mech.*, vol. 50, pp. 717–722, 1983.

[13] K. K. Liu, D. R. Williams, and B. J. Briscoe, "Compressive deformation of a single microcapsule," *Phys. Rev. E*, vol. 54, pp. 6673–6680, 1996.

[14] M. Rachik, D. Barthes-Biesel, M. Carin, and F. Edwards-Levy, "Identification of the elastic properties of an artifical capsule membrane with the compression test: effect of thickness," *J. Colloid. Interf. Sci.*, vol. 301, pp. 217–226, 2006.

[15] Y. Lin, D. Wang, W. Lu, Y. Lin, and K. Tung, "Compression and deformation of soft spherical particles," *Chem. Eng. Sci.*, vol. 63, pp. 195–203, 2008.

[16] W. Lu, K. Tung, S. Hung, J. Shiau, and K. Hwang, "Compression of deformable gel particles," *Powder Technol.*, vol. 116, pp. 1–12, 2001.

[17] B. Nadler, "On the contact of a spherical membrane enclosing a fluid with rigid parallel planes," *International Journal of Non-Linear Mechanics.*, vol. 45, pp. 294–300, 2010.

[18] B. Daily, E. L. Elson, and G. I. Zahalak, "Cell poking. determination of the elastic area compressibility modulus of the erythrocyte membrane," *Biophys. J.*, vol. 45, pp. 671–682, 1984.

[19] J. Arfsten, S. Leupold, C. Bradtmoller, I. Kampen, and A. Kwade, "Atomic force microscopy studies on the nanomechanical properties of saccharomyces cerevisiae," *Colloids Surf. B Biointerf.*, vol. 79, pp. 284–290, 2010.

[20] V. C. Bui, Y. U. Kim, and S. S. Choi, "Physical characteristics of saccharomyces cerevisiae," *Surf. Interface Anal.*, vol. 40, pp. 1323–1327, 2008.

[21] J. A. C. Santos, L. M. Rebelo, A. C. Araujo, E. B. Barros, and J. S. de Sousa, "Thickness-corrected model for nanoindentation of thin films with conical indenters," *Soft Matter*, vol. 8, pp. 4441–4448, 2012.

[22] C. A. Tweedie and K. J. V. Vliet, "Contact creep compliance of viscoelastic materials via nanoindentation," *J. Mater. Res.*, vol. 21, pp. 1576–1589, 2006.

[23] Y. Sun, K. Wan, K. P. Roberts, J. C. Bischof, and B. J. Nelson, "Mechanical property characterization of mouse zona pellucida," *IEEE Trans. Nanobisci.*, vol. 2, pp. 279–286, 2003.

[24] M. Radmacher, M. Fritz, J. P. Cleveland, D. A. Walters, and P. K. Hansma, "Imaging adhesion forces and elasticity of lysozyme adsorbed

on mica with the atomic force microscope," *Langmuir*, vol. 10, pp. 3809–3814, 1994.

[25] M. Radmacher, M. Fritz, C. M. Kacher, J. P. Cleveland, and P. K. Hansma, "Meauring the viscoelastic properties of human platelets with the atomic force microscope," *Biophys. J.*, vol. 70, pp. 556–567, 1996.

[26] X. Li and B. Bhushan, "A review of nanoindentation continuous stiffness measurement technique and its applications," *Mater. Charact.*, vol. 48, pp. 11–36, 2002.

[27] I. N. Sneddon, "The relation between load and penetration in the axisymmetric boussinesq problem for a punch of arbitrary profile," *Int. J. Engr. Sci.*, vol. 3, pp. 47–57, 1965.

[28] E. K. Dimitriadis, F. Horkay, J. Maresca, B. Kachar, and R. S. Chadwick, "Determination of elastic moduli of thin layers of soft material using the atomic force microscope," *Biophys. J.*, vol. 82, pp. 2798–2810, 2002.

[29] L. A. Taber, "Large deflection of a fluid-filled spherical shell under a point load," *J. Appl. Mech.*, vol. 49, pp. 121–128, 1982.

[30] T. Sohail and B. Nadler, "On the contact of an inflated spherical membrane-fluid structure with a rigid conical indenter," *Acta Mech.*, vol. 218, pp. 225–235, 2011.

[31] D. Theret, M. Levesque, M.Sato, R. Nerem, and L. Wheeler, "The application of a homogeneous half-space model in the analysis of endothelial cell micropipette measurements," *ASME J. Biomech. Eng.*, vol. 110, pp. 190–199, 1988.

[32] T. Sohail, T. Tiang, and B. Nadler, "Micropipette aspiration of an inflated fluid-filled spherical membrane," *Z. Angew. Math. Phys.*, Available online, 2011.

[33] A. Vaziri, "Mechanics of highly deformed elastic shells," *Thin Wall. Struct.*, vol. 47, pp. 692–700, 2009.

[34] J. J. Foo, K. K. Liu, and V. Chan, "Viscous drag of deformed vesicles in optical trap: Experiments and simulations," *Amer. Inst. Chem. Eng.*, vol. 50, pp. 249–254, 2004.

[35] S. Rancourt-Grenier, M. Wei, J. Bai, A. Chiou, P. Bareil, P. Duval, and Y. Sheng, "Dynamic deformation of red blood cell in dual-trap optical tweezers," *Opt. Expr.*, vol. 18, pp. 10462–10472, 2010.

[36] R. P. Joshi, Q. Hu, K. H. Schoenbach, and S. J. Beebe, "Simulations of electroporation dynamics and shape deformation in biological cells subjected to high voltage pulses," *IEEE Trans. Plasma Sci.*, vol. 30, pp. 1536–1546, 2002.

[37] J. I. Rey, R. J. Connolly, M. J. Jaroszeski, and A. M. Hoff, "Electrostrictive forces on vesicles with compartmentalized permittivity and conductivity conditions," *IEEE Trans. Dielectr. Electr. Insul.*, vol. 16, pp. 1280–1287, 2009.

[38] J. Guck, R. Ananthakrishnan, C. C. C. H. Mahmood, T. J. Moon, and J. Kas, "The optical stretcher: A novel laser tool to micromanipulate cells," *Biophys. J.*, vol. 81, pp. 767–784, 2001.

[39] A. L. Weisenhorn, M. Khosandi, S. Kasas, V. Gotzos, and H. J. Butt, "Deformation and height anomaly of soft surfaces studied with an AFM," *Nanotech.*, vol. 4, pp. 106–113, 1993.

[40] X. Yao, J. Walter, S. Burke, S. Stewart, M. H. Jericho, D. Pink, R. Hunter, and T. Beveridge, "Atomic force microscopy and theoretical considerations of surface properties and turgor pressures of bacteria," *Coll. Surf.*, vol. 23, pp. 213–230, 2002.

[41] H. Hertz, "ber die berhrung fester elastischer krper," *J. Reine Angew. Math*, vol. 92, pp. 156–171, 1881.

[42] J. Boussinesq, *Application des Potentiels a L'etude de l'equilibre et due Mouvement des Solides Elastique.* Paris: Gauthier Villars, 1885.

[43] K. L. Johnson, K. Kendall, and A. D. Roberts, "Surface energy and the contacts of elastic solids," *Proc.R.Soc.London. A*, vol. 324, pp. 301–313, 1971.

[44] B. V. Derjaguin, V. M. Muller, and Y. P. Toporov, "Effect of contact deformations on the adhesion of particles," *J. Colloid. Interf. Sci.*, vol. 53, pp. 314–325, 1975.

[45] R. Wang, Q. Jiao, and D. Wei, "Mechanical response of single plant cells to cell poking: a numerical simulation model," *J. Integ. plant bio.*, vol. 48, pp. 700–705, 2006.

[46] M. Radmacher, M. Fritz, and P. K. Hansma, "Imaging soft samples with the atomic force microscope: Gelatin in water and propanol," *Biophys. J.*, vol. 69, pp. 264–270, 1995.

[47] J. D. Humphrey, "Review paper: Continuum biomechanics of soft biological tissues," *Proc. R. Soc. Lond. A*, vol. 459, pp. 3–46, 2003.

[48] W. Feng and W.-H. Yang, "On the contact problem of an inflated spherical nonlinear membrane," *J. Appl. Mech.*, vol. 41, pp. 209–214, 1973.

[49] T. Lardner and P. Pujara, "Compression of spherical cells," *Mechanics Today.*, vol. 5, pp. 161–176, 1980.

Chapter 5

Micropipette aspiration of an inflated fluid-filled spherical membrane[1]

5.1 Introduction

This work is motivated by the micropipette experiments that have been widely used to determine the mechanical response of cells. The human cell is a complicated structure that contains nucleus, cytoplasm, protein fibers, plasma membrane, and a network of different organelles [1,2], which work together to maintain the daily activities of human beings. Living cells always remain in an active state and are constantly involved in various physio-chemical reactions. In response to external mechanical stresses, cells undergo biophysical changes influenced by their interaction with the extracellular matrix [3]. Depending upon the surrounding environment, cells go through mechanical changes such as contraction, relaxation, and stretching. In addition, different cells (e.g., leukocyte, granulocyte, endothelial, chondrocyte and human neutrophils) respond differently to external loading [2, 4–8]. To regulate cell activities, it is essential to understand how the different organelles in a cell contribute to its mechanical properties and how a cell behaves under typical loading conditions.

---

[1]A version of this chapter was published. Touqeer Sohail, Tian Tang and Ben Nadler, Z. Angew. Math. Phys., 63 , 737-757, 2012.

This has become an active area of research in recent years [3, 7–10].

The micropipette technique has been widely used to investigate the mechanical and adhesive properties of living cells [1–20]. The goal of the micropipette technique is to measure the mechanical properties of the cell such as the bending stiffness of the membrane, viscosity, relaxation during recovery after being aspirated into a micropipette [5, 6, 8] and minute adhesive forces during detachment from a substrate [19, 20]. In a typical micropipette experiment, a micropipette of radius 0.2-0.8 times the cell radius is used and a suction pressure is applied so that the pressure inside the micropipette is smaller than that outside. Such a pressure difference causes the cell to be aspirated into the micropipette and the cell's deformation can be captured by a high resolution microscope [4]. This technique has been applied to various active and passive living cells such as granulocyte, leukocyte, erythrocyte, endothelial, red blood cell, chondrocyte and human neutrophil. In general, it has been observed that, at small suction pressure, the cell's response is elastic [14], and upon removal of the suction pressure, the cell completely recovers its original shape. When the suction pressure exceeds a threshold value, the cell exhibits liquid-like behavior [1] and spontaneously flows into the micropipette. The resistance to aspiration decreases as the ratio between the micropipette diameter and the cell diameter increases. Based on different mechanics models, the micropipette technique has also been used for the design of force transducers to measure forces in the piconewton range [21–23]. Here, a cell is aspirated by the micropipette at one end and a microbead (or another cell) is attached at the other end. The membrane tension resists the displacement of the bead [22, 23] and the stiffness of the force transducer is changed by changing the suction pressure [22, 23]. With a mechanics model for the cell, the force on the bead is deduced, and the force-displacement relation is used to determine the bonding characteristics [20, 24] between the cell and the bead.

Through the micropipette experiments, different properties have been identified for different types of cells. For example, aspiration of leukocyte at three different positions has shown similar behavior, which suggests that it has nearly homogeneous mechanical properties [4]. The axisymmetric recovery of leukocyte upon removal of external load provides further support [5]. It has also been found that some cells are morphologically heterogeneous because of non-uniform distribution of organelles and cytoskeletal elements in the cytoplasm [4, 12]. During micropipette aspiration, endothelial cells have shown greater stiffness and viscosity as compared to erythrocytes [7]. White blood cells are more resistive than red blood cells and, therefore, larger suction pressure is required to deform white blood cells [5, 15]. Based on a theoretical model, Jones *et al.* [8] interpreted the data from micropipette experiments for normal chondrocytes and osteoarthritic chondrocytes, and argued that their Young's moduli are quite close, whereas there is significant volumetric difference after deformation.

The cell's behavior during the micropipette experiment is usually represented by a graph where the aspiration length (i.e., the projected length of the cell inside the micropipette) is plotted against the suction pressure. For the neutrophil, such a graph contains an initial linear regime, which reflects its linear elastic response at small deformation [4, 9]. The subsequent non-linear regime, however, suggests its non-linear behavior at large deformations [9]. In general, it has been observed that the cell behaves in an elastic manner when being rapidly aspirated and expelled from the micropipette [13, 16]. Specifically, the cell returns to its original shape upon removal of the pressure. The recovery, however, depends on how long the cell is held in the micropipette [13]. The longer the cell is kept deformed, the more slowly it recovers its original shape [5].

Several mechanics models have been developed to explain the experimen-

tal observations. Based on whether the cell is considered a solid or a liquid (Newtonian or Maxwell liquid), these models can be divided into two main categories: (1) solid-like models and (2) liquid-like models. Bagge *et al.* [25] suggested that the neutrophil can be modeled as a solid body when deformed. Jones *et al.* [8] showed that the chondrocyte behaves as a viscoelastic solid, where the aspiration length is significantly greater than the micropipette radius. Sato *et al.* [7] suggested that the cell's major resistance to aspiration is provided by its cortical layer and that the cell can be modeled as a shell with thickness equal to that of the cortical layer. They also proposed that, if the micropipette radius is small, a plate model with thickness equal to that of the cortical layer can also be considered [7]. Yeung *et al.* [1] and Evan *et al.* [6,17] demonstrated the liquid-like behavior of neutrophil, namely that it continuously flows into the micropipette when the suction pressure exceeds a threshold value. The threshold pressure is found to be inversely proportional to the micropipette radius [1]. Dong *et al.* [14] modeled leukocyte by a shell containing a Maxwell fluid, but pointed out a few deficiencies of using small strain theory in their work. Hochmuth *et al.* [15] observed the shear thinning behavior of the cytoplasm at high rates of deformation (i.e., the viscosity decreases as the rate of deformation increases). Tran-Son-Tay *et al.* [13] proposed that the neutrophil behaves like Newtonian liquid if it is held in the micropipette for a long time and like Maxwell liquid if it is held for a short time and undergoes rapid deformation. Hochmuth *et al.* [16], however, suggested that the neutrophil does not behave as simple Newtonian or Maxwell liquid because the cytoplasmic viscosity decreases as deformation decreases.

The solid-like and liquid-like models are simplified cell models, and neither can adequately capture the overall cell behavior. The solid-like model [4] and the Maxwell liquid-like model [14] adequately capture the initial elastic response during the aspiration and expulsion from the micropipette, but the

Newtonian liquid-like model [13,15] does not. The solid-like model with small strain assumption [4] can adequately fit the experimental data during loading and unloading when the deformation is small, but are not suitable for large or long term deformation [6]. In fact, because of the scarcity of the information about the properties and interactions of the materials that constitute cell, it is very difficult for any single model to fit cell's natural response for both small and large deformations.

Along with the above simplified continuum models, the tensegrity cell model has been proposed. This model uses cables and struts to represent the cell structure [26]. The cables are initially stretched in the reference state by the struts. The entire structure is stretched uniaxially and its deformation is determined. In [18], the cytoskeletal material is modeled as a network of viscoelastic links, which is capable of predicting its viscosity, elasticity, shear thinning and thixotropy. However, because this model is two-dimensional, it does not provide good comparison with experimental measurements on the three-dimensional cell structure. A combination of elements from the continuum and tensegrity models [9] is also suggested to study cell mechanics.

Despite the different levels of complexity involved in the common cell models, several assumptions were often made. Firstly, it was assumed that the deformation of the cell during aspiration is small (i.e., the reference and current configurations are indistinguishable). Secondly, the geometry of the cell outside the micropipette was considered to be part of a sphere even after deformation. Finally, it was assumed that the tension in the cell membrane is a constant and independent of position. However, it is not clear whether these assumptions truly reflect the actual physical situation, especially since large deformation can be expected during aspiration.

In this work, we attempt to characterize the behavior of a spherical cell in a micropipette experiment using a simple continuum mechanics model, while

101

removing the above assumptions. We recognize that the mechanical properties of the cortical layer are in general very different from the liquid core [1], which is why we model them separately. Specifically, the cell membrane is assumed to be in a passive state and is modeled as a homogenous, isotropic and elastic membrane. The membrane is assumed to be a hyper-elastic material and can sustain very large deformation. The fluid inside the membrane is considered to be incompressible, so that its volume is conserved. Equilibrium configurations of the fluid-filled membrane during micropipette aspiration are calculated for different micropipette radii and different suction pressures. Although possible viscous behavior of the membrane and the fluid are not considered in this work, compared with previous work, our model has several advantages. It is simple and involves very few parameters. It does not require the assumption of spherical shape for the cell segments during aspiration. It considers geometrical nonlinearity and can capture very large deformation. In fact, our results show very good agreement with experimental data, indicating that the nonlinear membrane model may be suitable to accurately describe the mechanical behaviors of certain cells.

This chapter is organized as follows. In Section 5.2, we provide the formulation for the geometry of a nonlinear membrane, the equilibrium equation, the constitutive relation and the contact condition during micropipette aspiration. The numerical procedure is described in Section 5.3. The results and discussion are presented in Section 5.4 and conclusions are given in Section 5.5.

5.2 Formulation

5.2.1 Geometry

As shown in Figure 5.1(a), the membrane under consideration is a sphere of radius R in the reference configuration κ (taken to be the stress-free state) and the convected spherical coordinates $\{\phi, \theta\}$ are used to define the position of a material point X on the membrane surface. The membrane is inflated to radius r_0 filled with fluid and then aspirated by a rigid micropipette of radius ρ. In Figure 5.1(b), A and B correspond to the leftmost and rightmost
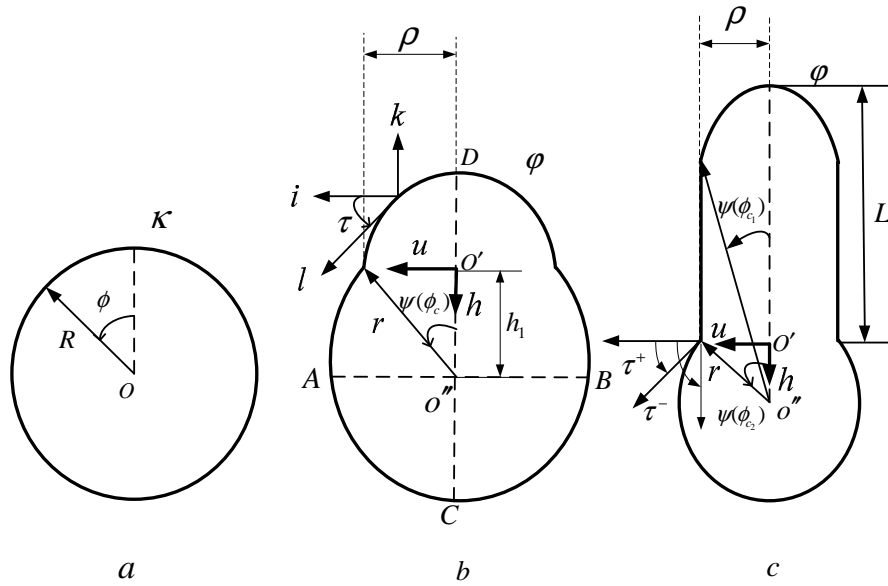
Figure 5.1: Coordinate system for the membrane under micropipette aspiration. ϕ is the angle measured in the reference configuration κ and ψ in the deformed configuration φ and $\tau^- = \lim_{\phi \to \bar{\phi}^-} \tau$ and $\tau^+ = \lim_{\phi \to \bar{\phi}^+} \tau$ are the tangential angles at the kink. (a) Referential state (b) Deformed equilibrium configuration when membrane is not in contact with the micropipette wall (c) Deformed equilibrium configuration when membrane is in contact with the micropipette wall.

points of the membrane, while O'' is the intersect of AB and the symmetry line of the membrane. $r(\phi)$ is the distance from O'' to a point on the deformed membrane and $\psi(\phi)$ is the meridian angle. As explained in Chapter 2, the

first order ODEs for $r'(\phi)$ and $\psi'(\phi)$ are

$$r' = \lambda R \sin(\psi - \tau), \quad \psi' = \frac{\lambda R}{r} \cos(\psi - \tau), \tag{5.1}$$

where $()' = d()/d\phi$, λ is the meridian stretch (the hoop stretch denoted by μ), and τ is the tangent angle on the membrane surface. Through geometrical relationship, in Figure 5.1(b), r in the deformed membrane can be calculated as

$$r = \frac{(h_1 - h)}{\cos(\psi)} \tag{5.2}$$

where h_1 is the distance from the horizontal axis AB to the lower edge of the micropipette. Substituting (5.2) into (5.1)$_2$, $\psi'(\phi)$ in the deformed membrane is given by

$$\psi' = \frac{\lambda R \cos(\psi)}{(h_1 - h)} \cos(\psi - \tau). \tag{5.3}$$

Since the deformed membrane does not possess spherical symmetry, but rather cylindrical symmetry, it is more convenient to employ cylindrical coordinates. In the following, the formulation will be recast in terms of $u(\phi)$ and $h(\phi)$, which are the horizontal and vertical positions defined with respect to the origin O' located at the centre of the lower edge of the micropipette (see Figure 5.1 (b)). The following relationships can be easily derived

$$u = r \sin \psi, \quad h = h_1 - r \cos \psi, \tag{5.4}$$

where h_1 is the distance from O'' to the center of the micropiette, O'. Differentiating (5.4) and afterward substituting equation (5.1) into it, the first order ODEs for $u'(\phi)$ and $h'(\phi)$ are

$$u' = \lambda R \cos \tau, \quad h' = \lambda R \sin \tau. \tag{5.5}$$

Using (5.4) and (5.5), expressions for $r'(\phi)$ and $\psi'(\phi)$ can be written in terms of $u(\phi), u'(\phi), h(\phi)$ and $h'(\phi)$ as

$$r' = \frac{u'u - h'h_1 + h'h}{u}\sin(\tan^{-1}(\frac{u}{h_1 - h})), \quad \psi' = \frac{u'(h_1 - h) + h'u}{u^2}(\sin(\tan^{-1}(\frac{u}{h_1 - h})))^2.$$

(5.6)

The principal stretches λ and μ can also be written in terms of $u(\phi)$, $h(\phi)$ and their derivatives as

$$\lambda = \frac{\sin(\tan^{-1}(\frac{u}{h_1 - h}))}{uR}\sqrt{(u'u - h'h_1 + h'h)^2 + (u'h_1 - u'h + h'u)^2}, \quad \mu = \frac{u}{R\sin\phi}.$$

(5.7)

5.2.2   Equilibrium

The derivation of the equilibrium equations follows the same procedure as shown in Chapter 3, except that the traction on the membrane due to the indenter is replaced by the pressure from outside of the membrane. Let P_1 and P_2 denote the pressure inside the micropipette and the outside ambient pressure, respectively. The traction on the membrane due to the fluid outside the membrane is

$$\mathbf{f}_v = -p\mathbf{n},$$

(5.8)

where $\mathbf{n}$ is the outward normal to the deformed membrane surface, $p = P_1$ on the aspirated part of the membrane not in contact with the micropipette wall, and $p = P_2$ on the part of the membrane outside the micropipette. The equilibrium equations are, therefore, given by

$$\lambda' = \frac{(w_\mu - \lambda w_{\lambda\mu})\cos\tau - (w_\lambda - \mu w_{\lambda\mu})\cos\phi}{w_{\lambda\lambda}\sin\phi},$$

(5.9)

$$\tau' = \frac{\lambda\mu R(p_f - p)}{w_\lambda} - \frac{w_\mu \sin\tau}{w_\lambda \sin\phi}.$$

(5.10)

105

As shown in Figure 5.1(b,c), at the lower edge of the micropipette there is a "kink" in the deformed membrane, where curvature is undefined. Figure 5.2(a) shows the balance between the force exerted by the micropipette and the tension in the stretched membrane at the kink. The vertical force exerted by
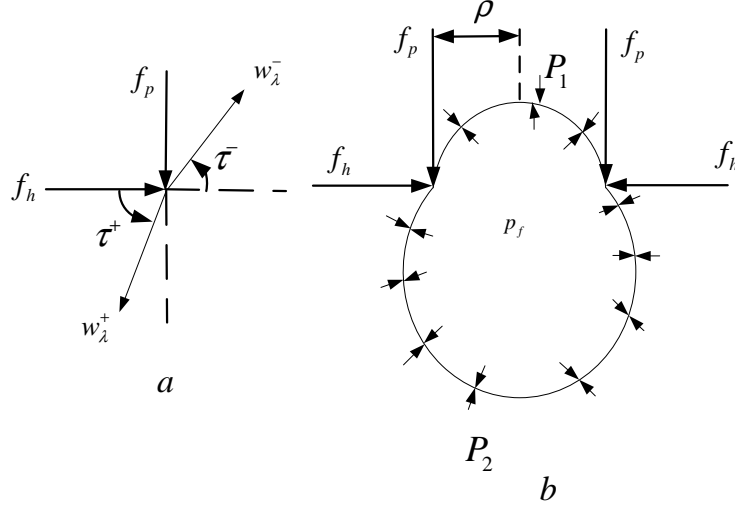
Figure 5.2: (a) Free body diagram for the kink of the membrane in contact with the micropipette. The principal stresses at the kink are $w_\lambda^- = \lim_{\phi \to \bar{\phi}^-} w_\lambda$ and $w_\lambda^+ = \lim_{\phi \to \bar{\phi}^+} w_\lambda$. (b) Equilibrium of the membrane with inside fluid pressure p_f, micropipette vertical force f_p, micropipette horizontal force f_h and external pressures P_1 and P_2.

the micropipette in contact with the membrane is

$$f_p = - [w_\lambda \sin \tau]_{\bar{\phi}}, \tag{5.11}$$

where

$$[w_\lambda \sin \tau]_{\bar{\phi}} = (w_\lambda \sin \tau)^+ - (w_\lambda \sin \tau)^- = \lim_{\phi \to \bar{\phi}^+} w_\lambda \sin \tau - \lim_{\phi \to \bar{\phi}^-} w_\lambda \sin \tau \tag{5.12}$$

is the jump at the kink, i.e., at $\bar{\phi} = \phi_c$, when the membrane is not in contact with the micropipette wall and, at $\bar{\phi} = \phi_{c_2}$, when it is in contact with the micropipette wall, as shown in Figure 5.1 (b) and (c). The domain $\phi_{c_1} \leqslant \phi \leqslant$

106

ϕ_{c_2} corresponds to the part of the membrane in contact with the micropipette wall as shown in Figure 5.1 (c). $\tau^- = \lim_{\phi \to \bar{\phi}^-} \tau$ is the tangential angle of the membrane inside the micropipette at the kink and $\tau^+ = \lim_{\phi \to \bar{\phi}^+} \tau$ is the tangential angle of the membrane outside the micropipette at the kink (see Figure 5.1(c)). It should be noted that the vertical force f_p is the force per unit length, measured in the reference configuration, of the contact line between the membrane and the end of the micropipette. The balance between the external pressures and the micropipette force is shown in Figure 5.2(b). Since the length of the contact line in the reference configuration is $R \sin \bar{\phi}$, the total vertical force from the pipette is $f_p 2\pi R \sin \bar{\phi}$. Therefore, the suction pressure (i.e., the pressure difference inside and outside of the micropipette) required to aspirate the membrane is

$$\Delta P = \frac{2}{\rho^2} f_p R \sin \bar{\phi}. \tag{5.13}$$

Here, $\bar{\phi} = \phi_c$, when the membrane is not in contact with the micropipette wall and $\bar{\phi} = \phi_{c_2}$, when the membrane is in contact with the micropipette wall. $\Delta P = P_2 - P_1$ is the pressure difference and ρ is the radius of the micropipette.

5.2.3   Constitutive relationship

The strain energy function for the membrane is described in this work by the neo-Hookean material as [27, 28]

$$w(\lambda, \mu) = \frac{G}{2} \left(\lambda^2 + \mu^2 + (\lambda\mu)^{-2} - 3 \right), \tag{5.14}$$

where G is a material constant. Since the membrane cannot sustain any negative stress, the conditions $w_\lambda \geqslant 0$ and $w_\mu \geqslant 0$ need to hold everywhere in

the membrane [27]. If w_λ or w_μ are found to be negative, then, physically, this corresponds to wrinkling of the membrane and the equilibrium solution is not physically admissible. The spherical membrane with initial radius R is inflated by the enclosed fluid to radius r_0. For such homogeneous deformations, $\psi = \tau = \phi$, since the sphere is mapped into a sphere, and the principle stretches are $\lambda = \mu = \lambda_i = \frac{r_0}{R}$. Using (5.10) and (2.31), the initial pressure in the fluid is

$$p_f^0 = \frac{2G}{r_0} \left(1 - \left(\frac{R}{r_0} \right)^6 \right) + P_2. \tag{5.15}$$

The fluid is taken to be incompressible and the pressure p_f in the aspirated membrane is determined by the incompressibility condition

$$J_f = \frac{V}{V_0} = 1, \tag{5.16}$$

where $V_0 = \frac{4}{3}\pi r_0^3$ is the volume of the inflated spherical membrane before aspiration. V is the volume of the fluid enclosed in the membrane after it has been aspirated and can be calculated using

$$V = \pi \int_{h_C}^{h_D} u^2 dh, \tag{5.17}$$

where the position of points C and D are indicated in Figure 5.1(b).

5.2.4   Contact conditions

The micropipette aspiration of the membrane consists of two stages. When the suction pressure is small, the membrane is only in contact with the micropipette at its lower edge and there is no contact between the membrane and the micropipette wall, as shown in Figure 5.1(b). When the suction pressure is sufficiently large, contact is formed with the micropipette wall, as shown in Figure 5.1(c). For the first stage, the membrane can be separated into two

regions: (1) the aspirated part and (2) the external part. For the second stage, the membrane has three regions: (1) the part inside the micropipette, but not in contact with the micropipette wall, (2) the part inside the micropipette and in contact with the micropipette wall and (3) the external part.

5.2.4.1 First stage: no contact with the micropipette wall

At small aspiration pressure, the membrane is only in line contact with the micropipette edge. Equation (5.10) for the aspirated region, where $p = P_1$, becomes

$$\tau' = \frac{\lambda \mu R(p_f - P_1)}{w_\lambda} - \frac{w_\mu \sin \tau}{w_\lambda \sin \phi}. \tag{5.18}$$

The three first order ODEs $(5.5)_1$, (5.9) and (5.18) are to be solved for the aspirated part of the membrane $0 \leqslant \phi \leqslant \phi_c$. The boundary conditions (BCs) in the aspirated region are

$$u(0) = 0, \quad \tau(0) = 0, \quad u(\phi_c) = \rho, \tag{5.19}$$

as shown in Figure 5.1. Equation (5.10) for the external part of the membrane with $p = P_2$ becomes

$$\tau' = \frac{\lambda \mu R(p_f - P_2)}{w_\lambda} - \frac{w_\mu \sin \tau}{w_\lambda \sin \phi}. \tag{5.20}$$

The three first order ODEs $(5.5)_1$, (5.9) and (5.20) are required in the external part of the membrane $\phi_c < \phi \leqslant \pi$. The BCs for this region are

$$u(\phi_c) = \rho, \quad u(\pi) = 0, \quad \tau(\pi) = \pi, \tag{5.21}$$

as shown in Figure 5.1(b). Once λ and τ are determined, equation $(5.5)_2$ can be integrated with respect to the origin O', where $h(\phi_c) = 0$, and the configuration of the deformed membrane is entirely determined. It should be

109

noted that there are two unknowns, p_f in the governing equation and ϕ_c in the BCs above. Therefore, two additional conditions are required to complete the formulation of the problem. These equations are the incompressibility

$$\frac{V}{V_0} = 1, \tag{5.22}$$

and the equilibrium of the whole membrane-fluid structure

$$\pi \rho^2 \Delta P + 2\pi R \sin \bar{\phi} f_p = 0, \tag{5.23}$$

where the first term is the resultant force due to the pressure difference and the second term is the resultant vertical force applied by the micropipette edge. In the case of no contact between the membrane and the micropipette wall, $\bar{\phi} = \phi_c$.

5.2.4.2 Second stage: contact with the micropipette wall

At large suction pressure, the aspirated membrane forms contact with the micropipette wall. The three first order ODEs $(5.5)_1$, (5.9) and (5.18) are to be solved for the aspirated yet non-contacting part of the membrane $0 \leqslant \phi \leqslant \phi_{c_1}$. The BCs for this region are

$$u(0) = 0, \quad \tau(0) = 0, \quad u(\phi_{c_1}) = \rho, \tag{5.24}$$

as shown in Figure 5.1(c). For the part of the membrane, $\phi_{c_1} \leqslant \phi \leqslant \phi_{c_2}$, which is in contact with the micropipette wall, $\tau = \pi/2$ and $u = \rho$. Thus, in this region,

$$\tau' = 0, \quad u' = 0. \tag{5.25}$$

Hence, only one governing equation (5.9) for λ is required. The boundary condition in this region is the continuity of λ at ϕ_{c_1} (i.e., $\lim_{\phi \to \phi_{c_1}^+} \lambda = \lim_{\phi \to \phi_{c_1}^-} \lambda$),

as required by the jump condition in the absence of concentrated load, where $\lim_{\phi \to \phi_{c_1}^-} \lambda$ is known from the solution to the aspirated, but non-contacting part of the membrane. The three governing equations for the exterior part of the membrane, $\phi_{c_2} < \phi \leqslant \pi$, are $(5.5)_1$, (5.9) and (5.20). The BCs for this part are

$$u(\phi_{c_2}) = \rho, \quad u(\pi) = 0, \quad \tau(\pi) = \pi, \tag{5.26}$$

as depicted in Figure 5.1(c). After knowing λ and τ, equation $(5.5)_2$ is integrated with $h(\phi_{c_2}) = 0$. Two unknowns ϕ_{c_1} and ϕ_{c_2} are present in the BCs and the third unknown p_f is present in the governing equation for τ'. These three unknowns require three aditional conditions. In addition to the two conditions (5.22) and (5.23) introduced in 5.2.4.1, the third condition is

$$\tau(\phi_{c_1}) - \pi/2 = 0, \tag{5.27}$$

which is the continuity of τ as required by the jump condition in the absence of concentrated load.

5.3 Numerical Algorithm

Experimentally, in the micropipette aspiration, the suction pressure is controlled and the deformation of the cell is measured. This corresponds to solving the above defined BVPs for given parameters R, r_0, G, ρ, P_1 and P_2. Considering, for example, the case where the membrane forms contact with the micropipette wall, one would specify P_1 and P_2, and solve the BVP defined in 5.2.4. Consequently, ϕ_{c_1} and ϕ_{c_2} will be part of the solution. However, numerically, it is difficult to solve a BVP without knowing the boundary locations (i.e., how much of the membrane has been aspirated and how much is in contact with the micropipette wall). In order to avoid this difficulty, in

our calculation, we specify the domain boundary ϕ_{c_2} and calculate the corresponding suction pressure. This approach facilitates the numerical calculation and also allows us to establish the relationship between the suction pressure and deformation.

The membrane, $0 \leqslant \phi \leqslant \pi$, is discretized into n elements with equal spacing $\Delta\phi$. The lower edge of the micropipette is placed on a sequence of nodes $j = q, q+1, \ldots n$ on the membrane, where $j = q$ corresponds to $\Delta P = 0$ and no deformation in the membrane. For each j, the deformation of the membrane is obtained by solving the BVP and the corresponding suction pressure is determined. The shooting method is employed to solve the BVP. Using this method, the BVP is replaced by two initial value problems. The membrane is decomposed into two parts, the part inside the micropipette, $0 \leqslant \phi < \bar{\phi}$, and the part outside the micropipette, $\bar{\phi} < \phi \leqslant \pi$. For the the first stage (no contact with the wall), given P_2, the guessed values $\lambda_1 = \lambda(0)$, $\lambda_2 = \lambda(\pi)$, p_f, and P_1 are used to shoot for the boundary conditions $u^+(\phi_c) = u^-(\phi_c) = \rho$, and the two additional conditions (5.22) and (5.23). For the second stage (contact with the micropipette wall), the guessed values λ_1, λ_2, p_f, P_1 and ϕ_{c_1} are used to shoot for the boundary conditions $u^+(\phi_{c_1}) = u^-(\phi_{c_2}) = \rho$, and the three additional conditions (5.22), (5.23) and (5.27). The fourth order Runge-Kutta method was used to integrate the equations. After $\{\lambda, \tau, \mu, h\}$ are obtained, the hoop stretch μ can be determined from (4.4) and the principal stresses can be calculated from (2.27).

5.4 Results and Discussion

The deformed equilibrium configuration of the aspirated membrane is explained using the following normalized parameters:

$$\bar{\rho} = \frac{\rho}{r_0}, \quad \bar{f}_p = \frac{f_p R}{G\rho}, \quad \bar{L} = \frac{L}{R}, \quad \bar{r}_0 = \frac{r_0}{R}. \tag{5.28}$$

Here, $\bar{\rho}$ is the micropipette radius normalized by the inflated radius of the membrane, $\overline{f_p}$ is the normalized micropipette force and $\bar{L}$ is the aspirated length normalized by the referential radius of the membrane shown in Figure 5.1. The fluid pressure inside the membrane, the pressure inside the micropipette and the external pressure are normalized as

$$\overline{p_f} = \frac{p_f R}{G}, \quad \overline{P_1} = \frac{P_1 R}{G}, \quad \overline{P_2} = \frac{P_2 R}{G}. \tag{5.29}$$

The normalized pressure difference (defined as the suction pressure) by which the membrane is aspirated is

$$\overline{\Delta P} = \overline{P_2} - \overline{P_1}. \tag{5.30}$$

In general, as shown in Figure 5.1(b), at low suction pressure, the membrane aspirated does not form contact with the micropipette wall. As the suction pressure increases to a certain value, the contact with the micropipette wall is achieved as shown in Figure 5.1(c). Figure 5.3 to Figure 5.12 represent the response of the membrane at an initial inflation of $r_0 = 2R$. The aspirated membrane for micropipette radius $\bar{\rho} = 0.52$ and different suction pressures is shown in Figure 5.3. Figure 5.3(a) shows the state where the membrane is inflated, but not aspirated. Figure 5.3(b) illustrates the state where the membrane has no contact with the micropipette wall, and Figure 5.3(c-d) illustrates the state where the membrane is in contact with the micropipette wall. The correspond-

ing normalized suction pressures for Figure 5.3(b-d) are $\overline{\Delta P} = 0.871, 0.540$ and 0.103, and the normalized aspirated lengths are $\bar{L} = 1.01, 2.35$ and 6.76, respectively. Interestingly, these values indicate that, once contact with the micropipette wall is achieved, the suction pressure can decrease, while the aspirated length keeps increasing. In addition, our numerical results show 42.5%

a   b   c   d
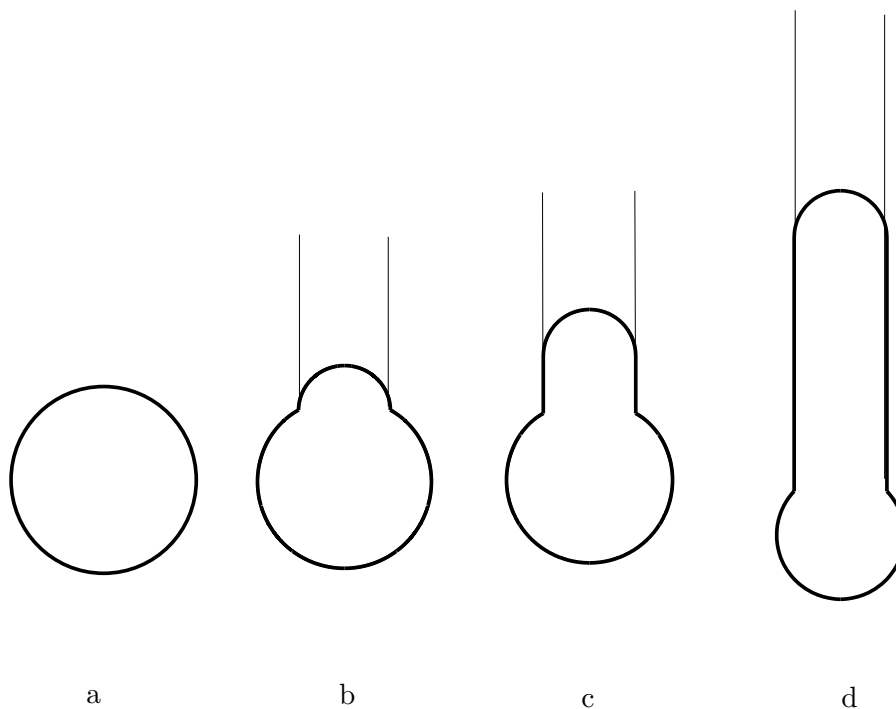
Figure 5.3: Configuration of the membrane when aspirated by a micropipette of radius $\bar{\rho} = 0.52$, (a) Referential state, $\overline{\Delta P} = 0.0$ (b) $\overline{\Delta P} = 0.872$ (c) $\overline{\Delta P} = 0.505$(d) $\overline{\Delta P} = 0.103$.

of the membrane is inside the micropipette in Figure 5.3(c) and 92.5% is inside the micropipette in Figure 5.3(d). Out of the part of the membrane inside the micropipette, 62.1% (in Figure 5.3(c)) and 96.4% (in Figure 5.3(d)) are in contact with the micropipette wall. Clearly, as deformation increases, portion of the membrane inside the micropipette that is in contact with the micropipette wall increases, while the portion of the membrane inside the micropipette that is not in contact decreases. This phenomenon occurs because stretches about the pole are larger compared with the stretches in the part which is in contact

with the micropipette wall. This point will be demonstrated later.

To study the large deformation of the membrane, its aspiration into micropipettes of various sizes is investigated. The micropipette size is in the range of $(0.20r_0 - r_0)$, where r_0 is the radius of the inflated membrane. Figure 5.4 shows the deformed configuration of the membrane when aspirated by micropipettes of different radii at the same suction pressure $\overline{\Delta P} = 0.310$. It is observed that, at the same suction pressure, the aspirated length is larger in smaller micropipettes. Specifically, the aspirated lengths in the three mi-

a   b   c   d
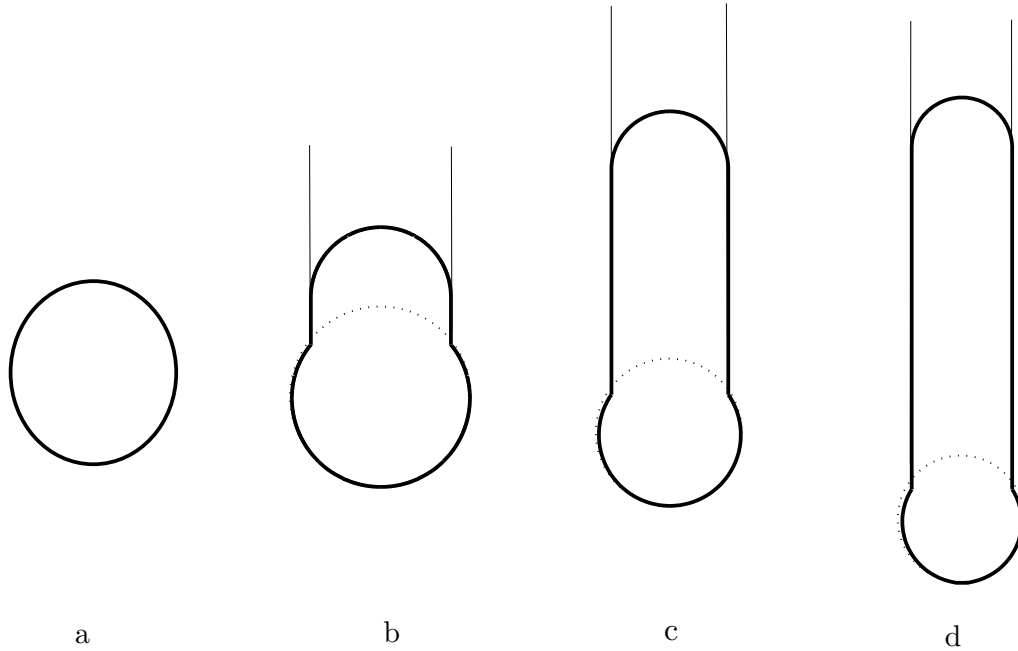
Figure 5.4: Configuration of the membrane when aspirated by micropipettes of different radii at the same $\overline{\Delta P} = 0.310$ (a) Referential state (b) $\bar{\rho} = 0.70$ (c)$\bar{\rho} = 0.58$ (d)$\bar{\rho} = 0.52$. The dotted curve represents sphere (with Delta P =0.0).

cropipette sizes $\bar{\rho} = 0.70, 0.58$ and 0.52 are $\bar{L} = 2.38, 5.68$ and 8.13, respectively. For fixed $\overline{\Delta P}$, 45.9% of the membrane is inside the micropipette in Figure 5.4(b), 87.35% is inside the micropipette in Figure 5.4(c) and 98.1% is inside the micropipette in Figure 5.4(d). The portions 40.41% (in Figure 5.4(b)), 90.09% (in Figure 5.4(c)) and 96.58% (in Figure 5.4(d)), respec-

tively, are in contact with the micropipette wall. This demonstrate that, at the same $\overline{\Delta P}$, a larger portion of the membrane is in contact with the micropipette wall for smaller micropipettes. In [17], it is verified experimentally that the resistance to aspiration is small for large micropipette size and large for small micropipette size. To investigate this fact by our model, we consider different micropipettes sizes: $\bar{\rho} = 0.70, 0.58, 0.52$ and 0.45. The $\overline{\Delta P}$ require to initially aspirate an equal small portion of the membrane into the micropipette are determined to be 0.019 for $\bar{\rho} = 0.70$, 0.073 for $\bar{\rho} = 0.58$ and 0.143 for $\bar{\rho} = 0.52$. These pressure values indicate that the resistance to aspiration increases drastically as the micropipette size decreases. This is in agreement with experimental observations.

In a typical micropipette experiment, a suction pressure is applied and the aspirated length is measured. Figure 5.5 shows the relation predicted by our model between the normalized suction pressure and the ratio L/ρ for different micropipette sizes. Here, L/ρ is chosen to be the variable instead of $\bar{L}$, because the radius of the unstressed membrane R is not known in experiments. Let us first examine the curve corresponding to $\bar{\rho} = 0.45$. It can be seen that the suction pressure first increases with L/ρ at a steep slope until it reaches p, which is the pressure at which contact with the micropipette wall is initiated. As L/ρ further increases, $\overline{\Delta P}$ continues to increase, but with a much smaller slope. At certain L/ρ, $\overline{\Delta P}$ reaches its maximum value p', after which $\overline{\Delta P}$ decreases with further aspiration. p' represents the threshold point after which the suction pressure decreases in the micropipette, while the aspiration length continues to increase. We refer to this phenomenon as "liquid-like" behavior of the membrane. Specifically, our model is based on displacement control, in which the part of the membrane aspirated is specified and the corresponding suction pressure is computed. However, in experiments, load control is typically used to aspirate the membrane. The suction pressure is

116
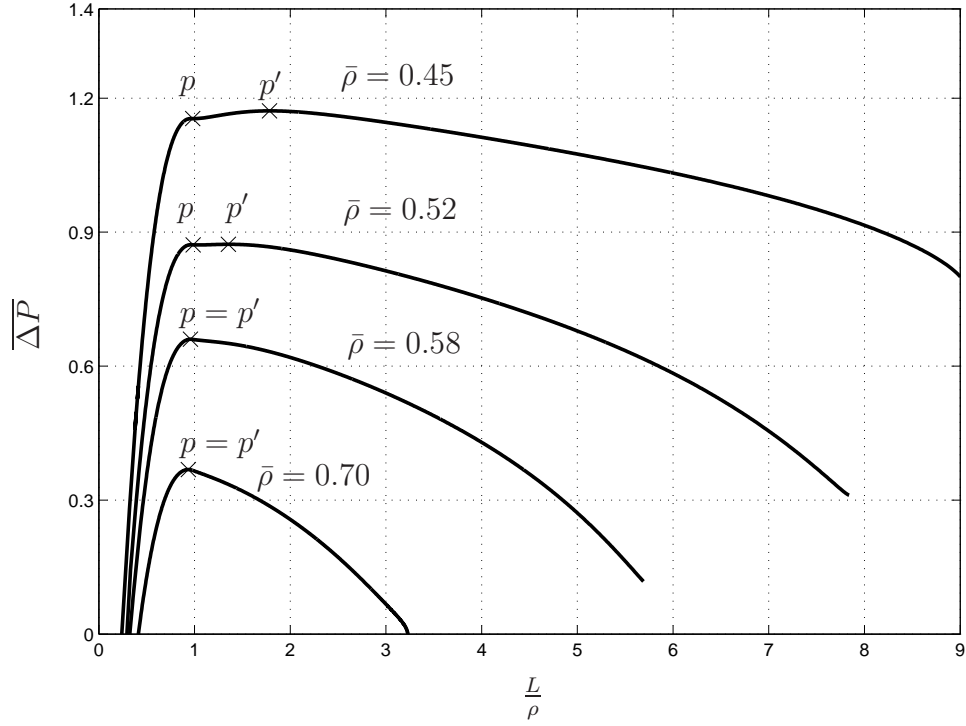
Figure 5.5: Normalized suction pressure vs. aspiration length L normalized by micropipette radius ρ for various micropipette sizes $\bar{\rho} = \{0.70, 0.58, 0.52, 0.45\}$.

gradually increased and the corresponding deformation of the membrane is measured at each $\overline{\Delta P}$. Because the suction pressure decreases with L/ρ after the threshold value, it is expected that in a load control test the membrane will spontaneously "flow" into the micropipette once ΔP exceeds p'. The additional three curves in Figure 5.5 demonstrate how $\overline{\Delta P}$ varies with L/ρ for different micropipette sizes. All the curves demonstrate similar characteristics, namely, that there is a branch with positive slope and one with negative slope. However, for the cases where $\bar{\rho} \geq 0.58$, it has been found that p and p' collapse into a single point. For these micropipette sizes, once the membrane forms contact with the micropipette wall, the "liquid-like" behavior is expected in a load control test. It is interesting to point out that such "liquid-like" behavior is an experimentally observed phenomenon [1, 13, 15, 17]. Such phenomenon cannot be predicted by the solid-like models where the aspiration length increases when the suction pressure increases [16]. However, it can be captured

with the present model.

If $\overline{\Delta P}$ is slowly reduced after reaching p', there are two possible outcomes: (1) the membrane undergoes further deformation, which corresponds to moving along the curves in Figure 5.5 from p' to the right or (2) the aspiration process is reversed and the membrane gradually retreats from the micropipette,
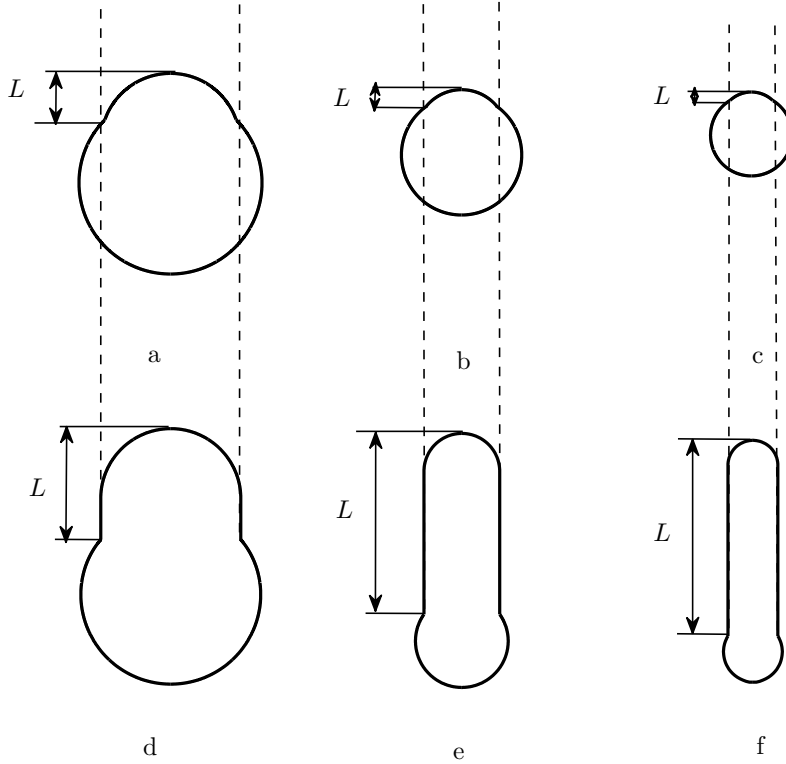

Figure 5.6: Configurations of the membrane aspirated by micropipette of different radii at the same $\overline{\Delta P} = 0.311$ (a)-(c) $\bar{\rho} = 0.70$, $\bar{\rho} = 0.58$ and $\bar{\rho} = 0.52$, respectively, in the situation where the membrane is not in contact with the micropipette wall;(d)-(f) $\bar{\rho} = 0.70$, $\bar{\rho} = 0.58$ and $\bar{\rho} = 0.52$, respectively, in the situation where the membrane is in contact with the micropipette wall.

which corresponds to moving along the curves in Figure 5.5 from p' to the left. Figure 5.6(a-c) show the deformed configurations of the membrane for three micropipette sizes at the suction pressure of $\overline{\Delta P} = 0.311$, where the membrane is not in contact with the micropipette wall, and Figure 5.6(d-f) show the deformation at the same $\overline{\Delta P}$, but in this case the membrane is in

contact with the micropipette wall. It is observed that, in the former case (i.e., before reaching the maximum pressure), the aspirated length is greater for larger micropipette sizes: $\bar{L} = 0.706, 0.474$ and 0.401 for $\bar{\rho} = 0.70, 0.58$ and 0.52, respectively. In contrast, after the threshold point, the aspirated length is greater in smaller micropipette sizes: $\bar{L} = 1.59, 4.79$ and 7.79 for $\bar{\rho} = 0.70, 0.58$ and 0.52, respectively.
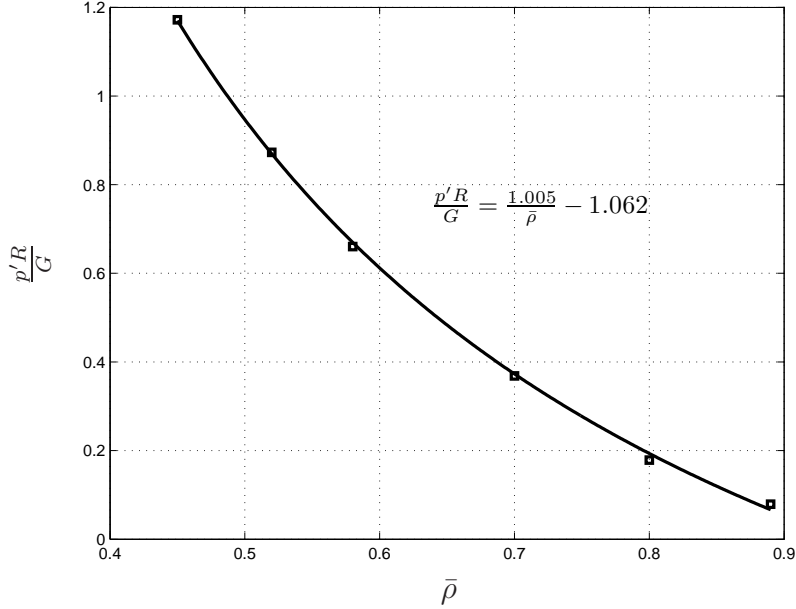
Figure 5.7: Normalized threshold pressure vs. normalized micropipette radii.

The maximum pressure as a function of the micropipette radius is plotted in Figure 5.7, where the squares represent the p' values obtained from our numerical calculations. It is clear from Figure 5.7 that the maximum pressure p' increases as micropipette size decreases. This relation looks very similar to the experimental data reported in [1,17]. In fact, the maximum pressure can be shown to be inversely proportional to the micropipette radius, as demonstrated by the curve fitting (solid line in Figure 5.7). This is in quantitative agreement with experimental findings [1, 17].

In the literature, the micropipette aspiration data have been used to extract the stiffness and viscosity of the cortical layer [2, 16, 17]. The membrane in our

model has no bending stiffness; nevertheless, the results above demonstrate quantitatively good agreement with experimental observations. The membrane resistance to aspiration in this model results from the enclosed fluid. To illustrate this, in Figure 5.8, the fluid pressure p_f in the membrane is plotted as a function of the aspirated length. p_f is normalized by p_f^0, which is the initial pressure of the fluid prior to aspiration. The fluid pressure increases as the aspirated length increases. For fixed $\bar{L}$, the fluid pressure is larger for smaller micropipettes. Because the membrane in our model has no bending rigidity, its resistance to aspiration largely arises from the enclosed fluid. The larger p_f shown here for smaller micropipettes is consistent with the fact that it is more difficult to aspirate the membrane with smaller micropipette. This result also indicates that the experimentally observed resistance to aspiration may be largely attributed to the structural stiffness due to the enclosed fluid, rather than the bending stiffness of the surface. Therefore, special care should be exercised when interpreting the experimental data. In fact, as indicated by Taber [29, 30] in his work of fluid-filled spherical shell, bending is important if the deflection is less than 20 percent of the radius, whereas the membrane stress becomes significant for large deformations. If the spherical shell has a thin wall (radius to thickness ratio about 16), the bending stiffness can be completely neglected [31].

The normalized contact area with the micropipette wall vs. the normalized suction pressure is plotted in Figure 5.9. Here, the contact area A_c between the membrane and the micropipette wall is normalized by R^2. The arrows in the figure indicate how A_c and $\overline{\Delta P}$ change as the aspirated length in the micropipette increases. Clearly, when the aspirated length is small, A_c remains zero, independent of $\overline{\Delta P}$. This is the regime where the membrane does not have contact with the micropipette wall. After $\overline{\Delta P}$ reaches p, contact is initiated, A_c continues to increase for further aspiration, while ΔP may start

120
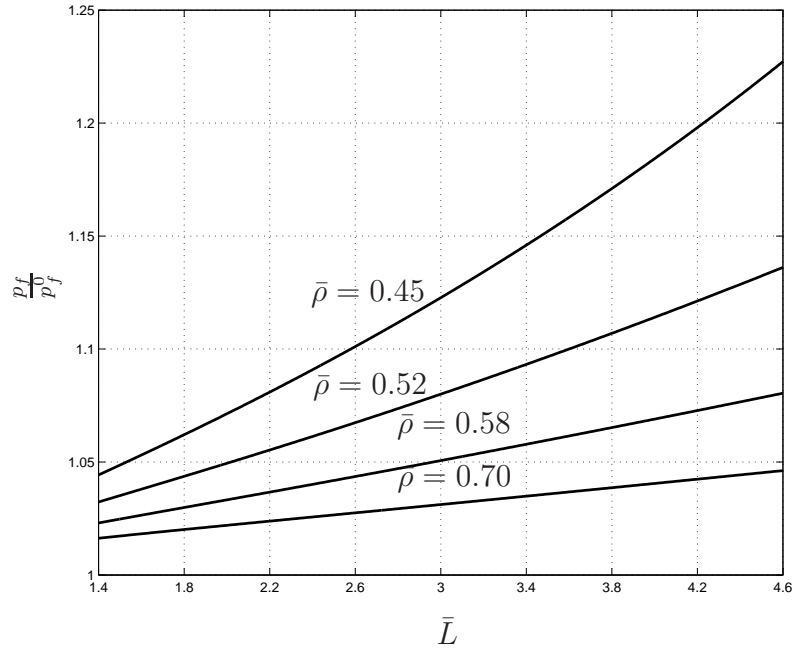
Figure 5.8: Normalized fluid pressure vs. normalized aspiration length for various micropipette sizes $\bar{\rho} = \{0.70, 0.58, 0.52, 0.45\}$.
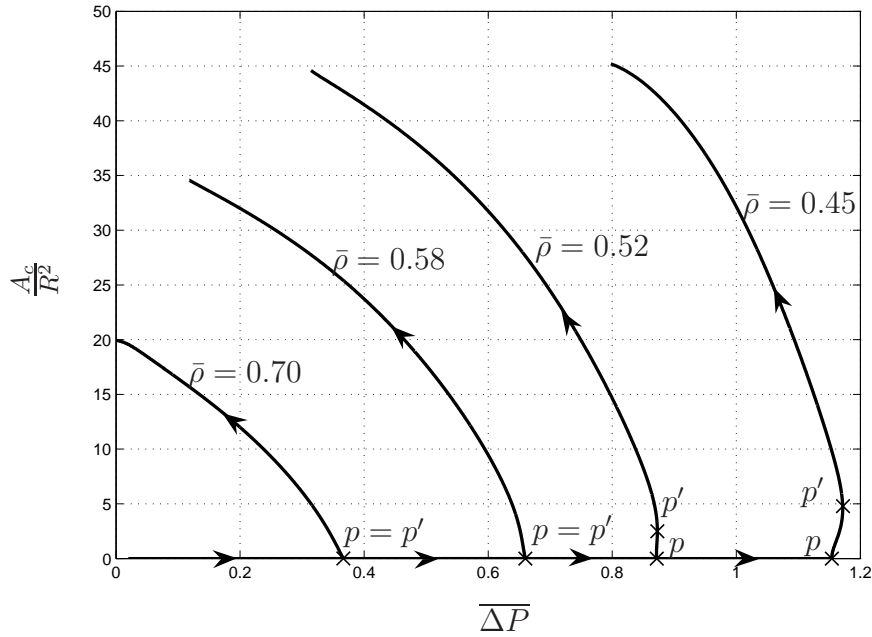
Figure 5.9: Normalized contact area between the membrane and the micropipette wall vs. normalized suction pressure for various micropipette sizes $\bar{\rho} = \{0.70, 0.58, 0.52, 0.45\}$.

decreasing (if $p' = p$) or increasing to p' and then decreasing. In Figure 5.9, the maximum contact area that can be achieved for $\bar{\rho} = 0.70$ is about $20R^2$

and the contact area for $\bar{\rho} = 0.45$ can exceed $45R^2$. Recalling that the surface area of the unstressed membrane is πR^2 and that of the inflated membrane is $4\pi R^2$ ($r_0 = 2R$), our results demonstrate significant areal dilation during aspiration, and such dilation appears to be much more pronounced in smaller micropipette sizes. It is recognized that such large dilation may not be possible physically. However, the maximum contact area that can be obtained depends on the initial inflation r_0 and the choice of $r_0 = 2R$ here is rather arbitrary. Nevertheless, the results here demonstrate the possibility of very large deformation, which is often seen experimentally [6,13–15,17]. In [17], the cell model is based on the assumption that the cell surface inside and outside of the micropipette is spherical. In [8], the deformed cell is assumed to be of cylindrical shape with a hemisphere at each end. In [15], the assumption is limited to the situation where the segment outside the micropipette is hemispherical. Unlike these models, our model does not make any geometrical assumptions and the actual deformed shape of the membrane is solved. Deviation from spherical shape is demonstrated in Figure 5.4, where dashed circles are drawn as a comparison. In [3], it is argued that neither the external nor the internal part is spherical. In [1], it is suggested that, in complex situations, there is deviation from the original spherical shape. It has also been shown experimentally that the external part is not spherical [15], especially at large deformations. These results are consistent with our model.

The assumption of a spherical surface also implies that the tension is uniform along the surface. This assumption was made in many papers [1,6,11,13–17]. Because of the invalidity of the spherical shape assumption in general, constant tension may not be a good assumption under certain loading conditions. In fact, our results show that variation in the tension exists on the surface. The principal stresses are plotted in Figure 5.10 for different micropipette sizes at the same aspiration length $\bar{L} = 2.0$. The suction pressure is different, being

0.329, 0.636 and 1.17 for $\bar{\rho} = 0.70, 0.58$ and 0.45, respectively. The principal stresses are normalized by w_i, where w_i is the magnitude of the initial principal stress in the inflated spherical membrane. In Figure 5.10, ϕ corresponds to the convected location on the reference membrane surface as shown in Figure 5.1. Before the kink, part of the membrane is inside the micropipette and beyond the kink, part of the membrane is outside the micropipette. Clearly, each of
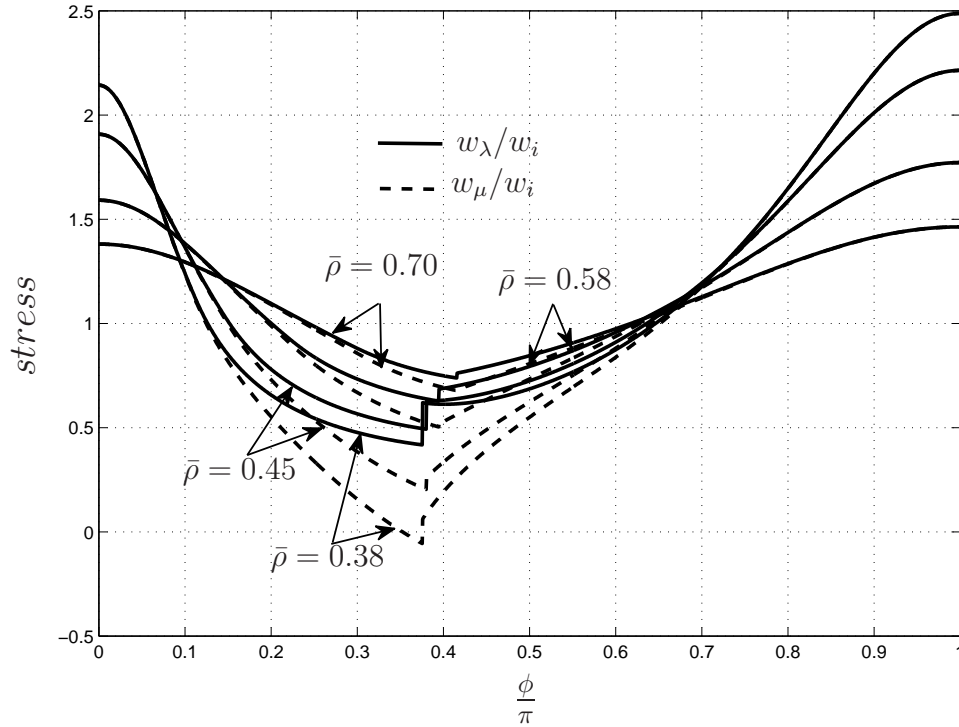
Figure 5.10: Distribution of normalized principal stresses in the membrane for various micropipette sizes $\bar{\rho} = \{0.70, 0.58, 0.45\}$.

the two principal stresses w_λ and w_μ varies with location along the surface. In addition, the principal stresses w_λ and w_μ are equal near the poles ($\phi = 0$ and π), but deviates in between, especially in the part of the membrane in contact with the micropipette wall. Such difference is more pronounced for smaller micropipette sizes. It is also observed from Figure 5.10 that for each $\bar{\rho}$, jumps in the principal stresses occur at the location of the kink where the membrane makes contact with the lower edge of the micropipette. This further confirms that the principal stresses are not only non-uniform, but also

discontinuous. It is interesting to see that for $\bar{\rho} = 0.38$, w_μ becomes negative around $\phi/\pi \approx 0.37$. Because the membrane presented in our model can only sustain tension, the negative w_μ obtained here will correspond to compression of the membrane and physically will cause its wrinkling. The wrinkling only occurs for sufficiently small micropipettes, in this case when $\bar{\rho} \leq 0.40$.
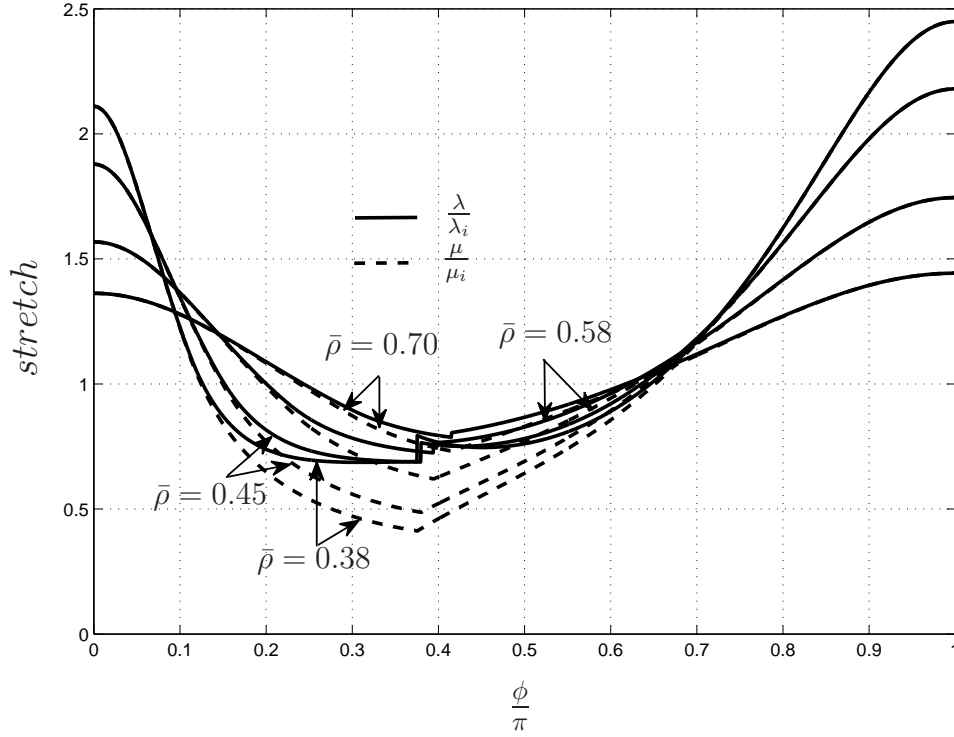
Figure 5.11: Distribution of normalized principal stretches in the membrane for various micropipette sizes $\bar{\rho} = \{0.70, 0.58, 0.45\}$.

The principal stretch distribution in the deformed membrane, normalized by the initial principal stretch λ_i, are plotted in Figure 5.11. The behavior is quite similar to what is shown in Figure 5.10 for the principal stresses, namely that the two principal stretches are equal at the poles and deviates around the contact region of the membrane with the micropipette wall, indicating the geometry of the deformed membrane is only close to being spherical near the poles. There also exists a jump in λ at the kink and it is more pronounced for small micropipette sizes. As shown in Figure 5.11, the principal stretches are greater at the poles, which is consistent with the earlier argument in the

explanation of Figure 5.3.
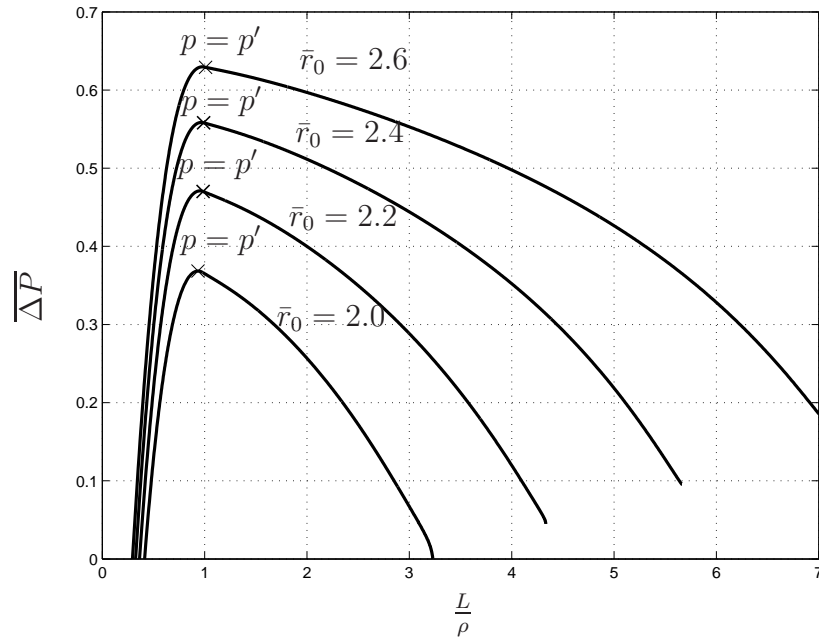
Figure 5.12: Normalized suction pressure vs. normalized aspiration length with micropipette size $\bar{\rho} = 0.70$ and different initial inflations $\bar{r}_0 = \{2.0, 2.2, 2.4, 2.6\}$.
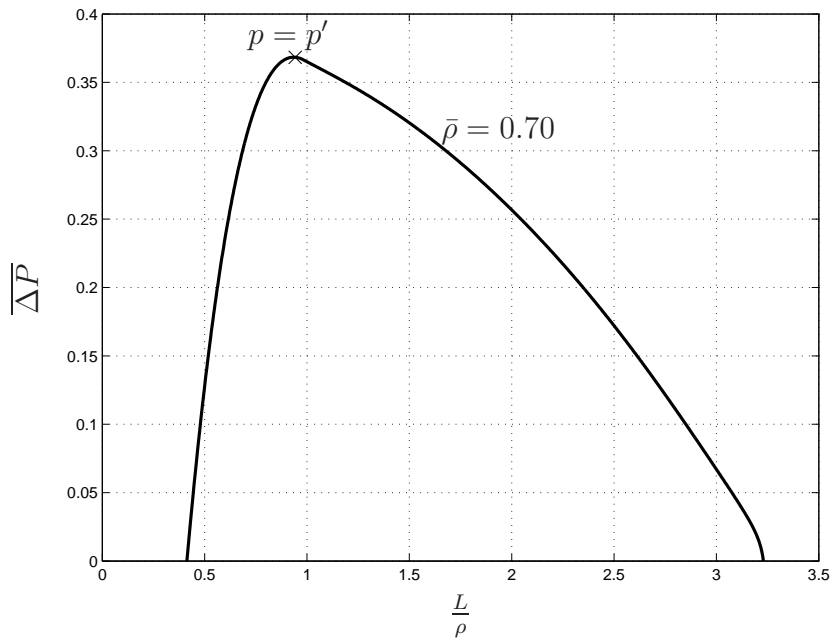
Figure 5.13: Normalized suction pressure vs. normalized aspiration length with micropipette size $\bar{\rho} = 0.70$ and different external pressures $\overline{P_2} = \{0.0, 0.5, 1.0, 1.5\}$. All curves collapse onto one another and, therefore, only a single curve is visible.

In the previous discussions, the initial inflation has been fixed at $r_0/R = 2$. Figure 5.12 presents the characteristic behavior of the membrane considering different inflation values $r_0/R = 2.0, 2.2, 2.4$ and 2.6. The suction pressure as a function of aspirated length is plotted at a constant micropipette radius $\rho = 1.41R$. For all values of r_0 considered here, the suction pressure increases until it reaches the maximum value p', which coincides with p, the pressure at which contact with the pipette wall is initiated. The suction pressure drops afterwards and the membrane exhibits "liquid-like" behavior. At the same $\frac{L}{\rho}$, a membrane with larger initial inflation requires a larger suction pressure, which is expected.

In the results presented above, P_1, the pressure inside the micropipette, is variable and P_2, the ambient pressure, is assigned to be zero. In Figure 5.13, the normalized suction pressure vs. the normalized aspiration length is plotted considering different ambient pressures $P_2 = 0.0, 0.5, 1.0$ and 1.5. Interestingly, all the curves collapse onto one another, indicating that the deformation of the membrane only depends on the pressure difference $\Delta P = P_2 - P_1$, but not on P_1 or P_2 individually. This is a direct result of the incompressibility of the enclosed fluid, but it is not apparent from the formulation of the BVP, where the quantity $P_2 - P_1$ cannot be clearly separated. Nevertheless, our numerical results confirmed this fact, which is also consistent with the experimental data [17], where L is reported as a function of the pressure difference ΔP.

5.5 Conclusions

Reliable models for the mechanics of cells are very important in the understanding of cell adhesion, flow of cells in vessels, arteries, veins and capillaries, where deformation of cells occurs. In this work, we use a continuum membrane model to characterize the mechanical response of a cell during micropipette

aspiration. This model assumes elastic material properties, but accounts for large deformation. No assumptions are made on the deformed shape of the cell. The membrane has no bending stiffness, but the enclosed fluid can greatly contribute to the structural stiffness. Based on this model, we identify two critical suction pressures p and p' during aspiration. As the suction pressure increases from zero, prior to reaching the suction pressure p, the membrane deforms, but it is not in contact with the micropipette wall. Between p and p', the membrane comes in contact with the micropipette wall. After reaching the maximum pressure value p', the aspiration length continues to increase, but, to maintain equilibrium, the suction pressure has to decrease. This predicts a "liquid-like" behavior during a load control test. The maximum pressure p' increases as the micropipette radius decreases or as initial inflation increases. During aspiration, non-uniform and even discontinuous principal stresses/stretches are obtained on the surface of the membrane. This indicates that the deformed membrane does not possess a spherical shape in general, especially when the deformation is large. Despite its simplicity, the model we presented here, captures some of the experimental results quite adequately. Specifically, it predicts larger resistance associated with smaller micropipette sizes. The relationship between aspiration pressure and aspirated length captures the "solid-like" response at small deformation and "liquid-like" response beyond the maximum pressure point, both observed in experiments. The maximum pressure is shown to be inversely proportional to the micropipette radius, which is also consistent with experimental data [17].

The present model is by no means a fully realistic representation of a cell under micropipette aspiration. There are clear limitations. The model does not involve any rate-dependent material properties and, therefore, will not be able to capture any time/rate-dependent behaviors observed in experiments. This can be done by extending the current model to include viscosity in the

membrane and in the enclosed fluid. The adhesion and the frictional contact of the membrane with the micropipette wall are not part of this study. It is observed that wrinkling may appear in the aspirated part of the membrane during large deformation, if very small micropipette sizes ($\bar{\rho} \leq 0.40$) are used. Experimentally, aspiration using very small micropipettes is not feasible because cell lysis will occur [1, 13]. Future research may model the cytoplasm as a viscous and compressible fluid. The non-linear membrane coupled with the cytoplasm model will shed more light on the cell's complex mechanical response.

Bibliography

[1] A. Yeung and E. Evans, "Cortical shell-liquid core model for passive flow of liquid-like spherical cells into micropipets," *Biophys. J.*, vol. 56, pp. 139–149, 1989.

[2] K. Sung, G. Schmid-Schonbein, R. Skalak, G. Schuessler, S. Usami, and S. Chien, "Influence of physiochemical factors on rheology of human neutrophils," *Biophys. J.*, vol. 39, pp. 101–106, 1982.

[3] M. Haider and F. Guilak, "An axisymmetric boundary integral model for assessing elastic cell properties in the micropipette aspiration contact problem," *ASME J. of Biomech. Eng.*, vol. 124, pp. 586–595, 2002.

[4] G. W. Schmid-Schonbein, K-L.P.Sung, and H. Tozeren, "Passive mechanical properties of human leukocytes," *Biophys. J.*, vol. 36, pp. 243–256, 1981.

[5] K. Sung, C. Dong, G. Schmid-Schonbein, S. Chien, and R. Skalak, "Leukocyte relaxatio properties," *Biophys. J.*, vol. 54, pp. 331–336, 1988.

[6] E. Evans and B. Kukan, "Passive material behavior of granulocyte based on large deformation and recovery after deformation tests," *Blood*, vol. 64, pp. 1028–1035, 1984.

[7] M. Sato, D. Theret, L. Wheeler, N. Ohshima, and R. Nerem, "Application of the micropipette technique to the measurement of cultured porcine

aortic endothelial cell viscoelastic properties," *ASME J. Biomech. Eng.*, vol. 112, pp. 263–268, 1990.

[8] W. Jones, H. Ting-Beall, G. Lee, S. Kelley, R. Hochmuth, and F. Guilak, "Alterations in the young's modulus and volumetric properties of chondrocytes isolated from normal and osteoarthritic human cartilage," *J. of Biomech.*, vol. 32, pp. 119–127, 1999.

[9] R. Hochmuth, "Micropipette aspiration of living cells," *J. of Biomech.*, vol. 33, pp. 15–22, 2000.

[10] J. L. Drury and M. Dembo, "Aspiration of human neutrophils: Effects of shear thinning and cortical dissipation," *Biophys. J.*, vol. 81, pp. 3166–3177, 2001.

[11] R. Rand, "Mechanical properties of the red cell membrane ii. viscoelatic breakdown of the membrane," *Biophys. J.*, vol. 4, pp. 303–316, 1964.

[12] D. Theret, M. Levesque, M.Sato, R. Nerem, and L. Wheeler, "The application of a homogeneous half-space model in the analysis of endothelial cell micropipette measurements," *ASME J. of Biomech. Eng.*, vol. 110, pp. 190–199, 1988.

[13] R. Tran-Son-Tay, D. Needham, A.yeung, and R. Hochmuth, "Time-dependent recovery of passive neutrophils after large deformation," *Biophys. J.*, vol. 60, pp. 856–866, 1991.

[14] C. Dong, R. Skalak, K. Sung, G. Scmid-Schonbein, and S. Chien, "Passive deformation analysis of human leukocytes," *ASME J. of Biomech. Eng*, vol. 110, pp. 27–36, 1988.

[15] D. Needham and R. Hochmuth, "Rapid flow of passive neutrophils into a 4 μm pipet and measurement of cytoplasmic viscosity," *ASME J. of Biomech. Eng.*, vol. 112, pp. 269–276, 1990.

[16] R. Hochmuth, H. Ting-Beall, B. Beaty, D. Needham, and R. Tran-Son-Tay, "Viscosity of passive human neutrophils undergoing small deformations," *Biophys. J.*, vol. 64, pp. 1596–1601, 1993.

[17] E. Evan and A.Yeung, "Apparent viscosity and cortical tension of blood granulocytes determined by micropipet aspiration," *Biophys. J.*, vol. 56, pp. 151–160, 1989.

[18] D. Bottino, "Modeling viscoelastic networks and cell deformation in the context of the immersed boundary method," *J. of Computational Phys.*, vol. 147, pp. 86–113, 1998.

[19] Y. Lin and L. Freund, "Forced detachment of a vesicle in adhesive contact with a substrate," *Int. J. Sol. Struct.*, vol. 44, pp. 1927–1938, 2007.

[20] Q. H. Cheng, P. Liu, H. J. Gao, and Y. Zhang, "A computational modeling for micropipette-manipulated cell detachment from a substrate mediated by receptor-ligand binding," *J. Mech. Physi. Sol*, vol. 57, pp. 205–220, 2009.

[21] V. Heinrich and C. Ounkomol, "Force versus axial deflection of pipette-aspirated closed membranes," *Biophys. J.*, vol. 93, pp. 363–372, 2007.

[22] D. Simson, F. Ziemann, M. Strigl, and R. Merkel, "Micropipet-based pico force tansducer: In depth analysis and experimental verification," *Biophys. J.*, vol. 74, pp. 2080–2088, 1998.

[23] L. Sun, Q. Cheng, H. Gao, and Y. Zhang, "A nonlinear characteristic regime of biomembrane force probe," *J. of Biomech.*, vol. 44, pp. 662–668, 2011.

[24] L. B. Freund, "The stiffness of a biomembrane force probe vesicle," *Math. Mech. Solids.*, vol. 14, pp. 148–160, 2009.

[25] U. Bagge, R. Skalak, and R. Attefors, "Granulocyte rheology. experimental studies in an in vitro micro-flow system," *Adv Microcirc*, vol. 7, pp. 29–48, 1977.

[26] M. Coughlin and D. Stamenovic, "A tensegrity structure with buckling compression elements: Application to cell mechanics," *J. Appl. Mech.*, vol. 64, pp. 480–486, 1997.

[27] B. Nadler, "On the contact of a spherical membrane enclosing a fluid with rigid parallel planes," *Int. J. Non-Linear Mech.*, vol. 45, pp. 294–300, 2010.

[28] T. Sohail and B. Nadler, "On the contact of an inflated spherical membrane-fluid structure with a rgid conical indenter," *Acta Mech.*, vol. 202, pp. 1–16, 2011.

[29] L. A. Taber, "Compression of fluid-filled spherical shells by rigid indenters," *J. Appl. Mech.*, vol. 50, pp. 717–722, 1983.

[30] L. A. Taber, "Large deflection of a fluid-filled spherical shell under a point load," *J. Appl. Mech.*, vol. 49, pp. 121–128, 1982.

[31] K. K. Liu, D. R. Williams, and B. J. Briscoe, "Compressive deformation of a single microcapsule," *Phys. Rev. E.*, vol. 54, pp. 6673–6680, 1996.

Chapter 6

Adhesive contact of a fluid-filled membrane driven by electrostatic forces[1]

6.1 Introduction

Adhesion between two objects arises from the molecular interactions between them [1–3]. These interactions can be categorized into (1) non-specific, such as electrostatic, van der Waals, steric and hydrophobic interactions [1, 2, 4–7], or (2) specific, such as receptor-ligand bonds and hydrogen bonding [2, 4–6, 8–12]. Specific interactions are strong, but short-ranged, while the non-specific interactions are relatively weak, but long ranged [2, 4–6]. Adhesion plays an important role in biology, for example, cell deformation, cell movement, growth and cell-tissue interaction [12, 13, 20–22] and contributes substantially to many industrial applications, for example, electrophotography [14–17], powder technology [18, 19], biotechnology, semiconductor and pharmaceutical industries [23, 24].

Cell adhesion has recently become an intensive area of research because of its significance in many biological, physiological and pathological processes [4, 8, 9, 12, 13]. Also, widely studied is the adhesion of vesicles, which are more

---

[1]A version of this chapter is in press for publication. Touqeer Sohail, Tian Tang and Ben Nadler., Int. J. Solids Struct., 2013.

simple than cells, as they have no cytoskeleton or nucleus effects [4, 25]. They are often used as primitive models to determine important insights in cell adhesion [1]. In experiments, many techniques have been used to investigate the specific and non-specific adhesion of cells and vesicles during their attachment with other cells, vesicles or substrates [2, 4, 5], including atomic force microscopy [26], dynamic force spectroscopy [11], magnetic tweezers [13], optical interferometry [27], traction force microscopy [28], optical traps [29], centrifugation [30], hydrodynamic shear [31], micropipette aspiration [8,9,11,12], optical microscope [3, 11] and impedance spectroscopy [25]. Evans *et al.* [32] measured the adhesion between red blood cells using micropipette aspiration by monitoring the reduction of the aspirated length in the pipette during adhesion. Similarly, Prechtel *et al.* [11] used micropipette aspiration to study the detachment of a vesicle from a substrate. They observed that the detachment force depended on the loading rate which could be well described by a power law relation with exponent of 0.4. In the work of Reinhart-King *et al.* [33], endothelial cells were plated on flexible polyacrylamide gels, the spreading rate and changes in the cell shape were examined, and the traction force exerted by the endothelial cells on the polyacrylamide substrate was measured by traction force microscopy. It was observed that the rate of spreading of the endothelial cells increased with the ligand density on the substrate [33]. Aside from the experimental explorations, many theoretical studies have been conducted to model cell/vesicle adhesion [1–6, 8–11, 13, 20–22, 25, 34–42]. There are two key elements in each of these studies. The first is a mechanics model that captures the bulk mechanical response of the cell/vesicle and the second is an interfacial model for adhesion. To reduce the difficulties of modeling the non-homogeneous and non-isotropic nature of cells, many assumptions have been introduced in the bulk mechanics models of cells, common examples including constant surface area [2], constant volume [4, 5, 20, 36], constant tension along

the surface [37,38], small deformation [11,21,22] and negligible bending [21,22]. These assumptions are not without limitations, but have greatly simplified the analysis on cell deformation. The necessity of considering bending depends upon the extent of deformation. Taber showed that bending dominated if the deflection of a fluid-filled rubber shell was less than 20 percent of its radius [39, 40] and, at large deformation, membrane stretching became more significant [39]. Joshi *et al.* [21, 22], by using a thin shell model for a spherical cell structure and determining its deformation in response to external electric fields, observed that the bending moments were small and could be neglected for simple analysis. For elastic polymer capsules which have thin membrane structures, it was observed that bending effects were negligible compared to stretching [43]. In general, it has been found that, if a spherical microcapsule has a radius that is more than 16 times its thickness, the bending moment can usually be neglected [41], while for larger thickness, the bending effect has to be included [42]. The geometrical assumption of small deformation is quite common, but it has also been emphasized that geometrical nonlinearity can play a significant role during large deformation [5]. Cell/vesicle adhesion also depends strongly upon the interfacial adhesive behaviors. Many interfacial models have been introduced, for example, within thermodynamic framework [1,5], via chemical reaction kinetics [2, 4–6, 11, 12, 35, 44] and probabilistic kinetics [5], as well as through cohesive zone models [4, 5, 8, 9]. These models are typically based on one of two approaches. The first uses an energy approach and the formation of contact area causes reduction in the system's free energy [1–3,8,9,12,13]. The second models the interacting forces explicitly and "binders" on the interface keep the surfaces in contact [2, 4, 5, 8, 9, 13, 34]. Through out the literature, it has become evident that non-specific and specific forces have different interaction relation and strength that contribute towards adhesion [5]. Therefore, it is appropriate to model them separately [5]. As

one of the non-specific forces, electrostatic interaction is a long-ranged interaction that contributes to cell/vesicle adhesion. In particular, charge groups exist over the surfaces of cells and vesicles, and they can interact with one another as well as with other charged entities. Seyfert *et al.* [45] used the flat plate streaming potential method to test the adhesion of leucocytes to microscope glass slides coated with various polycations. It was observed that the cell adhesion could be modified by altering the surface conditions and the interaction forces, including the electrostatic forces [45]. Modeling and understanding electrostatic interaction is therefore of interest to the study of cell/vesicle adhesion and its modulation.

Many experimental and theoretical efforts have been devoted to the study of particle-particle and particle-substrate adhesion driven by electrostatic forces. Experimentally, different methods, for example, atomic force microscopy, centrifugal detachment and microelectrode detachment field methods have been used to investigate the electrostatic adhesive force between particles and substrates [14–18]. Through these studies, many factors that affect the electrostatic force were determined, including particle size, particle's total charge and its distribution, particle shape and surface roughnesses of the particle and the substrate [14,15,17]. On the theoretical front, several works addressed the adhesion between a charged particle and a conductive plane [14–16,18,45]. The particle was usually assumed to be spherical with a uniformly distributed surface charge [16–18]. These charges were controllable and could be increased by applying an electric field [17,18]. The electrostatic force between the particle and the substrate was then calculated via different methods such as the image charge model, charge patch model and dumbbell model [14, 18, 46]. It has also been a common practice to replace the uniform surface charges around a spherical particle by a point charge at the center of particle [14,16] in order to facilitate the force calculation. The image charge model [17] and Matsuyama

model [47] always underestimate the electrostatic force because these models do not consider the strong contribution from the local charges in the vicinity of the contact area [14]. For instance, the electrostatic adhesion of a conductive plane with a spherical particle that has a uniform, but discrete, distribution of charges was studied by Schien [16] and Czarnecki *et al.* [46]. It was predicted analytically that the electrostatic force acting on the few charges on the particle in close proximity with the conductive plane was comparable to the electrostatic force acting on a single point charge located at the center of the sphere [46]. Although the various models mentioned above acknowledged significant electrostatic interaction and predicted its contribution to adhesion, all these models assumed that the electrostatic interaction was between rigid particles and substrates, that is, no deformation resulted from the interaction.

For compliant solids subjected to electrostatic forces, however, such treatment is not appropriate. For example, experiments on vesicles with different internal and external conductivity were used to determine the electromechanical behavior of vesicles [25]. These experiments suggested that the deformation of the vesicles strongly depended upon the magnitude and frequency of the applied electrostatic field, as well as the conductivity of the media. Theoretically, Bryant *et al.* [20] modeled a cell in suspension under a uniform electric field. The interaction of the electric field with the induced charges on the cell membrane caused its deformation and the electrical and mechanical stresses in the cell membrane were analyzed [20]. The external electric field was assumed not to be influenced by the deformation and possible charge redistribution of the cell. That is, the electrostatics is decoupled from the deformation. In [37], the cell membrane was modeled as an insulating layer with univalent cations exterior to the layer and univalent anions in the interior of the layer. The presence of surface charges on the outer and inner surfaces of the cell produces surface stresses on the cell membrane due to the attraction of counterions. The

137

resulting pressure drop across the membrane sets a limit on the hydrostatic pressure drop that the membrane can sustain without buckling. This analysis focused on addressing the equilibrium of the membrane in presence of electrostatic forces, while the actual deformation of the membrane required from the equilibrium condition was not calculated. In [38], Lopez *et al.* studied the shape of human erythrocyte by assuming constant tension in the cell membrane and considering its deformation caused by both the electrostatic forces due to the charges on the cell surface and the hydrostatic pressure difference across the cell. The proposed model coupled electrostatics with deformation and predicted an equilibrium shape that was similar to the observed shape of erythrocytes [38]. While these previous studies have shed light on the mechanics of flexible particles under electrostatic forces, it remains unclear how electrostatic interaction can contribute to adhesion of such flexible particles to other entities and how adhesion may be affected by surrounding media such as an electrolyte solution, the environment in which cells reside.

In this work, we study an interesting adhesion problem driven by electrostatic forces, while invoking possible large nonlinear deformation and strong coupling between deformation and electrostatic forces. In particular, we study a charged flexible particle that adheres to an oppositely charged substrate via electrostatic attraction. The particle is a spherical membrane filled with incompressible fluid. The membrane cannot sustain bending, but is extensible and can undergo large nonlinear deformation. Such a model has been used to represent the deformation of vesicles [4], but electrostatic interaction was absent from that work. The particle is located in an electrolytic environment with certain salt concentration. We assume that the presence of electrostatic field gives rise only to electrostatic forces acting on the membrane associated with the charge's attraction and repulsion. Material response, in the form of polarization, to an electric field [48–50] is neglected. Uniformly dis-

tributed charges are initially introduced on the surface of the membrane. In the absence of other charged entities, the electrostatic repulsion between these surface charges results in spherical symmetry in the shape of the particle. As this particle is brought to the vicinity of an oppositely charged substrate, the electrostatic attraction between the charges on the membrane and the charges on the substrate deforms the particle, leading to its formation of contact with the substrate. Such deformation is resisted by the stresses in the membrane, as well as by the fluid inside the membrane. In addition, the deformation results in a new charge distribution on the membrane surface, which in turn affects the electrostatic interaction between the surface charges and between the particle and the substrate. That is, the deformation of the particle and the electrostatic interaction are strictly coupled. Through this work, we demonstrate how the electrostatic force induced adhesion is affected by the properties of the particle and the electrolyte solution. Our results will be useful for modulating particle-substrate adhesion by controlling the electrostatic interaction [10].

The present chapter is organized as follows. The formulation of the electrostatic force, the equilibrium equation, the geometry of the nonlinear membrane and its constitutive relation are presented in Section 6.2. The numerical procedure used to obtain the deformed configuration is explained in Section 6.3. The results and discussion are provided in Section 6.4, while conclusions are given in Section 6.5.

6.2   Formulation

The system under consideration is shown in Figure 6.1. It consists of a spherical membrane with an initially uniform distribution of positive charges on its surface. The radius of the membrane is R in the reference unstressed configuration κ. We will consider R to be in the micron/submicron range, because
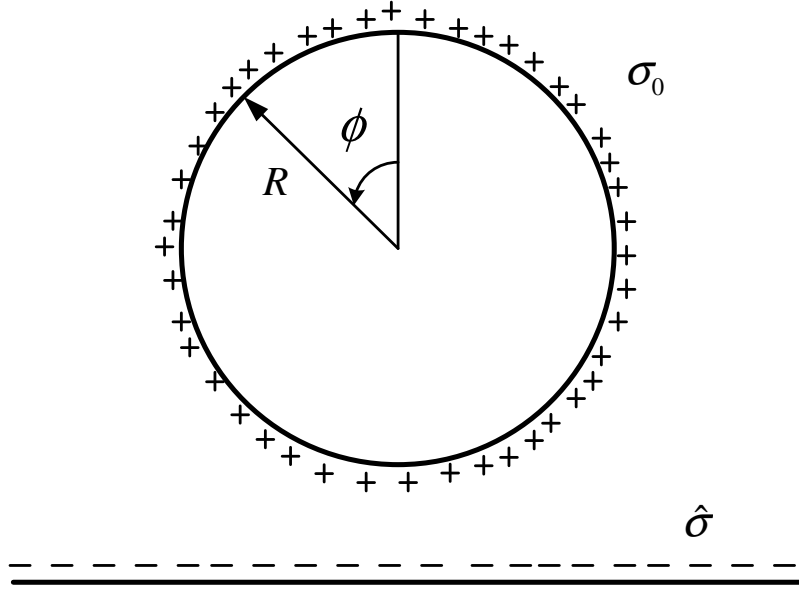
Figure 6.1: System under consideration in this work. It consists of a spherical membrane of radius R in the reference configuration and a nearby rigid flat substrate. σ_0 is the surface charge density on the membrane and ϕ represents the location of the charges in the meridional direction, both measured in the reference configuration. $\hat{\sigma}$ is the surface charge density of the substrate. Both the membrane and the substrate are embedded in an electrolytic environment, and the membrane is filled with incompressible fluid.

this problem is motivated by the adhesion of small particles, where surface forces dominate. The location of charges on the membrane is represented by angle ϕ in the reference configuration. The total charge on the membrane is $Q = \sigma_0(4\pi R^2)$, where σ_0 is the uniform referential charge density as shown in Figure 6.1. The membrane is assumed to have no bending rigidity, but it is stretchable and can sustain large nonlinear deformation. The inside of the membrane is filled with incompressible fluid. A rigid flat substrate with a uniform distribution of negative charges $\hat{\sigma}$ is located near the membrane as shown in Figure 6.1. Note that the choice of $\sigma_0 > 0$ and $\hat{\sigma} < 0$ is rather arbitrary, and all calculations in this work remain the same as long as $\sigma_0\hat{\sigma} < 0$. Both the membrane and the substrate are located in an electrolytic environment. It is assumed that the electrolyte solution both inside and outside of the membrane

is identical having the same Debye length. The Debye length is an important quantity to describe an electrolyte solution. It is inversely proportional to the square root of the ionic concentration in the solution [51] and is a characteristic length that corresponds to the distance from a charged entity at which the electric potential decays to approximately $1/e$ of its value at the charged entity [52], e here being the base of the natural logarithm.

The loading process considered in this work is described as follows. Firstly, the membrane of radius R in the reference configuration is inflated by the incompressible fluid to a radius of r_0. Under the fluid pressure and the electrostatic repulsion among the charges on the surface, the membrane maintains its spherical shape. Afterward, the substrate is brought to the proximity of the inflated membrane. The electrostatic attraction between the charges on the membrane and those on the substrate tends to deform the membrane and cause its adhesive contact with the substrate. The deformation of the membrane is resisted by the electrostatic repulsion among the charges on the membrane as well as by the fluid enclosed by the membrane. This results in an equilibrium deformation of the membrane. It is clear that the entire loading process as described above is axisymmetric, therefore, the deformation possesses axisymmetry. Due to steric effects and van der Waal repulsive interactions at short range (although not to be explicitly modeled in this work), in the deformed configuration, a non-zero gap will be formed in the contact area between the membrane and the substrate, and, therefore, neutralization of charges on the membrane and on the substrate will not be considered. The objective of this study is to model the coupling between the electrostatic interactions and the deformation of the membrane, and to predict the equilibrium deformation of the membrane, the adhesive contact and adhesive force, and how they depend on physical parameters governing the problem. To obtain the equilibrium deformation of the membrane, a system of equations was developed that de-

scribes the geometry and constitutive behavior of the membrane, as well as the force balance involving the electrostatic interactions. The formulation is presented below.

Due to axisymmetric deformation, we can completely describe the shape of the membrane using the curve from point O to point A as shown in Figure 6.2(a). To calculate the electrostatic traction at an arbitrary surface ele-
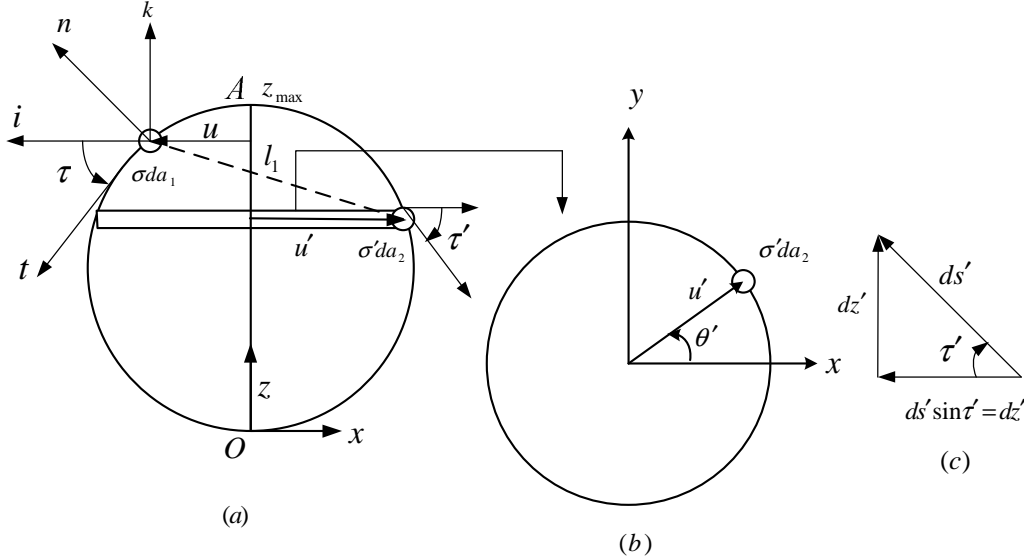
Figure 6.2: (a) Calculation of electrostatic traction on an arbitrary element da_1 of the membrane due to another surface element da_2 on the membrane. σ is the charge density in da_1, σ' is the charge density in da_2 and l_1 is the distance between da_1 and da_2. z defines the vertical position of points on the membrane from the lower pole O. (b) Cross-sectional view of the membrane showing the location of the surface element da_2. x and y are the coordinates of points on the membrane in the circumferential direction. θ' and u' show the radial and angular position of da_2, respectively. (c) An infinitesimal element ds' in the meridional direction, τ' is the angle between the curved membrane and the horizontal x-axis.

ment da_1 on the membrane, we start with the electric potential Φ, which, for both inside and outside of the membrane, is assumed to be governed by the Debye-Huckel (D-H) equation [53]

$$\nabla^2 \Phi = k^2 \Phi, \tag{6.1}$$

142

where k is the inverse Debye length defined as

$$k = \left(\frac{q^2}{\epsilon_0 \epsilon k_B T} \sum_i z_i n_{i\infty} \right)^{1/2}.$$ (6.2)

In equation (6.2), q is the unsigned charge of an electron, ϵ_0 is the free space permittivity, ϵ is the dielectric constant of the solution, k_B is the Boltzmann constant, T is the temperature, z_i is the valence of the ith type of ions in the solution and $n_{i\infty}$ is the bulk number concentration of the ith type of ions. The D-H equation is the linear version of the Poisson-Boltzmann (P-B) equation governing the electrolyte [53]. The linear form of equation (6.1) not only allows analytical solution for Φ in many situations, but it also allows for the use of linear superposition, which is adopted in this work. Specifically, consider an arbitrary surface element da_2 on the membrane (see Figure 6.2(a)). If the local charge density in da_2 is σ', then the total charge in da_2 is $\sigma' da_2$. Treating it as a point charge gives the potential Φ in the electrolyte due to this point charge [53]:

$$\Phi = \frac{(\sigma' da_2) e^{-kl}}{4\pi \epsilon_0 \epsilon l},$$ (6.3)

where l is the distance from this surface charge element. Denoting the local charge density in da_1 as σ, and considering σ and σ' are separated by l_1, the electrostatic force from the charge $\sigma' da_2$ on the charge σda_1 is calculated by taking the gradient of the potential Φ in (6.3) with respect to l, evaluating it at $l = l_1$, and multiplying it by $-\sigma da_1$. This gives the electrostatic force from $\sigma' da_2$ on the surface elements da_1 as

$$\boldsymbol{F}_{21} = \frac{(\sigma da_1)(\sigma' da_2)}{4\pi \epsilon_0 \epsilon}(1 + kl_1) \left(\frac{e^{-kl_1}}{l_1^2} \right) \mathbf{e}_{l_1},$$ (6.4)

where $\mathbf{e}_{l_1}$ is the unit vector pointing from da_2 to da_1. Now, by considering the force between σda_1 and all other surface elements on the membrane and on

143

the substrate, and using linear superposition, the total force on σda_1 can be calculated. It should be noted that, as the membrane deforms, the local charge distribution on the membrane varies, which also modifies the electrostatic forces. Specifically, the local charge density in da_1 can be written as $\sigma = \frac{\sigma_0}{\lambda\mu}$, where λ and μ are the principal stretches at da_1 and $\lambda\mu$ represents the local areal dilation. Similar calculation can be performed for any other surface element on the membrane. Due to axisymmetry, σ and σ' are functions of z only and do not depend on x or y shown in Figure 6.2. Because the substrate is considered to be rigid and it does not deform, its charge density $\hat{\sigma}$ is fixed throughout the calculation.

To perform the superposition, we first express the area element da_2 in terms of the coordinates defined in Figure 6.2. The cross-section of the membrane in the circumferential direction is shown in Figure 6.2(b). θ' is the circumferential location of da_2 and u' is the radial distance of da_2 from the z-axis as shown in Figure 6.2(a). The surface element da_2 can be written as $da_2 = u'(z')d\theta'ds'$. ds' is the length of an infinitesimal element along the membrane in the meridional direction shown in Figure 6.2(c) and can be written as $ds' = \frac{dz'}{\sin\tau'}$, where τ' is the angle between the tangent on the membrane and the horizontal x-axis. The distance l_1 between da_1 and da_2 can be written as

$$l_1 = \sqrt{(x - u'(z')\cos\theta')^2 + (y - u'(z')\sin\theta')^2 + (z - z')^2}, \qquad (6.5)$$

where $\{x, y, z\}$ are the coordinates of surface element da_1, $\{u'(z')\cos\theta', u'(z')\sin\theta', z'\}$ are the coordinates of da_2. The total electrostatic traction acting on da_1 due to all surface charge elements on the membrane can then be calculated through the following integration

$$\frac{\boldsymbol{F}_m(z)}{da_1} = \frac{\sigma(z)}{4\pi\epsilon_0\epsilon} \int_0^{z_{max}} \int_0^{2\pi} \left[(\sigma'(z'))\frac{u'(z')}{\sin\tau'}\right](1+kl_1(\theta', z', z))\left(\frac{e^{-kl_1(\theta', z', z)}}{[l_1(\theta', z', z)]^2}\right)\mathbf{e}_{l_1(\theta', z', z)}d\theta' dz',$$
$$(6.6)$$

144

where $\mathbf{e}_{l_1(\theta',z',z)}$ is the unit vector pointing towards da_1 from any other area element on the membrane. In (6.6), the dependence of l_1 on x and y has been omitted for simpler notation, because axisymmetry permits us to use the curve from O to A (i.e., a given set of x and y) to describe the membrane deformation.

Since σ and σ' in (6.6) are of the same sign, $\mathbf{F}_m(z)$ represents a repulsive force, which provides resistance to the deformation of the membrane. On the contrary, the electrostatic attractive forces between the surface charges on the membrane and the substrate tend to deform the membrane. The electrostatic forces on da_1 from the substrate can be calculated as follows. In Figure 6.3(a), H represents the non-zero gap between the substrate and the lower pole of the membrane and l_2 is the distance between da_1 and an arbitrary surface element da_3 on the substrate. In Figure 6.3(b), R_1 is the distance from the axis of the membrane to da_3 and φ represents the location of da_3 in the circumferential direction. The expression for the total electrostatic traction acting on da_1 due to all surface charge elements on the substrate is

$$\frac{\mathbf{F}_s(z)}{da_1} = \frac{\sigma(z)}{4\pi\epsilon_0\epsilon} \int_0^\infty \int_0^{2\pi} [(\hat{\sigma}R_1)](1+kl_2(\varphi,R_1,z)) \left(\frac{e^{-kl_2(\varphi,R_1,z)}}{[l_2(\varphi,R_1,z)]^2} \right) \mathbf{e}_{l_2(\varphi,R_1,z)} d\varphi dR_1,$$
(6.7)

where $\mathbf{e}_{l_2(\varphi,R_1)}$ is the unit vector pointing towards da_1 from any arbitrary element on the substrate and l_2 can be written in terms of (φ,R_1) as

$$l_2 = \sqrt{(x-R_1\cos\varphi)^2 + (y-R_1\sin\varphi)^2 + (z+H)^2}.$$
(6.8)

Here, $\{R_1\cos\varphi, R_2\sin\varphi, -H\}$ are the coordinates of da_3 on the substrate with respect to O shown in Figure 6.3.

Summing (6.6) and (6.7), after substituting (6.5) into equation (6.6) and (6.8) into equation (6.7), gives the total electrostatic traction $\mathbf{f}_e$ at the element

145
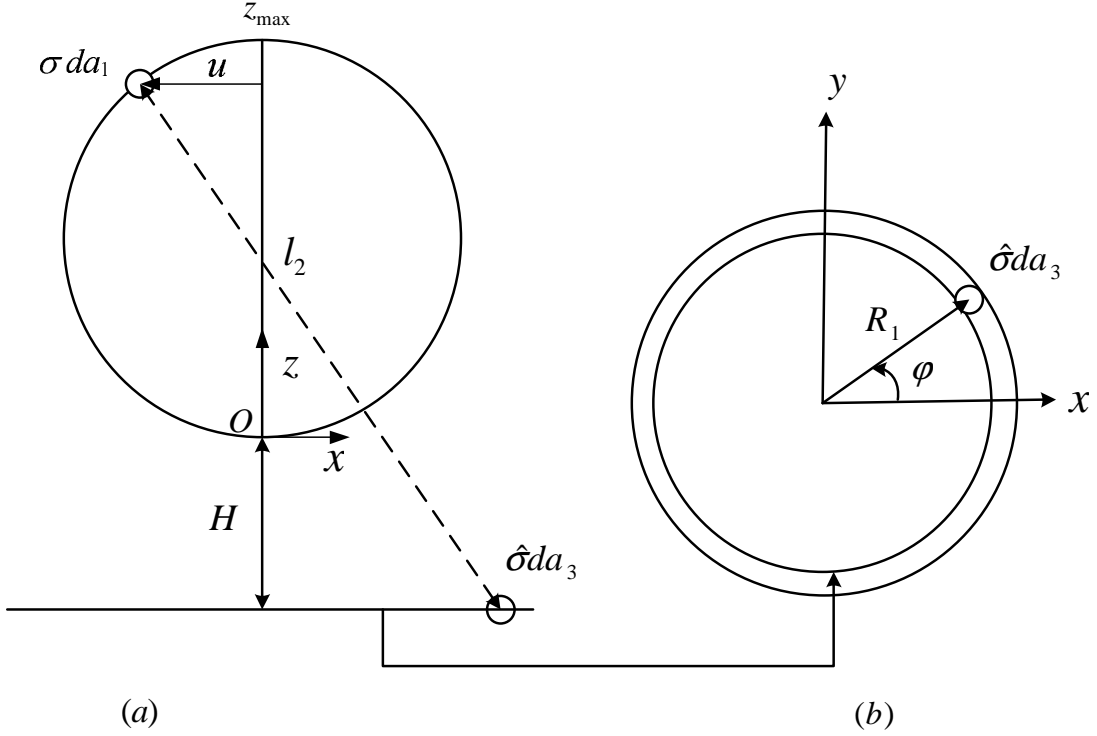
Figure 6.3: Calculation of electrostatic traction on an arbitrary element da_1 of the membrane due to the flat substrate. (a) l_2 is the distance between da_1 and an arbitrary surface element da_3 on the substrate and H is the vertical distance from the substrate to the lower pole O on the membrane (b) x-y plane view of the substrate, where φ and R_1 are the radial and angular position of da_3, respectively.

da_1 on the membrane, which can be expressed as

$$\mathbf{f}_e = \mathbf{f}_{et} + \mathbf{f}_{en}, \tag{6.9}$$

where $\mathbf{f}_{et} = f_{et}\mathbf{t}$ and $\mathbf{f}_{en} = f_{en}\mathbf{n}$ are the electrostatic tractions in the tangential $\mathbf{t}$ and the normal $\mathbf{n}$ directions, respectively, as shown in Figure 6.2(a). Because of axisymmetry, the electrostatic traction does not have any circumferential component. $\mathbf{t}$ and $\mathbf{n}$ are defined in the deformed configuration and can be expressed in terms of the cylindrical basis $\{\mathbf{i}, \mathbf{j}, \mathbf{k}\}$ as

$$\mathbf{t} = \cos\tau\mathbf{i} - \sin\tau\mathbf{k}, \quad \mathbf{n} = \sin\tau\mathbf{i} + \cos\tau\mathbf{k}, \tag{6.10}$$

146

where $\mathbf{i}$ and $\mathbf{k}$ are depicted in Figure 6.2(a) and $\mathbf{j}$ is orthogonal to both $\mathbf{i}$ and $\mathbf{k}$. Since the choice of da_1 is arbitrary, the equilibrium equation of the membrane can be written as

$$\text{Div}\,\mathbf{P} + J(\mathbf{f}_f + \mathbf{f}_e) = \mathbf{0}, \tag{6.11}$$

where Div is the divergence operator on the reference configuration κ, $\mathbf{P}$ is the first Piola-Kirchhoff stress tensor, J is the areal dilation, $\mathbf{f}_f$ is the traction due to the fluid inside the membrane and $\mathbf{f}_e$ is the traction due to the electrostatic interaction. The traction exerted by the fluid is normal to the membrane $\mathbf{f}_f = p_f \mathbf{n}$, where p_f is the fluid pressure. The gravity of the fluid can be neglected because of the small dimension considered here. Therefore, equilibrium of the fluid requires uniform pressure inside the membrane. The first Piola-Kirchhoff stress tensor $\mathbf{P}$ of a hyperelastic material is equal to the gradient of the strain energy function with respect to the deformation gradient $\mathbf{F}$ of the membrane, which can be expressed as [54–56]

$$\mathbf{F} = \frac{\frac{dr}{d\phi}\mathbf{e}_r + r\frac{d\psi}{d\phi}\mathbf{e}_\psi}{R} \otimes \mathbf{E}_\phi + \frac{r\sin\psi}{R\sin\phi}\mathbf{e}_\theta \otimes \mathbf{E}_\theta, \tag{6.12}$$

where $\{\psi, \theta\}$ are the spherical coordinates in the deformed configuration γ. ψ represents the angular position of surface elements in the meridional direction and θ represents the angular position in the circumferential direction. $\{\mathbf{E}_\phi(\phi,\theta), \mathbf{E}_\theta(\theta), \mathbf{E}_R(\phi,\theta)\}$ and $\{\mathbf{e}_\psi(\psi,\theta), \mathbf{e}_\theta(\theta), \mathbf{e}_r(\psi,\theta)\}$ are the orthonormal basis for the spherical coordinates in κ and γ, respectively. After substitution of the first Piola-Kirchhoff stress tensor and the traction (due to both electrostatics and fluid) into (6.11), the equilibrium equation can be conveniently expressed as the following set of first order ODEs

$$\frac{d\lambda}{d\phi} = \frac{(w_\mu - \lambda w_{\lambda\mu})\cos\tau - (w_\lambda - \mu w_{\lambda\mu})\cos\phi}{w_{\lambda\lambda}\sin\phi} - \frac{\lambda\mu R f_{et}}{w_{\lambda\lambda}}, \tag{6.13}$$

$$\frac{d\tau}{d\phi} = \frac{\lambda\mu R(p_f + f_{en})}{w_\lambda} - \frac{w_\mu \sin\tau}{w_\lambda \sin\phi},\tag{6.14}$$

where $w(\lambda, \mu)$ is the isotropic strain energy function of the membrane, $w_\lambda = \frac{\partial w}{\partial \lambda}$, $w_\mu = \frac{\partial w}{\partial \mu}$ and $w_{\lambda\mu} = \frac{\partial w}{\partial \lambda\mu}$. The stretch μ in equations (6.13) and (6.14) is given by

$$\mu = \frac{u}{R\sin\phi},\tag{6.15}$$

and the ODE for u is given by

$$\frac{du}{d\phi} = \lambda R \cos\tau.\tag{6.16}$$

The detailed derivation of the equations (6.13)-(6.16) can be obtained by extending our previous work [54–56] to include the electrostatic traction. A word of caution for equation (6.14) is that in its derivation from equation (6.11), the pressure from the substrate upon the formation of contact has not been considered. Considering the contact pressure, equation (6.14) needs to be slightly modified, which will be explained below.

Due to the electrostatic attraction, a finite contact region is formed between the membrane and the substrate. Therefore, the membrane surface can be separated into two domains: (1) the free not in contact region and (2) the contact region. The transition between these two regions occurs at $\phi = \phi_c$. The free region of the membrane is between $0 \le \phi \le \phi_c$ and the contact region is in between $\phi_c \le \phi \le \pi$. The radius of contact between the membrane and the substrate is denoted as a. For each of the two domains, the governing equations and boundary conditions (BCs) are explained below.

In the free region of the membrane surface, the three first order ODEs (6.13), (6.14) and (6.16) are to be solved with the following BCs

$$u(0) = 0, \quad \tau(0) = 0, \quad u(\phi = \phi_c^-) = a, \quad \tau(\phi = \phi_c) = \pi.\tag{6.17}$$

The first two equations correspond to zero horizontal displacement and zero slope at the upper pole ($\phi = 0$; point A as shown in Figure 6.2(a)). The last two equations correspond to conditions at the edge of the contact zone ($\phi = \phi_c^-$), including the horizontal distance from the axis of the membrane being equal to the contact radius a, and the continuity of tangent angle τ in the absence of a concentrated force. At first glance, we have three first order ODEs and four BCs. But, it should be noted that both ϕ_c, and a, are not known a priori and should also be solved. This requires that one more BC be prescribed, which is the continuity of the stretch λ at ϕ_c

$$\lim_{\phi \to \phi_c^+} \lambda = \lim_{\phi \to \phi_c^-} \lambda. \tag{6.18}$$

For the contact region of the membrane, $\frac{d\tau}{d\phi} = 0$; therefore, equation (6.14) is not required. The governing equations required are (6.13) and (6.16), and the BCs of this region are

$$u(\phi = \phi_c^+) = a, \quad u(\phi = \pi) = 0. \tag{6.19}$$

The first equation corresponds to the horizontal distance being the contact radius a at ($\phi = \phi_c^+$) and the second equation requires the horizontal distance at the lower pole of the membrane ($\phi = \pi$; point O as shown in Figure 6.2(a)) to be zero, that is, the membrane is a closed axisymmetric surface. Once u is solved, μ can be determined from (6.15) and the principal stresses can be evaluated using (2.27). Finally, p_f is also an unknown to be found. To determine p_f, the condition to be satisfied is

$$\frac{V}{V_0} = 1, \tag{6.20}$$

which corresponds to the incompressibility of the fluid inside the membrane.

Here, $V_0 = \frac{4}{3}\pi r_0^3$ is the initial volume of the inflated spherical membrane and V is the volume of the fluid enclosed by the membrane after deformation and is calculated as

$$V = \pi \int_0^{z_{max}} u^2 dz. \tag{6.21}$$

It should be pointed out that in the contact zone, there is another source of loading, which is the contact pressure p_c from the substrate on the membrane and it is repulsive. This contact pressure may arise from steric or van der Waals repulsion when the surfaces are sufficiently close, and it modifies equation (6.14) to

$$\frac{d\tau}{d\phi} = \frac{\lambda\mu R(p_f + f_{en} - p_c)}{w_\lambda} - \frac{w_\mu \sin\tau}{w_\lambda \sin\phi}, \tag{6.22}$$

which is further reduced to

$$p_c = p_f + f_{en}, \tag{6.23}$$

as the membrane is flat in the contact zone, i.e., $\tau = \pi$ and $\frac{d\tau}{d\phi} = 0$. Since the BVP defined above completely determines the equilibrium deformation of the membrane, the fluid pressure p_f and the normal electrostatic traction $\mathbf{f}_{en}$, equation (6.23) serves to determine the distribution of the contact pressure p_c in the contact zone. To describe the nonlinear material behavior of the membrane, we make use of the constitutive relation for the Neo-Hookean type, which has the following strain energy function in terms of the principal stretches:

$$w(\lambda, \mu) = \frac{G}{2}\left(\lambda^2 + \mu^2 + (\lambda\mu)^{-2} - 3\right), \tag{6.24}$$

where G is the material constant. After the initial inflation, the fluid pressure inside the spherical membrane can be calculated as

$$p_f^0 = \frac{2G}{r_0}\left(1 - \left(\frac{R}{r_0}\right)^6\right). \tag{6.25}$$

150

6.3   Numerical Algorithm

In the numerical calculation, given initial uniform charge density on the membrane, charge density on the substrate, Debye length, material constant, radii of the membrane in its unstressed and inflated states, and gap between the membrane and the substrate, we determine the deformation of the membrane, the contact area and the adhesive force on the membrane. Since the deformation and the electrostatic forces are strongly coupled, the solution is obtained through an iterative numerical scheme as explained below.

Considering axisymmetric deformation, the membrane is discretized into n elements with spacing $\Delta\phi$ for $0 \leqslant \phi \leqslant \pi$. At each node $j = 1...n$, the electrostatic traction is calculated and the deformation is obtained by solving the BVP defined in Section 6.2. The shooting method is used to reduce the BVP to an initial value problem. Specifically, the membrane has two regions, the free region and the region in contact with the substrate. The initial guess values for λ_0 (λ_0 being the stretch at $\phi = 0$), p_f and ϕ_c are used to integrate the ODEs identified in Section 6.2, and the conditions $\tau(\phi_c) = \pi$, $u(\pi) = 0$ and $V/V_0 = 1$ are used to adjust the λ_0, p_f and ϕ_c values. Contact area a is also computed as part of the solution. The Euler's explicit method is used to integrate the governing equations. At this point, it is important to note that the electrostatic tractions on the membrane f_{et} and f_{en}, which appear in the equilibrium equations (6.13) and (6.14), are calculated from equations (6.6) and (6.7), and they clearly depend on the deformation of the membrane. That is, the final equilibrium configuration of the membrane should be such that the electrostatic tractions are consistent with the deformation. To obtain such a self-consistent deformation, we use the following iterative numerical scheme. We start with the spherical configuration of the membrane with a radius of r_0. The charge distribution on the membrane under this configuration is still uniform and the traction at any arbitrary position on the membrane can be calculated by

performing the integrations in equations (6.6) and (6.7). The calculated f_{et} and f_{en} are then substituted into the equilibrium equations (6.13) and (6.14) to obtain the deformation under such tractions. Next, the newly obtained deformation is applied to equations (6.6) and (6.7) to recalculate the tractions f_{et} and f_{en}, which are then used to calculate the deformation again. This iteration continues until the deformation and the electrostatic traction calculated from it are consistent in that the guess value for $\{\lambda_0, p_f, \phi_c\}$ at the $(N+1)^{th}$ iteration step is sufficiently close to that at the Nth iteration step. Such numerical scheme is applied to every set of parameters $\{\sigma_0, \hat{\sigma}, r_0, G, R, k, H\}$ and the dependence of the deformation and adhesive force on these parameters is presented in the section below.

6.4 Results and Discussion

In this section, we present numerical results to investigate the influence of parameters such as the Debye length, inflation and substrate charge density on the deformation of the membrane and on the adhesive electrostatic forces. At each equilibrium configuration, the distribution of charges on the deformed membrane, the adhesive contact area between the membrane and the substrate, the fluid pressure inside the membrane and the principal stresses/stretches on the membrane are studied in detail and discussed below.

To facilitate the discussion and reduce the number of independent parameters, a normalization of the BVP described in Section 6.2 can be performed using the following definitions:

$$\bar{a} = \frac{a}{R}, \quad \bar{r}_0 = \frac{r_0}{R}, \quad \bar{H} = \frac{H}{R}, \quad \bar{k} = kR, \quad \bar{p}_f = \frac{p_f R}{G}, \quad \bar{\sigma} = \frac{\sigma}{\sigma_0}, \quad \bar{\hat{\sigma}} = \frac{\hat{\sigma}}{\sigma_0}, \quad \bar{w} = \frac{w}{G},$$

$$(6.26)$$

where $\bar{a}$, $\bar{r}_0$ and $\bar{H}$ are, respectively, the contact radius, inflated radius and vertical distance between the membrane and the substrate normalized by the

referential radius of the membrane, $\bar{k}$ is the normalized inverse Debye length, $\bar{p}_f$ is the normalized fluid pressure inside the membrane, $\bar{\sigma}$ and $\bar{\hat{\sigma}}$ are, respectively, the local charge density on the membrane and the substrate charge density normalized by the referential charge density σ_0 on the membrane, and $\bar{w}$ is the normalized strain energy function. In addition, unless otherwise specified, all lengths are normalized by the referential radius of the membrane R. The normalized BVP is given in the Appendix, which reveals five dimensionless governing parameters: $\bar{H}$, $\frac{\sigma_0^2 R}{4\pi\epsilon_0\epsilon G}$, $\bar{k}$, $\bar{\hat{\sigma}}$, and $\bar{r}_0$. To get an estimate of the range of the parameters used in this work, consider a spherical membrane with a referential radius of 1 micron. The non-zero gap between the membrane and the substrate in the contact zone due to van der Waals repulsion is on the order of a few angstroms to one nanometer; hence $\bar{H}$ is chosen to be 0.001 throughout the calculation (simulations were also done for smaller $\bar{H}$ and the results showed similar characteristics). The dimensionless parameters $\frac{\sigma_0^2 R}{4\pi\epsilon_0\epsilon G}$ will also be fixed in the calculation. Specifically, σ_0 is chosen to be $0.022\ C/m^2$, close to the experimentally measured charge density on human erythrocytes [57]. Considering the solution to be aqueous, the dielectric constant ϵ is set to be 80. The estimation of the material constant G requires more consideration. In particular, because the membrane is a two-dimensional mechanics model, G has the dimension of force per unit length. That is, it differs from the elastic modulus E of a solid by a length scale. This length scale would be the thickness of the membrane if it is viewed as a three-dimensional material. In fact, the strain energy function as given in equation (6.24) implies that the material is incompressible and the principle stretch in the direction perpendicular to the membrane surface is $(\lambda\mu)^{-1}$. Denoting this length scale as L, G can be approximated by EL. Considering the elastic modulus of a soft solid with $E \sim 100$ MPa and the thickness L to be on the order of $10\ nm$ [58], G can be estimated to be $1\ N/m$. The resulting value of $\frac{\sigma_0^2 R}{4\pi\epsilon_0\epsilon G}$ from these estimations is

0.05, which will be applied to all calculations below. The other three governing parameters $\bar{k}$, $\bar{r}_0$ and $\bar{\hat{\sigma}}$ will be varied in the discussion. Since the Debye length of an electrolyte is typically in the range of $1nm$ to $100nm$ [59], the normalized parameter $\bar{k}$ is in the range of 10 to 1,000. We have used several values of $\bar{k}$ in this range to study the effect of Debye length, i.e., the effect of salt concentration on the membrane deformation. A range of normalized charge density $\bar{\hat{\sigma}}$ on the substrate from 0.1 to 60 is used in the calculation to study how it influences the adhesion. Finally, the effect of inflation r_0 is also investigated by varying $\bar{r}_0$ from 1.2 to 2.0.

First, we demonstrate the fundamental characteristic of the membrane deformation under the electrostatic force. Figure 6.4 presents the deformed equilibrium configuration of the membrane at an initial inflation of $\bar{r}_0 = 1.2$, Debye length $\bar{k} = 100$ and different substrate densities $\bar{\hat{\sigma}} = \{0.1, 30, 60\}$. As expected, the increase in $\bar{\hat{\sigma}}$ causes increase in the electrostatic attraction between the membrane and the substrate, which results in larger deformation of the membrane, larger contact area and smaller height of the membrane. The increase in total electrostatic force F due to the increase in the substrate charge density is shown in Figure 6.5(a), where the normalized force $\bar{F}$ is defined by $\bar{F} = \frac{F}{GR}$. From equation (6.7), the electrostatic attraction between the membrane and the substrate should be directly proportional to the surface charge density on the substrate. If the electrostatic interaction is decoupled from the deformation, then a linear relation will be expected. The observed nonlinear behavior shown in Figure 6.5(a) arises from the coupling between deformation and electrostatic force. Higher $\bar{\hat{\sigma}}$ results in larger deformation and, overall, closer separation between the charges on the membrane and the charges on the substrate. This causes the faster increase of $\bar{F}$ with $\bar{\hat{\sigma}}$ seen in Figure 6.5(a), as the substrate charge density increases. Such nonlinear relation, however, becomes insignificant once $\bar{\hat{\sigma}}$ reaches 48, after which the relation between $\bar{F}$

154
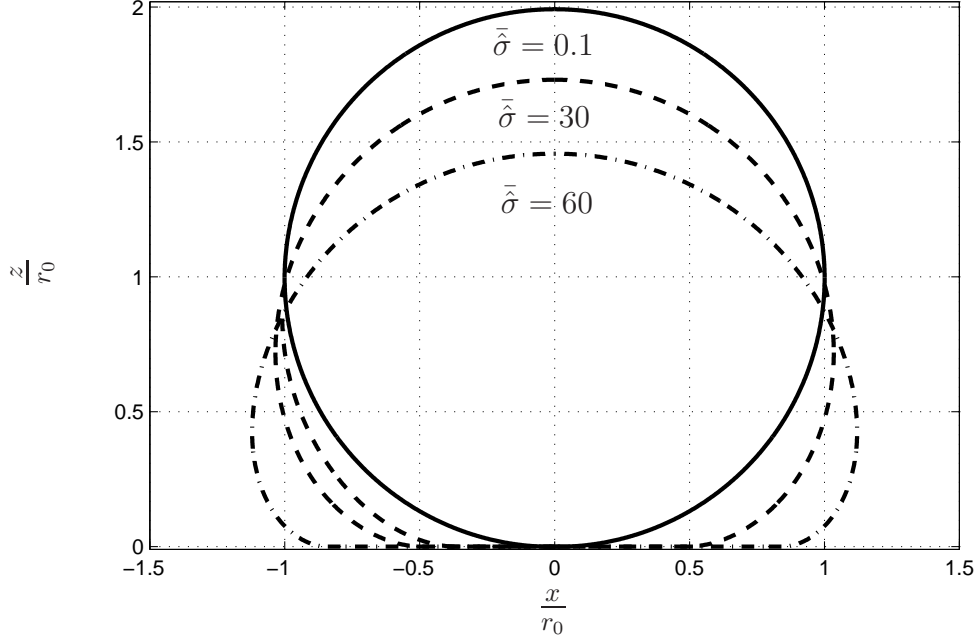
Figure 6.4: Deformed equilibrium configuration of the membrane at an inflation of $\bar{r}_0 = 1.2$, Debye length $\bar{k} = 100$ and several different substrate density $\bar{\hat{\sigma}}$ (0.1 for solid line, 30 for dash line and 60 for dash and dotted line).

and $\bar{\hat{\sigma}}$ becomes almost linear again. This implies that the coupling between the electrostatic interaction and the deformation is not strong for very large deformations. This can be further confirmed by examining the relation between the electrostatic force and the contact radius, as shown in Figure 6.5(b). It can be seen from this figure that the normalized contact radius $\bar{a}$ first increases gradually with the increase of electrostatic force, indicating steadily increasing contact between the membrane and the substrate. However, once $\bar{a}$ reaches 0.39, there is a rapid increase in $\bar{F}$ without significant changes in $\bar{a}$. Specifically, when $\bar{F}$ changes from 2.66×10^5 to 8.89×10^5 (234.13% increase), $\bar{a}$ only varies from 0.39 to 0.46 (18.56% increase). This demonstrates that once a considerable contact area has been formed, a significant increase in the electrostatic force is required to expand the contact area and to further deform the membrane. Therefore, in this regime, the influence of deformation on $\bar{F}$ becomes weaker and $\bar{F}$ is mainly affected by changes in $\bar{\hat{\sigma}}$.
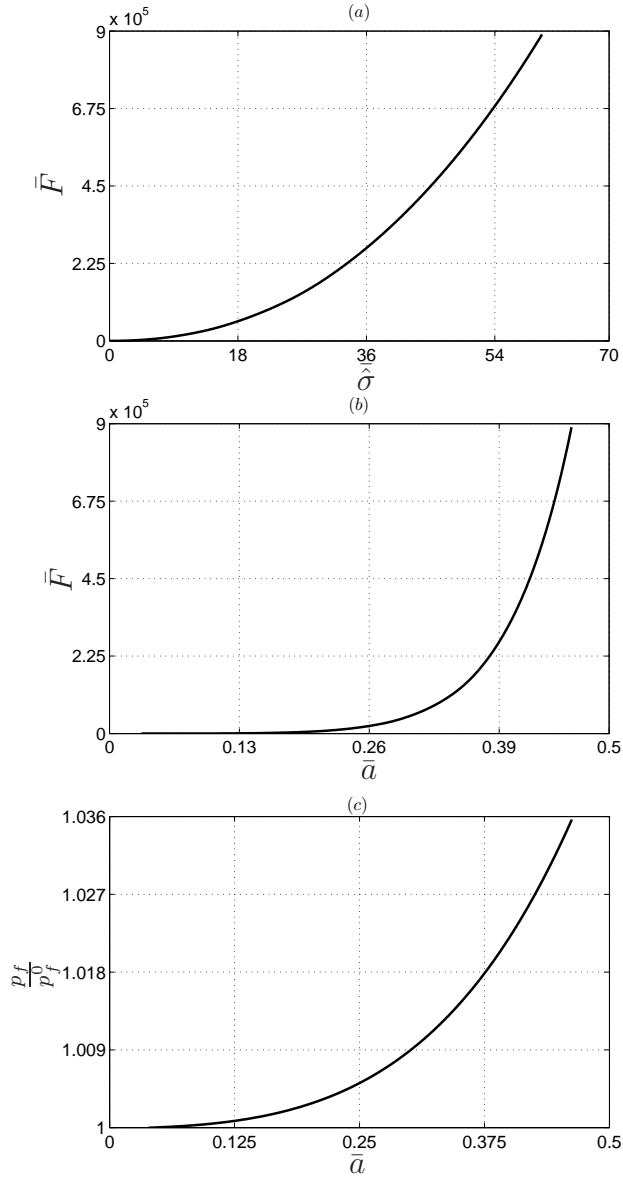
Figure 6.5: (a) Normalized total vertical electrostatic force vs. normalized substrate charge density. (b) Normalized total vertical electrostatic force vs. normalized radius of contact between the membrane and the substrate. (c) Fluid pressure in the membrane normalized by initial fluid pressure vs. normalized contact radius. The initial inflation of membrane is $\bar{r}_0 = 1.2$ and the Debye length is $\bar{k} = 100$. Changes in $\bar{a}$ are caused by changes in $\hat{\bar{\sigma}}$.

The above seen resistance to deformation arises from two sources. The first is the fluid pressure inside the membrane, which increases monotonically as larger contact area is formed, as shown in Figure 6.5(c). In our earlier work [56], we showed that, if a fluid-filled membrane was subjected to micropipette aspiration, even if the membrane itself had no bending stiffness, the change in fluid pressure could cause resistance to aspiration, which was in quantitative agreement with experiments. Similarly, in this work, the fluid pressure is also an important contributor to the structural rigidity of the membrane. The second source of resistance comes from the electrostatic repulsion between the charges on the membrane. The distribution of local charge density on the membrane is shown in Figure 6.6(a) for three different substrate charge densities $\bar{\hat{\sigma}} = \{0.1, 30, 60\}$, each corresponding to one equilibrium deformation shown in Figure 6.4. As the membrane is inflated to $\bar{r}_0 = 1.2$, the surface charge density remains uniform, but its magnitude normalized by the charge density in the referential state is reduced to 0.69. When the membrane is brought to the vicinity of the substrate, upon the non-homogeneous deformation, the charge distribution is no longer uniform. Specifically, in Figure 6.6(a), ϕ is the angular position along the membrane surface, while $\bar{\sigma}$ is the normalized local charge density. $\phi = 0$ corresponds to the upper pole (point A) on the membrane and $\phi = \pi$ corresponds to the lower pole (point O) in Figure 6.2(a). On each curve, the symbol "$\times$" is used to mark the location of the contact edge. The value ϕ_c at the edge of the contact zone is, respectively, $0.98\pi, 0.74\pi$ and 0.65π for $\bar{\hat{\sigma}} = \{0.1, 30, 60\}$, as shown in Figure 6.6(a). At $\bar{\hat{\sigma}} = 0.1$, the local charge density on the membrane is almost uniform with a slight increase within the contact zone. Such increase is due to the areal shrinkage in the contact zone that occurs during the deformation. As the substrate charge density increases to $\bar{\hat{\sigma}} = 30$ or $\bar{\hat{\sigma}} = 60$, the local charge density on the membrane decreases near the upper pole ($\phi = 0$) and increases quite
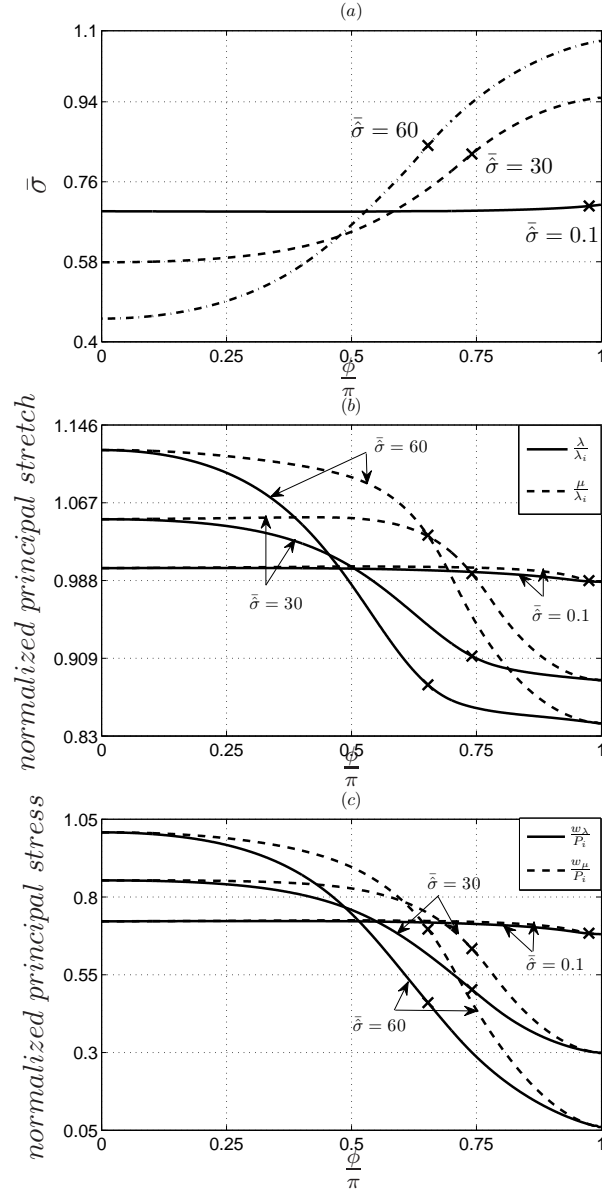
Figure 6.6: (a) Normalized local charge density on the membrane vs. the location of surface charge elements on the membrane. (b) Distribution of principal stretches along the membrane surface. (c) Distribution of principal stresses along the membrane surface. Above figures are plotted at an initial inflation $\bar{r}_0 = 1.2$, Debye length $\bar{k} = 100$ and at different substrate charge densities $\bar{\hat{\sigma}} = \{0.1, 30, 60\}$.

significantly inside and near the contact zone. This leads to areal dilation near the upper pole and great areal shrinkage within and near the contact zone. Such areal shrinkage causes the charges within and near the contact zone to be located much closer to one another compared with the spherical configuration. Because the electrostatic interactions between these charges are repulsive, this provides a resistance to further increase in charge density in this region caused by the membrane deformation.

The areal changes during deformation can be clearly seen from the distribution of the principal stretches and stresses on the membrane surface, shown in Figure 6.6(b) and Figure 6.6(c). Again, the location of the contact zone edge is marked with " $\times$ " on each curve. The principal stretches are normalized by the initial principal stretch in the membrane $\lambda_i = r_0/R = 1.2$ at an inflation of $\bar{r}_0 = 1.2$. The principal stresses are normalized by the initial stress $P_i = w_\lambda(\lambda_i, \lambda_i)$ in the inflated spherical membrane, which is given by $0.80G$, G being the material constant in equation (6.24). At $\bar{\bar{\sigma}} = 0.1$, the principal stretches and stresses are almost uniform everywhere on the membrane surface. However, for substrate charge densities $\bar{\bar{\sigma}} = \{30, 60\}$, both the principal stretches and stresses have non-uniform distribution along the membrane surface. Specifically, they have larger values on the free part of the membrane and smaller values on the contact part of the membrane. The largest values of the principle stretches and stresses occur at the upper pole ($\phi = 0$), where the areal dilation is most significant and the local charge density is smallest, as seen in Figure 6.6(a). The minimum values of the principle stretches and stresses are obtained at $\phi = \pi$ and it is clear that, within the contact zone, the principle stretches are mostly below one, indicating surface compression in this domain. This is consistent with the large local charge density in the contact zone observed in Figure 6.6(a).

All the above discussion applies at an initial inflation of $\bar{r}_0 = 1.2$. The

deformed equilibrium configurations of the membrane with the same substrate charge density $\bar{\bar{\sigma}} = 50$ and Debye length $\bar{k} = 100$, but different initial inflations $\bar{r}_0 = \{1.2, 1.4, 1.6, 2.0\}$, are shown in Figure 6.7(a). Note that, here, x and z are normalized by r_0, so that a comparison can be made on the "relative" deformation of the membrane. For fixed $\bar{\bar{\sigma}}$ and $\bar{k}$, it is observed that the relative deformation of the membrane increases with decreasing inflation and among these $\bar{r}_0$ values, the membrane with initial inflation of $\bar{r}_0 = 1.2$ undergoes the largest deformation. This is due to several reasons. Firstly, for smaller inflation, the charges on the membrane are closer to the substrate which results in larger electrostatic attraction. Secondly, for the same charge density in the reference configuration, smaller r_0 results in larger charge density on the membrane after inflation, which also contributes to larger electrostatic force. Finally, smaller $\bar{r}_0$ corresponds to smaller initial stresses in the membrane, which implies smaller resistance to deformation.

From Figure 6.4 to Figure 6.7(a), we considered constant normalized Debye length of $\bar{k} = 100$. To understand the effect of Debye length on the membrane deformation, the deformed equilibrium configurations of the membrane with initial inflation of $\bar{r}_0 = 1.2$, substrate charge density $\bar{\bar{\sigma}} = 50$ and different Debye lengths $\bar{k} = \{10, 100, 1000\}$ are shown in Figure 6.7(b). The Debye length k^{-1} is inversely proportional to the square root of ion concentration in the electrolyte solution; therefore, it is expected that by increasing the Debye length, the electrostatic screening from the ions will become weaker. As a result, at a given distance l, the exponential in equation (6.3) increases, which will increase the magnitude of the potential Φ at l. Thus, larger Debye length enhances the electrostatic interactions between the membrane and the substrate, which consequently should cause larger deformation of the membrane. This is confirmed in Figure 6.7(b), where, as the Debye length increases from $\bar{k}^{-1} = 0.001$ to 0.1, a clear increase in the deformation of the membrane and
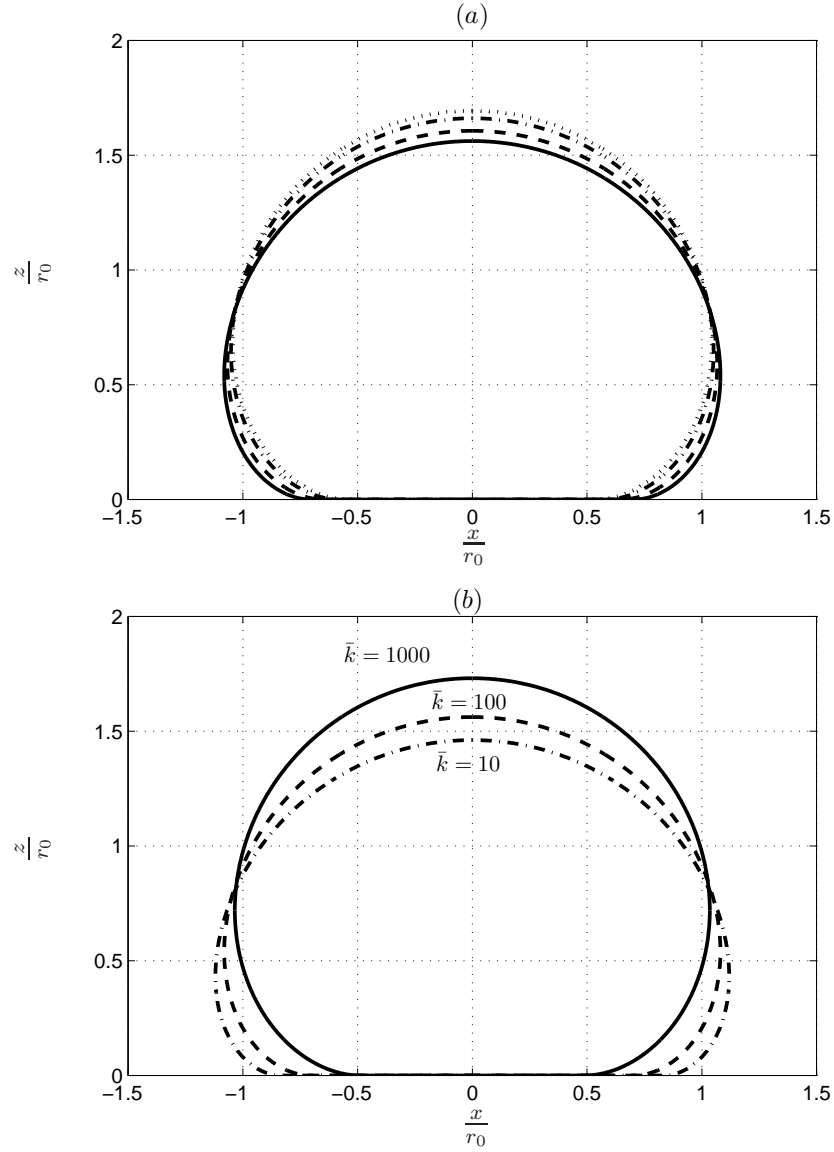
Figure 6.7: (a) Deformed equilibrium configuration of the membrane with different initial inflations $\bar{r}_0 = 1.2$ (solid line), 1.4 (dashed line),1.6 (dashed and dotted line) and 2.0 (dotted line) but the same substrate charge density $\bar{\hat{\sigma}} = 50$ and Debye length $\bar{k} = 100$. (b) Deformed equilibrium configuration of the membrane with initial inflation $\bar{r}_0 = 1.2$, substrate density $\bar{\hat{\sigma}} = 50$ and different Debye lengths $\bar{k} = \{10, 100, 1000\}$.

area of contact is observed.

Two quantities that are of most interest in contact mechanics are the contact area a and the applied force F causing the contact. The well-known Hertz theory of contact relates F and a for two solid spherical particles in contact based on the following assumptions: (1) the contact radius is small compared with the radii of the particles; (2) the region outside the contact zone is traction-free, so that the particles can be approximated by half spaces; (3) the strains are small, permitting the use of linear elasticity; (4) the surfaces are continuous and non-conforming and (5) the surfaces are frictionless [60]. With these assumptions, a cubic relation between F and a can be derived: [60]

$$F = \frac{4E^*a^3}{3R},$$ (6.27)

where a is the contact radius, $1/R = 1/R_2 + 1/R_3$, R_2 and R_3 being the radii of the two spherical particles, and $1/E^* = (1-\nu_2^2)/E_2 + (1-\nu_3^2)/E_3$, (E_2, ν_2) and (E_3, ν_3) being the Young's moduli and Poisson's ratios of the two particles. In the case of an elastic sphere contacting a rigid substrate, R_3 and E_3 can be set to infinity in equation (6.27). The Hertz theory was later extended to account for adhesive contact, one of the most famous theories being the Johnson-Kendall-Roberts (JKR) theory. In the JKR theory, the surface interactions are assumed to be short-ranged and negligible outside the contact zone. In contact problems involving particles with surface charges, some of the assumptions in the Hertz and JKR theories are clearly violated due to the long-ranged nature of the electrostatic interaction. Nevertheless, there has been some success in applying Hertz/JKR theories to adhesive contact driven by electrostatic forces. For example, it was shown that when a spherical elastic insulating particle with uniformly distributed surface charges made contact with a rigid conducting half space, the contact radius could be reasonably predicted by the

162

Hertz theory, if the electrostatic surface traction was replaced by an equivalent point load acting remotely from the contact zone [61].

In addition to the long-ranged electrostatic surface tractions acting both inside and outside the contact region, the problem considered in the present work violates the assumptions in the Hertz theory in several other aspects. The charged particle is not made of a single solid material, but consists of a membrane filled with fluid. The membrane and the fluid have different material behaviors characterized by different constitutive relations. In addition, the membrane is elastic, but it can undergo large nonlinear deformation. That is, it is not subjected to small strain approximations, and the reference and deformed configurations must be distinguished. Recognizing these differences, it is of interest to see how the force-contact radius relation from this work compares with predictions from the Hertz theory. To make such a comparison, an effective Hertz equation first needs to be established that involves parameters from this work. Specifically, if we estimate the contact radius from equation (6.27), then F would be interpreted as the total electrostatic force between the charged membrane and the substrate, as calculated in Figure 6.5(a) and Figure 6.5(b). R and a are the undeformed radius of the membrane and the contact radius, while E^* will be replaced by G/L as demonstrated earlier, with L being a length scale on the order of the thickness of the membrane. Such modification to equation (6.27) results in $F = 4Ga^3/3RL$, which can be written in the following form

$$\ln[\frac{3F}{4GR}(kR)^3] = 3\ln(ka) - \ln(\frac{L}{R}).$$
(6.28)

The above equation predicts that, if $\ln[\frac{3F}{4GR}(kR)^3]$ is plotted against $\ln(ka)$, a straight line will be obtained with the slope of 3 and intercept of $-\ln(\frac{L}{R})$. As we do not have exact information about L, we will compare our numerical

163

results with the following equation

$$\ln[\frac{3F}{4GR}(kR)^3] = 3\ln(ka), \tag{6.29}$$

where the intercept term in equation (6.28) has been removed. In fact, due to the uncertainly in L and the neglect of several governing parameters (addressed later), when converting equation (6.27) to (6.28), examining whether the cubic relation between F and a still holds in the current problem is more interesting than comparing the exact value of F at a given a.

Figure 6.8 plots $\ln[\frac{3F}{4GR}(kR)^3]$ vs. $\ln(ka)$ obtained from our numerical solutions (symbols) and from equation (6.29) (solid line). The different symbols correspond to different sets of governing parameters $\bar{r}_0$ and $\bar{k}$. The increase
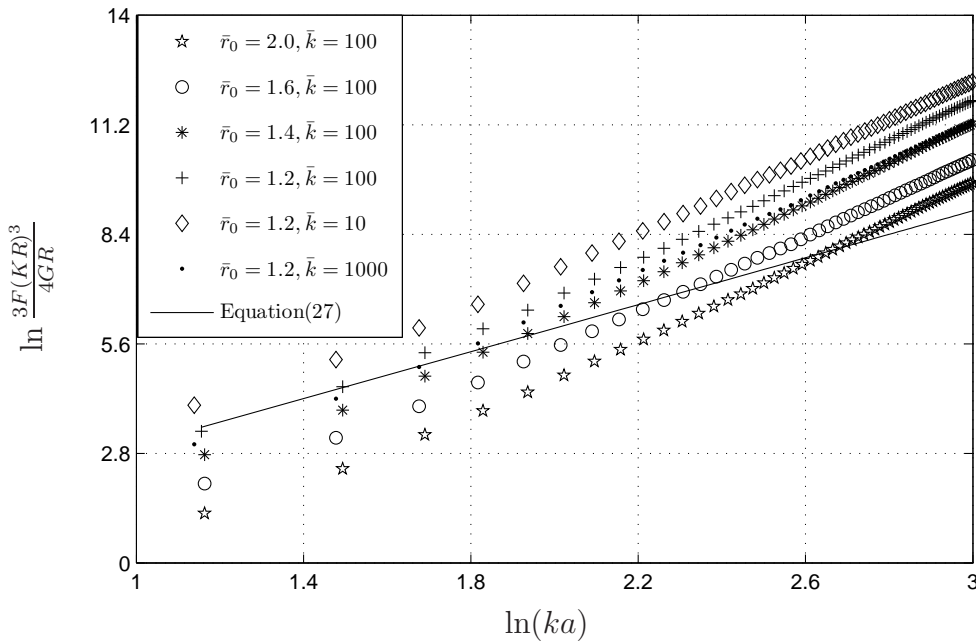
Figure 6.8: $\ln\frac{3F(KR)^3}{4GR}$ vs. $\ln(ka)$ for different initial inflations $\bar{r}_0 = \{1.2, 1.4, 1.6, 2.0\}$ at constant Debye length $\bar{k} = 100$ and for different Debye length $\bar{k} = \{10, 100, 1000\}$ at constant initial inflation $\bar{r}_0 = 1.2$.

in the electrostatic force and contact area is generated by varying the substrate charge density $\bar{\hat{\sigma}}$ from 0.1 to 50. For all the combination of governing

parameters shown in Figure 8, when $\ln(ka)$ is in the range of 1.16 to 1.4, the relation between $\ln[\frac{3F}{4GR}(kR)^3]$ and $\ln(ka)$ is nearly linear with slopes in the range of $2.9 \sim 3.2$. That is, despite the various differences between the Hertz contact problem and the membrane contact problem considered here, the cubic scaling between the total force and the contact radius remains when the deformation of the membrane is small. As deformation increases, the results from our model deviate from equation (6.29) in that there is a clear increase in the slope of the $\ln[\frac{3F}{4GR}(kR)^3]$ vs. $\ln(ka)$ curves for all sets of governing parameters. When $\ln(ka)$ is larger than 2.6, all the curves become parallel with a slope of approximately 5. In this regime, the total force and contact radius still follow a power relation $F \sim a^n$, with $n \approx 5 > 3$. As pointed out earlier, the faster increase of F as compared with the Hertz theory is exactly due to the resistances from the fluid pressure and the electrostatic repulsion near and within the contact zone.

It can also be seen from Figure 6.8 that the force-contact radius relation is affected by the governing parameters $\bar{r}_0$ and $\bar{k}$, which are not considered when converting equation (6.27) into (6.28). The effect of these parameters on the scaling relation between F and a is quite small, since all the curves in Figure 8 show a more or less parallel pattern. At small deformation ($\ln(ka)$ between 1.16 and 1.4), the initial inflation $\bar{r}_0$ has a slight influence on the slope of the curves, with smaller $\bar{r}_0$ having a smaller slope which is also closer to 3. However, the exact magnitude of F is strongly affected by these governing parameters. In general, larger force is obtained as the initial inflation $\bar{r}_0$ decreases or as the Debye length $\bar{k}^{-1}$ increases. This is consistent with the greater relative deformation obtained at lower $\bar{r}_0$ and higher $\bar{k}^{-1}$ values seen in Figure 6.7.

6.5 Conclusions

In this work, we study the adhesion of a flexible charged membrane, which is filled with incompressible fluid and resides in an electrolyte solution, to an oppositely charged rigid substrate. A nonlinear continuum model is formulated to study the mechanical response of the membrane under electrostatic interactions with the substrate. The membrane deformation is strongly coupled with the electrostatic interactions. The coupling is most significant for moderate deformation and becomes weaker for very large deformation. The adhesion is driven by electrostatic attraction between the membrane and the substrate, but is resisted by both the fluid pressure inside the membrane and the electrostatic repulsion between the membrane charges, the latter being most significant within and near the contact zone. Relative deformation of the membrane (normalized with respect to its radius after inflation) increases as the substrate charge density increases, as the initial inflation decreases, or as the Debye length of the solution increases. Together with the increase in deformation is the increase in the total electrostatic attractive force between the membrane and the substrate. Compared with the classical Hertz theory of contact, the cubic scaling ($F \sim a^n$, where $n = 3$) between the total force and the contact radius remains at small deformation, while n increases with deformation and becomes approximately 5 at very large deformations. The normalized inflation and Debye length appear to affect the actual magnitude of the total force, while having very small influence on the scaling relation between the total force and the contact radius. Although the results demonstrated here are for a given value of G (1N/m) and for $\bar{r}_0$ values above 1.2, the fundamental characteristics of the results do not apply only to these G and $\bar{r}_0$ values. We have, in fact, carried out calculations with different G and $\bar{r}_0$ values, and we observed that the qualitative behaviors demonstrated in this work remain the same.

Our model predicts the response of a charged membrane in contact with a charged substrate and provides useful information on how the adhesion can be modulated by changing certain parameters such as the Debye length, inflation and substrate charge density. The present model can be used to address some real-life problems. For example, the model can be used to predict electrostatic interactions between charged capsules and oppositely charged surfaces which are widely used in medicine, food technology, cosmetics, coatings, printing, and cleaning [23, 24, 43]. These capsules are fabricated from polymeric material, layer-by-layer deposition of oppositely charged polyelectrolyte onto charged colloidal particles and emulsion polymerization [24, 43]. The surface of the capsules is naturally charged and the electrostatic interactions with oppositely charged surfaces bring adhesion [23]. The surface properties of these charged capsules can be tailored to achieve desired interactions, particularly in drug delivery systems, where the capsules have to interact with targeted cells, tissues and organs [23]. Our model has the potential to study adhesion of these capsules induced by electrostatic forces. The model is also useful in studying the adhesion and spreading of vesicles. The deformed membrane shape, contact area, contact angle, and adhesive forces predicted from our model can be compared to measurements from experiments to test the applicability of the model to vesicle adhesion.

Limitations do exist in the present model. For example, the model does not account for possible rate dependent material properties of the membrane. This issue can overcome by adding the viscosity of the membrane and that of the enclosed fluid. The model can also be extended by including the compressibility of the fluid in the membrane. Friction between the membrane and the substrate is not considered which can also be included in the model. Our model has neglected bending, so it is only applicable to thin membranes with a thickness that is much smaller than its radius. It should be noted, however,

that the electrostatic repulsions between the charges on the surface can contribute to the apparent bending stiffness. For example, in a dilute electrolyte solution, the elasticity of a single-stranded DNA was shown to be mostly contributed by the electrostatic repulsion between the charges rather than the bending/torsion of the bonds [62]. Explicitly modeling the electrostatics can capture this part of the structural bending rigidity. For thick structures where mechanical bending stiffness cannot be neglected, the model can be modified by introducing the thickness and considering it as a shell.

Bibliography

[1] L. B. Freund and Y. Lin, "The role of binder mobility in spontaneous adhesive contact and implications for cell adhesion," *J. Mech. Physi. Sol.*, vol. 52, pp. 2455–2472, 2004.

[2] Y. Lin and L. B. Freund, "Forced detachment of a vesicle in adhesive contact with a substrate," *Int. J. Sol. Struct.*, vol. 44, pp. 1927–1938, 2007.

[3] K. L. Johnson, K. Kendall, and A. D. Roberts, "Surface energy and the contact of elastic solids," *Proc. R. Soc. Lond.*, vol. 324, pp. 301–313, 1971.

[4] P. Liu, Y. W. Zhang, Q. H. Cheng, and C. Lu, "Simulation of the spreading of a vesicle on a substrate surface mediated by receptor-ligand binding," *J. Mech. Physi. Sol.*, vol. 55, pp. 1166–1181, 2007.

[5] Q. H. Cheng, P. Liu, H. J. Gao, and Y. W. Zhang, "A computational modeling for micropipette-manipulated cell detachment from a substrate mediated by receptor ligand binding," *J. Mech. Physi. Sol.*, vol. 57, pp. 205–220, 2009.

[6] G. I. Bell, "Models for the specific adhesion of cells to cells," *Science*, vol. 200, pp. 618–627, 1978.

[7] S. Nir and M. Andersen, "Van der waals interactions between cell surfaces," *J. Membr. Biol*, vol. 31, pp. 1–18, 1977.

[8] E. A. Evans, "Detail mechanics of membrane-membrane adhesion and separation: I. continuum of molecular cross-bridges," *J. Biophys.*, vol. 48, pp. 175–183, 1985.

[9] E. A. Evans, "Detail mechanics of membrane-membrane adhesion and separation: Ii. discrete kinetically trapped molecular cross-bridges," *J. Biophys.*, vol. 48, pp. 185–192, 1985.

[10] A. V. M. Khachatourian and A. O. Wistrom, "Electrostatic pair-interaction force between semi-permeable membranes," *J. Phys. A: Math. Gen.*, vol. 35, pp. 2159–2171, 2002.

[11] K. Prechtel, A. R. Bausch, V. Marchi-Artzner, M. Kantlehner, H. Kessler, and R. Merkel, "Dynamic force spectroscopy to probe adhesion strength of living cells," *Phys. Rev. lett.*, vol. 89, pp. 028101(1–4), 2002.

[12] A. Boulbitch, "Enforced unbinding of biomembranes whose mutual adhesion is mediated by a specific interaction," *Eur. Biophys. J.*, vol. 31, pp. 637–642), 2003.

[13] A. Agrawal and D. J. Steigmann, "Mechanics of cellular membrane," in *Computational modeling in biomechanics* (S. De, F. Guilak, and M. R. K. Mofrdar, eds.), pp. 549–566, NY: Springer, 2010.

[14] H. Zhou, M. Gotzinger, and W. Peukert, "The influence of particle charge and roughness on particle-substrate adhesion," *Powder Technol.*, vol. 135-136, pp. 82–91, 2003.

[15] M. Takeuchi, "Adhesion forces of charged particles," *Chem. Eng. Sci.*, vol. 61, pp. 2279–2289, 2006.

[16] L. B. Schein, "Electrostatic proximity force, toner adhesion, and a new electrophotographic development system," *J. of Electro.*, vol. 65, pp. 613–617, 2007.

[17] H. Mizes, M. Ott, E. Eklund, and D. Hays, "Small particle adhesion: measurement and control," *Colloids and Surf.*, vol. 165, pp. 11–23, 2000.

[18] J. Q. Feng and D. A. Hays, "Relative importance of electrostatic forces on powder particles," *Powder Technol.*, vol. 135-136, pp. 65–75, 2003.

[19] J. Q. Feng, "Electrostatic interaction between two charged dielectric spheres in contact," *Phys. Rev. E.*, vol. 62, pp. 2891–2897, 2000.

[20] G. Bryant and J. Wolfe, "Electromechanical stresses produced in the plasma membranes of suspended cells by applied electric fields," *J. Memb. Biol*, vol. 96, pp. 129–139, 1987.

[21] R. P. Joshi and K. H. Schoenbach, "Theoretical predictions of electromechanical deformation of cells subjected to high voltages for membrane electroporation," *Phys. Rev. E*, vol. 65, pp. 021913(1–10), 2002.

[22] R. P. Joshi, Q. Hu, K. H. Schoenbach, and S. J. Beebe, "Simulations of electroporation dynamics and shape deformation in biological cells subjected to high voltage pulses," *IEEE Trans. Plasma Sci.*, vol. 30, pp. 1536–1546, 2002.

[23] A. M. Raichur, J. Voros, M. Textor, and A. Fery, "Adhesion of polyelectrolyte microcapsules through biotin-streptavidin specific interaction," *Biomacromolecules*, vol. 7, pp. 2331–2336), 2006.

[24] O. I. Vinogradova, O. V. Lebedeva, and B. S. Kim, "Mechanical behavior and characterization of microcapsules," *Annu. Rev. Mater. Res.*, vol. 36, pp. 143–178), 2006.

171

[25] J. I. Rey, R. J. Connolly, M. J. Jaroszeski, and A. M. Hoff, "Electrostrictive forces on vesicles with compartmentalized permittivity and conductivity conditions," *IEEE Trans. Dielectr. Electr. Insul.*, vol. 16, pp. 1280–1287, 2009.

[26] E. L. Florin, V. T. Moy, and H. E. Gaub, "Adhesion forces between individual ligand-receptor pairs," *Science*, vol. 264, pp. 415–417), 1994.

[27] A. Kloboucek, A. Behrisch, J. Faix, and E. Sackmann, "Adhesion-induced receptor segregation and adhesion plaque formation: a model membrane study," *Biophys. J.*, vol. 77, pp. 2311–2328), 1999.

[28] C. A. Reinhart-King, M. Dembo, and D. A. Hammer, "The dynamics and mechanics of endothelial cell spreading," *Biophys. J.*, vol. 89, pp. 676–689), 2005.

[29] A. Ashkin and J. M. Dziedzic, "Optical trapping and manipulation of viruses and bacteria," *Science*, vol. 235, pp. 1517–1520), 1987.

[30] D. R. McClay, G. M. Wessel, and R. B. Marchase, "Intercellular recognition: quantitation of initial binding events," *Proc. Natl. Acad. Sci.*, vol. 78, pp. 4975–4979), 1981.

[31] R. M. Hochmuth, N. Mohandas, and J. P. L. Blackshear, "Measurement of the elastic modulus for red cell membrane using a fluid mechanical technique," *Biophys. J.*, vol. 13, pp. 747–762), 1973.

[32] E. Evans, D. Berk, and A. Leung, "Detachment of agglutinin-bonded red blood cells. i. forces to rupture molecular-point attachments," *Biophys. J.*, vol. 59, pp. 838–848), 1991a.

[33] C. A. Reinhart-king, M. Dembo, and D. A. Hammer, "The dynamics and mechanics of endothelial cell spreading," *Biophys. J.*, vol. 89, pp. 676–689, 2005.

[34] H. Gao, J. Qian, and B. Chen, "Probing mechanical principles of focal contacts in cell-matrix adhesion with a coupled stochastic-elastic modelling framework," *J. R. Soc. Interface*, vol. 8, pp. 1217–1232, 2011.

[35] M. Dembo, D. C. Torney, K. Saxman, and D. Hammer, "The reaction-limited kinetics of membrane-to-surface adhesion and detachment," *Proc. R. Soc. Lond.*, vol. 234, pp. 55–83, 1988.

[36] M. R. K. Mofrad, H. Karcher, and R. D. Kamm, "Continuum elastic or vicoelastic models for the cell," in *Cytoskeletal mechanics models and measurements* (M. R. K. Mofrad and R. D. Kamm, eds.), pp. 71–83, NY, USA: Cambridge Uni. Press, 2006.

[37] K. H. Adams, "Mechanical equilibrium of biological membranes," *Biophys. J.*, vol. 12, pp. 123–130, 1972.

[38] L. Lopez, I. M. Duck, and W. A. Hunt, "On the shape of the erythrocyte," *Biophys. J.*, vol. 8, pp. 1228–1235, 1968.

[39] L. A. Taber, "Compression of fluid-filled spherical shells by rigid indenters," *J. Appl. Mech.*, vol. 50, pp. 717–722, 1983.

[40] L. A. Taber, "Large deflection of a fluid-filled spherical shell under a point load," *J. Appl. Mech.*, vol. 49, pp. 121–128, 1982.

[41] K. K. Liu, D. R. Williams, and B. J. Briscoe, "Compressive deformation of a single microcapsule," *Phys. Rev. E.*, vol. 54, pp. 6673–6680, 1996.

[42] M. Rachik, D. Barthes-Biesel, M. Carin, and F. Edwards-Levy, "Identification of the elastic properties of an artifical capsule membrane with the

compression test: effect of thickness," *J. Colloid Interface Sci.*, vol. 301, pp. 217–226, 2006.

[43] V. D. Gordon, X. Chen, J. W. Hutchinson, A. R. Bausch, M. Marquez, and D. A. Weitz, "Self-assembled polymer membrane capsules inflated by osmotic pressure," *J. Am. Chem. Soc.*, vol. 126, pp. 14117–14122), 2004.

[44] B. Nadler and T. Tang, "Decohesion of a rigid punch from non-linear membrane undergoing finite axisymmetric deformation," *Int. J. Non-linear Mech.*, vol. 43, pp. 716–721), 2008.

[45] S. Seyfert, A. Voigt, and D. Kabbeck-Kupijai, "Adhesion of leucocytes to microscope slides as influenced by electrostatic interaction," *Biomaterials*, vol. 16, pp. 201–207, 1995.

[46] W. S. Czarnecki and L. B. Schein, "Electrostatic force acting on a spherically symmetric charge distribution in contact with a conductive plane," *J. Electro.*, vol. 61, pp. 107–115, 2004.

[47] T. Matsuyama and H. Yamamoto, "The electrostatic force between a charged dielectric particle and a conducting plane," *Kona*, vol. 16, pp. 223–228, 1998.

[48] A. Kovetz, "Electromagnetic theory," Oxford Uni. Press, UK, 2000.

[49] D. J. Steigmann, "On the formulation of balance laws for electromagnetic continua," *Math. Mech. Solids*, vol. 14, pp. 390–402, 2009.

[50] A. Dorfmann, and R. .W. Ogden, "Magnetoelastic modelling of elastomers," *Europ. J. Mech. A/Solids*, vol. 22, pp. 497–507, 2003.

[51] J. N. Israelachvili, "Intermolecular and surface forces," Academic Press, 2010.

[52] R. M. Pashley and M. E. Karaman, "Applied colloid and surface chemistry," Wiley, 2004.

[53] W. B. Russel, D. A. Saville, and W. R. Schowalter, "Colloidal dispersions," Cambridge Uni. Press, UK, 1989.

[54] B. Nadler, "On the contact of a spherical membrane enclosing a fluid with rigid parallel planes," *International Journal of Non-Linear Mechanics.*, vol. 45, pp. 294–300, 2010.

[55] T. Sohail and B. Nadler, "On the contact of an inflated spherical membrane-fluid structure with a rigid conical indenter," *Acta Mech.*, vol. 218, pp. 225–235, 2011.

[56] T. Sohail, T. Tiang, and B. Nadler, "Micropipette aspiration of an inflated fluid-filled spherical membrane," *Z. Angew. Math. Phys.*, Available online, 2011.

[57] E. Donath, A. Budde, E. Knippel, and H. Baumler, "Hairy surface layer: Concept of electrophoresis combined with local fixed surface charge density isothems: Application to human erythrocyte electrophoretic fingerprinting," *Langmuir*, vol. 12, pp. 4832–4839), 1996.

[58] S. Fu, X. Feng, B. Lauke, and Y. Mai, "Effects of particle size, particle/matrix interface adhesion and particle loading on mechanical properties of particulate-polymer composites," *CompositesPartB*, vol. 39, pp. 933–961), 2008.

[59] K. S. Birdi, "Surface and colloid chemistry," CRC Press, 1997.

[60] K. L. Johnson, "Contact mechanics," Cambridge Uni. Press, 1987.

[61] T. Tang, C. Hui, and A. Jagota, "Adhesive contact driven by electrostatic forces," *J. Appl. Phys*, vol. 99, pp. 054906(1–6), 2006.

[62] S. Manohar, T. Tang, and A. Jagota, "Structure of homopolymer dna-cnt hybrids," *J. Phys. Chem. C*, vol. 111, pp. 17835–17845), 2007.

Chapter 7

Conclusions and Future Work

7.1   Conclusions

The significance of soft particles in both medicine and industry have led researchers to investigate their mechanical properties upon loading and how they interact with external stimuli. Mechanics of such particles involve many different parameters, as well as coupling between the system parameters such as a particle's deformation and tractions acting on the particle. In the literature, different mathematical models exist that attempt to capture the mechanical response of soft particles. It is important to recognize that it is not possible to capture all properties of soft particles within a single model. Each of the existing models has its own limitations and is only appropriate for certain particles under certain loading conditions. In this work, we explore the suitability of a continuum based nonlinear membrane model in describing the mechanics of a fluid-filled soft particle under contact conditions. Specifically, the particle is modeled as a two dimensional spherical membrane filled with incompressible fluid. The membrane is homogeneous, isotropic and (of) hyper-elastic (material). The bending stiffness of the membrane is neglected, but we did not confine our model to any other geometrical restrictions (i.e., the membrane can

undergo large deformations). With this model, we studied four axisymmetric problems with different loading conditions on the particle. The findings in each problem are summarized below.

The first problem concerns the symmetric indentation of the particle using two identical frictionless rigid conical indenters. The major resistance to deformation is provided by the enclosed fluid in the membrane. The indenter force, the contact radius and the fluid pressure were all found to increase nonlinearly with the indentation. Several observations were made when changing the sharpness of the indenter:

- By increasing the sharpness of the indenter, the force required to indent the membrane decreases and so does the fluid pressure which resists deformation.

- For flat indenters, the principal stresses increase from the poles to the equator such that the lowest stress is located at the pole while the largest stress is at the equator. However, for conical sharp indenters, the maximum principal stress is located at the pole and the stresses are much smaller and approximately constant away from the pole.

- For flat indenters, the pole stress remains approximately constant with the indentation and increases only at the last stage of the indentation. However, for conical indenters, the pole stress increases initially, then remains approximately constant and decreases at the end of the indentation process.

In the second problem, to better mimic the situation in a typical indentation test, we studied the mechanical response of the particle indented by a frictionless rigid conical indenter, while being supported by a rigid flat support. The relation between the indentation force and displacement was found to be linear for small deformation and nonlinear for large deformation. The

178

response of the particle was also observed to depend on the sharpness of the indenter:

- As the sharpness of the indenter decreases, the force required to deform the membrane to the same indentation depth increases. Meanwhile, the linearity in the force versus indentation curve decreases.

- The fluid pressure increases nonlinearly during indentation and decreases as the indenter sharpness increases.

- By increasing the indenter sharpness, the maximum stress significantly increases and becomes more localized about the indenter tip, while the stresses away from the indenter tip decrease and become almost constant with the indentation.

- The principal stress at the pole has strong dependence on the indenter sharpness. For sharp indenters $\alpha > 20^0$, the pole stress increases monotonically with indenter displacement, and, for blunt indenters, $\alpha < 20^0$, the pole stress decreases initially followed by an increase. This behavior is due to the coupling between the pole strain and the fluid pressure.

Overall, our model predicts well the nonlinear response for large deformation of the membrane which is observed in experiments for different soft particles.

In the third problem, we studied the micropipette aspiration of the particle, which has been widely used to determine the mechanical properties of soft particles. In the literature, different models exist to determine the physical properties of these particles from the micropipette aspiration. Usually these models capture small deformation and do not account for the nonlinear behavior of the particle. Our model predicts two critical suction pressures p and p' during aspiration. As the suction pressure increases from zero, prior to reaching the suction pressure p, the membrane deforms, but does not form

finite contact with the micropipette wall. Between p and p', the membrane forms contact with the micropipette wall. After reaching the maximum pressure value p', the aspirated length continues to increase, but, to maintain equilibrium, the suction pressure has to decrease. This predicts a "liquid-like" behavior during a load control test. The maximum pressure p' increases as the radius of the micropipette decreases or as the initial inflation increases. It has also been observed that deformation depends upon the pressure difference (i.e., the pressure inside the pipette P_1 and the outside ambient pressure P_2), but not on P_1 or P_2 individually. During aspiration, non-uniform and even discontinuous principal stresses and stretches are obtained on the surface of the membrane. This indicates that the deformed membrane does not possess spherical shape in general, especially when the deformation is large. Our model captures some of the experimental results in a good manner. Specifically, it predicts larger resistance associated with smaller micropipette sizes. The relationship between the aspiration pressure and the aspirated length captures the "solid-like" response at small deformation and "liquid-like" response beyond the maximum pressure point, both observed in experiments. The maximum pressure is shown to be inversely proportional to the radius of the micropipette, which is also consistent with experimental data.

In the last problem, we studied a charged particle located in an electrolyte environment that adheres to an oppositely charged substrate due to electrostatic interaction between them. The electrostatic traction on the membrane surface is calculated from the electric potential and is dependent on the deformed configuration of the membrane. The adhesion is driven by the electrostatic attraction between the membrane and the substrate, but is resisted by both the fluid pressure inside the membrane and the electrostatic repulsion among the charges on the membrane. Our model allows us to examine the nature of the coupling between the electrostatic interaction and the deformation

of the membrane. For example, an increase in the substrate charge density causes an increase in the deformation of the membrane, which, in turn, causes the charge distribution on its surface, uniform in its reference configuration, to become non-uniform, resulting in significant electrostatic repulsion between these charges. This repulsion is most pronounced within and near the contact zone and provides a source of resistance to its further deformation and contact formation. As a result, the coupling between electrostatics and deformation is most significant for moderate deformation and becomes weaker for very large deformation. At small deformation, the relation between the total electrostatic adhesive force F and the contact area a shows similar scaling ($F \sim a^n$, where $n = 3$) to the classical Hertz theory of contact, but the value of n increases as deformation increases. The deformation of the membrane increases as the substrate charge increases, as the initial inflation decreases or as the Debye length of the electrolyte solution increases.

The developed models can be used to investigate the particle response in practical situations. For example, the indentation model can be used to determine the Turgor pressure in a cell during indentation and can also be used to study the mechanical properties of the membrane in biological cells using poking experiments. Because the indentation model gives the locations on the membrane surface, where the stresses are minimal, it can be used for microinjection of foreign material into cells, where reducing the damage to the cell membrane is preferred. The micropipette model can be used for partial or complete aspiration of soft particles inside the pipette to determine their response at different aspirated lengths. It can predict the recovery response of the particles, as well as the response of soft gels that can be used as a microactuator in microfluidic devices. The adhesion model can be used to predict electrostatic interactions between charged capsules and oppositely charged surfaces which are used in the food industry, medicine, and cosmetics. This model is useful in

studying the deformation, adhesion and spreading of vesicles. In electropho-tography, our model can be used to study the particle-substrate interactions and the adhesion effect on the printing quality. In powder coating, the model can be used to study the particle interaction with the wall in determining the adhesion strength of the particle. Similarly, our models are also helpful in studying the flexible particles in other biotechnology, semiconductor and pharmaceutical industries.

7.2   Future Work

The primary objective of this work was to develop a continuum membrane model to study the mechanical response of soft particles that can undergo finite deformation. Since several assumptions have been made in the formula-tion, the model is not without limitations. The present work can be extended in a few directions. Firstly, the model assumes the enclosed fluid to be incom-pressible. The compressibility of the fluid has been neglected here, but may be considered in the future. This can be achieved by providing a constitutive law which prescribes the pressure of the fluid as a function of its volume change. Secondly, inhomogeneous and anisotropic material properties of the membrane can be introduced in the model. When these properties are introduced, the ax-isymmetric deformation may have to be relaxed. In addition, with anisotropy the strain energy function is not a function of principal stretches but the right Cauchy Green deformation tensor. Thirdly, rate-dependent properties of the membrane and viscosity of the fluid can be added by considering dynamic re-sponse of the particle. Fourthly, the membrane surface can also be modeled as porous material to allow the diffusion of liquid through the membrane. The diffusion or flux through the membrane depends on the chemical compositions of the enclosed and surrounding fluids and also on the pressure difference across

the membrane. The driving force for the transport of the fluid through the membrane can be obtained by considering the differences of the chemical potential and pressure across the membrane. Finally, adhesion of the membrane to other entities is only studied by considering electrostatic interaction. Friction as well as adhesion due to van der Waals interaction are absent from the current study and will be of interest in the future. Van der Waals force arises from the interaction between dipoles, and it includes three types: Keesom force (between two permanent dipoles), Debye force (between a permanent dipole and an induced dipole) and London dispersion force (between two instantaneous induced dipoles). The van der Waals attractive potential between two molecules depends on the inverse sixth power of the distance separating the two molecules. A repulsive branch is often added to the interaction potential to account for the repulsion resulting from overlapping of molecules. Knowing the van der Waals potential, the traction on the membrane due to van der Waals interaction can be calculated in the same way as the calculation of electrostatic traction in Chapter 6, i.e., by taking the gradient of the potential and using the principle of linear superposition. Dry or fluid friction between two physical surfaces can be included in the future work. Frictional force depends upon the contact geometry, topology, bulk and surface material properties. Different friction models are available that can used to determine the frictional force between the membrane and the substrate due to the applied external load.

Appendix A

Normalization of the BVP for chapter 6

Introduce the following normalization:

$$\bar{w} = \frac{w}{G}, \quad \bar{\sigma} = \frac{\sigma}{\sigma_0}, \quad \bar{\hat{\sigma}} = \frac{\hat{\sigma}}{\sigma_0}, \quad \bar{p}_f = \frac{p_f R}{G}, \quad \bar{k} = kR, \quad \bar{a} = \frac{a}{R}, \quad \bar{r}_0 = \frac{r_0}{R}, \quad \bar{H} = \frac{H}{R}.$$

(A-1)

In addition, all the lengths are normalized by R. Adding equations (6.6) and (6.7) and substituting in the normalized quantities, the traction on the membrane is expressed as

$$\mathbf{f}_e = \frac{\sigma_0^2 \bar{\sigma}(\bar{z})}{4\pi\epsilon_0\epsilon} \left\{ \int_0^{\bar{z}_{max}} d\bar{z}' \int_0^{2\pi} \frac{\bar{\sigma}'(\bar{z}')\bar{u}'(\bar{z}')}{\sin\tau'} (1 + \bar{k}\bar{l}_1(\theta', \bar{z}', \bar{z})) \frac{e^{-\bar{k}\bar{l}_1(\theta', \bar{z}', \bar{z})}}{[\bar{l}_1(\theta', \bar{z}', \bar{z})]^2} \mathbf{e}_{\bar{l}_1(\theta', \bar{z}', \bar{z})} d\theta' \right.$$
$$\left. + \int_0^\infty d\bar{R}_1 \int_0^{2\pi} \bar{\hat{\sigma}}\bar{R}_1 (1 + \bar{k}\bar{l}_2(\varphi, \bar{R}_1, \bar{z})) \frac{e^{-\bar{k}\bar{l}_2(\varphi, \bar{R}_1, \bar{z})}}{[\bar{l}_2(\varphi, \bar{R}_1, \bar{z})]^2} \mathbf{e}_{\bar{l}_2(\varphi, \bar{R}_1, \bar{z})} d\varphi \right\}. \quad \text{(A-2)}$$

If we define the normalized traction on the membrane as

$$\bar{\mathbf{f}}_e = \frac{\mathbf{f}_e}{\frac{\sigma_0^2}{4\pi\epsilon_0\epsilon}}, \qquad (A-3)$$

then

$$\bar{\mathbf{f}}_e = \bar{\sigma}(\bar{z})\Big\{ \int_0^{\bar{z}_{max}} d\bar{z}' \int_0^{2\pi} \frac{\bar{\sigma}'(\bar{z}')\bar{u}'(\bar{z}')}{\sin \tau'}(1+\bar{k}\bar{l}_1(\theta',\bar{z}',\bar{z}))\frac{e^{-\bar{k}\bar{l}_1(\theta',\bar{z}',\bar{z})}}{[\bar{l}_1(\theta',\bar{z}',\bar{z})]^2}\mathbf{e}_{\bar{l}_1(\theta',\bar{z}',\bar{z})}d\theta'$$
$$+ \int_0^{\infty} d\bar{R}_1 \int_0^{2\pi} \bar{\hat{\sigma}}\bar{R}_1(1+\bar{k}\bar{l}_2(\varphi,\bar{R}_1,\bar{z}))\frac{e^{-\bar{k}\bar{l}_2(\varphi,\bar{R}_1,\bar{z})}}{[\bar{l}_2(\varphi,\bar{R}_1,\bar{z})]^2}\mathbf{e}_{\bar{l}_2(\varphi,\bar{R}_1,\bar{z})}d\varphi\Big\}. \quad \text{(A-4)}$$

The normalized distances $\bar{l}_1$ and $\bar{l}_2$ in (A-4) are respectively

$$\bar{l}_1 = \sqrt{(\bar{x} - \bar{u}'\cos\theta')^2 + (\bar{y} - \bar{u}'\sin\theta')^2 + (\bar{z} - \bar{z}')^2}, \quad \text{(A-5)}$$

$$\bar{l}_2 = \sqrt{(\bar{x} - \bar{R}_1\cos\varphi)^2 + (\bar{y} - \bar{R}_1\sin\varphi)^2 + (\bar{z} + \bar{H})^2}. \quad \text{(A-6)}$$

The normalized electrostatic tractions in the tangential and normal directions are

$$\bar{f}_{et} = \frac{f_{et}}{\frac{\sigma_0^2}{4\pi\epsilon_0\epsilon}} = \bar{\mathbf{f}}_{et}.\mathbf{t}, \quad \text{(A-7)}$$

$$\bar{f}_{en} = \frac{f_{en}}{\frac{\sigma_0^2}{4\pi\epsilon_0\epsilon}} = \bar{\mathbf{f}}_{et}.\mathbf{n}. \quad \text{(A-8)}$$

Now, the governing equations in the normalized form in the free region of the membrane $\phi \in [0, \phi_c]$ are

$$\frac{d\lambda}{d\phi} = \frac{(\bar{w}_\mu - \lambda\bar{w}_{\lambda\mu})\cos\tau - (\bar{w}_\lambda - \mu\bar{w}_{\lambda\mu})\cos\phi}{w_{\lambda\lambda}\sin\phi} - \frac{\lambda\mu\bar{f}_{et}}{\bar{w}_{\lambda\lambda}}\frac{\sigma_0^2 R}{4\pi\epsilon_0\epsilon G}, \quad \text{(A-9)}$$

$$\frac{d\tau}{d\phi} = \frac{\lambda\mu(\bar{p}_f + \bar{f}_{en}\frac{\sigma_0^2 R}{4\pi\epsilon_0\epsilon G})}{\bar{w}_\lambda} - \frac{\bar{w}_\mu\sin\tau}{\bar{w}_\lambda\sin\phi}, \quad \text{(A-10)}$$

$$\frac{d\bar{u}}{d\phi} = \lambda\cos\tau, \quad \text{(A-11)}$$

and the normalized boundary conditions in this region are

$$\bar{u}(0) = 0, \quad \tau(0) = 0, \quad \bar{u}(\phi_c^-) = \bar{a}, \quad \tau(\phi_c^-) = \pi. \quad \text{(A-12)}$$

The normalized governing equations in the part of the membrane in contact with the substrate $\phi \in [\phi_c, \pi]$ are

$$\frac{d\lambda}{d\phi} = \frac{(\bar{w}_\mu - \lambda \bar{w}_{\lambda\mu}) \cos\tau - (\bar{w}_\lambda - \mu \bar{w}_{\lambda\mu}) \cos\phi}{w_{\lambda\lambda} \sin\phi} - \frac{\lambda\mu \bar{f}_{et}}{\bar{w}_{\lambda\lambda}} \frac{\sigma_0^2 R}{4\pi\epsilon_0 \epsilon G},\tag{A-13}$$

$$\frac{d\bar{u}}{d\phi} = \lambda \cos\tau,\tag{A-14}$$

and the normalized boundary conditions in this region are

$$\lambda(\phi_c^+) = \lambda(\phi_c^-), \quad \bar{u}(\phi_c^+) = \bar{a}, \quad \bar{u}(\pi) = 0.\tag{A-15}$$

With the normalization, the volume constraint equation is reduced to

$$\pi \int_0^{\bar{z}_{max}} \bar{u}^2 d\bar{z} = \frac{4}{3}\pi \bar{r}_0^3.\tag{A-16}$$

Clearly, the normalized BVP depends on the following dimensionless parameters

$$\bar{k}, \quad \bar{\hat{\sigma}}, \quad \bar{H}, \quad \frac{\sigma_0^2 R}{4\pi\epsilon_0 \epsilon G}, \quad \bar{r}_0.\tag{A-17}$$